Engineering Light-matter Interaction in Dielectric Nanophotonic Resonators

By

Shuren Hu

Dissertation

Submitted to the Faculty of the
Graduate School of Vanderbilt University
in partial fulfillment of the requirements
for the degree of

DOCTOR OF PHILOSOPHY

in

Physics

May, 2017
Nashville, Tennessee

Approved:

Sharon M. Weiss, Ph.D.

Richard F. Haglund, Ph.D.

Yaqiong Xu, Ph.D.

Jason Valentine, Ph.D.

Norman H. Tolk, PhD

To my family and all of the friends, near and far.

ACKNOWLEDGEMENTS

It is impossible to sufficiently express my thanks, on these few pages, to all those who have supported me and without whose help I could never have come so far. I especially wish to express my gratitude towards my academic advisor, Dr. Sharon M. Weiss. Joined her group with a low morale in research, I put a dollar bill on my cubical wall, only preparing myself to bear through graduate school and get a job. As time passed by, the dollar bill was gone and replaced with piles of printed research papers and fabricated samples. My curiosity was re-kindled and I indulged myself in an exciting game played with light. All these changes were thanks to the encouragement, mentorship, and advice that Dr. Weiss provided throughout my Ph.D. endeavor. She was always patient and supportive, helping restore my confidence after every failed fabrication and experiment. Her scientific intuition and insights have always helped to guide me in the right direction. When I showed her my “fun” side project: a cat-paw photonic crystal, she didn’t express any disapproval for wasting my time and instead encouraged me to probe deeper, resulting in Chapters 4 and 5 of this thesis. She showed me the qualities and scientific attitude a good scientist should possess and set a standard that I will always strive to attain.

I would like to thank all the recent graduates as well as present members of the Weiss Group for making the group such a dynamic and vibrant scientific, multicultural environment. Thanks to Dr. Judson Ryckman and Dr. Yang Jiao for sharing knowledge and helping me to get started. Thanks to Yiliang Zhao, Dr. Girija Gaur, Dr. Kelsey Beavers, Dr. Xing Wei and Dr. Jenifer Lawerie for helping me with surface chemistry in biosensing. Thanks to Kun Qin, Dr. Gilbert Rodriguez and Dr. Shweta Bhandaru for the great work in our collaboration projects. Also Thanks to Kevin Miller, Joshua Fain, Dr. Jeremy Mares, Suruj Deka, Balkrishnan M.B and Dr. Petr Markov for all the help.

The new group members, Francis Afzal, Tengfei Cao, Sami Halimi, Landen Ryder and Vijayashree Parsi Sreenivas (VJ), thank you for bringing in the young and vibrate dynamics into our group. I sure will miss the Friday afternoon “beer & raw egg” competition. I also would like to thank Stanley Lo from Dr. Philippe Fauchet’s group for discussions and critics.

I would like to thank Prof. Yaqiong Xu for her valuable advices, inspiring discussions and collaborations. Also thanks to Tianjiao Wang and Dr. Tu Hong in NanoCarbon group at Vanderbilt for being such great collaborators.

Thanks to all the staff at ViNSE, who always were willing to contribute their time to help out. Thanks to our hosts Dr. Ivan I. Kravchenko and Dr. Scott T. Retterer at Oak Ridge National Lab (ORNL) for accommodating our visits and helping us with fabrications.

Thanks to the folks in silicon photonics group at IBM Thomas J. Watson center. I would especially like to thank Dr. Marwan Khater, Dr. William M. Green, Dr. Ernst Kratschmer and Dr. Sabastian Engelmann for their advice and tremendous support during my stay.

Thanks to Dr. Rafael SALAS-Montiel in University of Technology of Troyes for NSOM measurements.

Thanks to the folks in large scale integrated photonics (LSIP) group at Hewlett-Packard Enterprise labs. I had a great internship and an eye-opening experience in the Silicon Valley. Thanks to my mentor and manager, Dr. Dave Kielpinski for his tremendous support and trust.

I would like to thank all of my friends, here in US, and far away in Asia and Europe. I cannot even begin to name everyone who have left such a valuable impression on me.

I want to specially thank Dr. Girija Gaur for her help and support in every aspect. I also thank Mr. Jim Scheske, Ms. Dorothy Chitwood, and Nancy C. Edward as my host family. These peaceful Jigsaw puzzle afternoons have always been a warm memory. Thanks to you all, Nashville has always felt like another home.

I would never have made this far without the unconditional love and support from my family. They stood behand me and gave me the ground I could stand on whenever the path ahead seemed dim. No son or brother could ask for better.

TABLE OF CONTENTS

Page

Chapter

LIST OF FIGURES

Figure Page

CHAPTER 1

INTRODUCTION

The interaction of light with matter is the foundation for the fundamental processes of optical emission, absorption, transmission, and reflection. The ability to control how light interacts with matter is therefore key to achieving technological breakthroughs across a wide range of photonic and optoelectronic applications. Some of the key highlights include: smaller and lower power light sources [1-4], more efficient solar cells [5-8], faster and low power optical data processing [9-12], enhanced nonlinear process [13, 14], stronger optomechanical coupling [15], and extremely sensitive detectors for sensing ultra-low concentrations of chemical and biological molecules [16-18]. The mature fabrication process of the microelectronics industry has enabled the transition of some nanophotonic devices from the laboratory to the market. In this thesis work, I present theoretical design methods and experimentally characterized nanophotonic structures that have the potential to further influence this transition for a variety of applications.

1.1 Overview of the dissertation

The main focus of this thesis is to optimize light-matter interaction through three key elements:

1. strength of the electric field ($\boldsymbol{E}^{(0)}$)
2. the magnitude of the refractive index change ($\Delta\varepsilon$),
3. the degree of spatial overlap of the optical field with the external perturbation (V)

In Chapter 2, we show a method to increase external perturbation ($\Delta\varepsilon$) by integration of more probes molecules onto a sensor surface. We experimentally test this idea on both microring and photonic crystal (PhC) platforms. In Chapter 3, a novel suspended microring resonator is demonstrated to increase the overlap between optical field and sensing region (V). In Chapter 4 and 5, a *de novo* PhC design method is proposed, which leads to increased optical field strength ($\boldsymbol{E}^{(0)}$). Chapter 6 presents conclusions and future work. The remaining sections of this chapter as introduction provides the necessary background knowledge and theoretical information regarding photonic resonators useful in realizing the aforementioned metrics.

1.2 Photonic resonators: tradeoff between Q-factor and V_m

Light-matter interaction is enhanced by the temporal and spatial confinement of photons. Temporal confinement is measured by the quality factor (Q-factor), which represents the photon lifetime in an optical cavity. Spatial confinement is characterized by mode volume (V_m) and is a measure of the ability to focus light down to a small volume. Figure 1.1 is a survey of the major optical resonators in nanophotonic research categorized by Q-factor and V_m. In general, there is a trade-off between Q-factor and V_m. The spatial confinement (V_m) often has to be relaxed in exchange for a prolonged temporal confinement (Q-factor) and vice versa. Simultaneously achieving high spatial and temporal confinement has been a long-time pursuit in nanophotonic researches and, if realized, holds the promise for a wide range of technological breakthroughs.

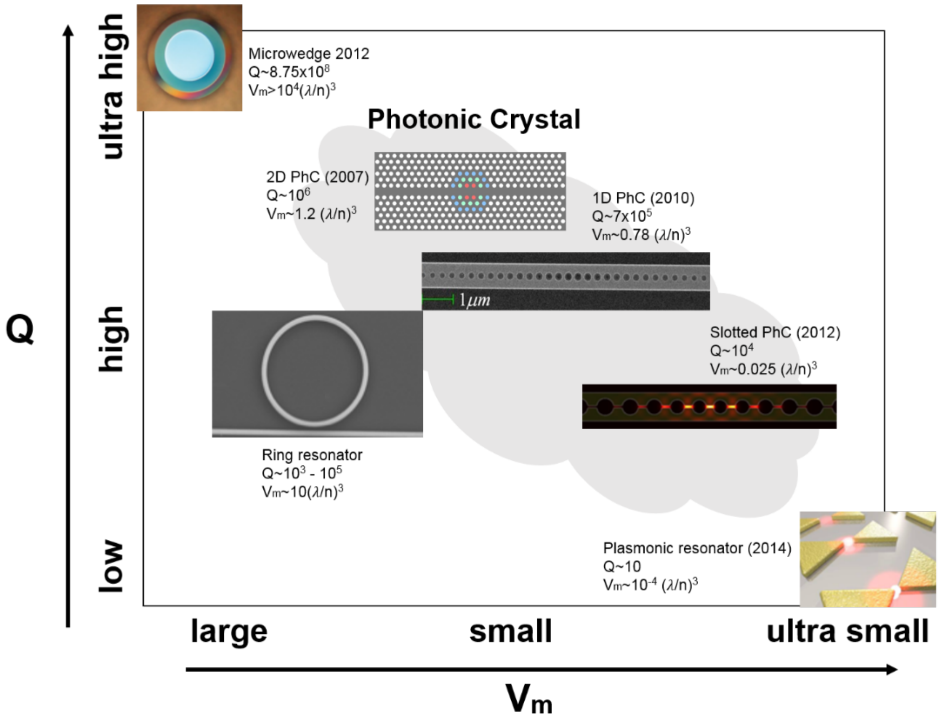

Figure 1.1 The Q-factor and V_m for different optical cavities. [19-23] Figures reprinted with permission from ©2012 NPG ©2008 OSA ©2010 AIP ©2012 AIP, Reprinted with permission from Ref. [22]. Copyright 2014 American Chemical Society.

1.1.1 Total internal reflection (TIR) based high Q-factor resonators

Total internal reflection (TIR), or index guiding, provides a simple method to confine light in a material with a refractive index higher than its surrounding environment. Fabry-Perot resonators and whispering gallery resonators are two common optical resonators that confine light based on TIR. In a Fabry-Perot cavity (Figure 1.2a), light is trapped within the high index material as it is constantly reflected back from the end facets, allowing for high temporal confinement. Also based on the principles of TIR, whispering gallery cavities are usually designed to be a circular disk or sphere. Light travels around the perimeter of the circles and forms a standing wave at resonance wavelengths. Both whispering gallery and Fabry-Perot resonators have high fabrication tolerance and have found broad applications in optics and photonics, such as lasers [24], sensors [25], modulators [10, 26] and optomechanics [27]. Q-factors of these cavities can be very high. For example, a wedge resonator is reported to have a Q-factor of ~ 10^8 [23]. However, V_m for these high Q-factor structures are generally quite large (> $10^4 (\lambda/n)^3$) [23]. In theory, the size limit for a Fabry-Perot cavity to form a standing wave is half of the wavelength of incident light in the cavity. However, in practice, the Q-factor decreases dramatically when the size is close to the wavelength. Similarly, for whispering gallery resonators, as the device size is reduced, the Q-factor decreases due to bending loss. This is because confinement by TIR is limited to a certain range of k vectors. As the cavity size is decreased, the bending radius increases, and therefore the range of k vectors that are confined by TIR is also reduced.

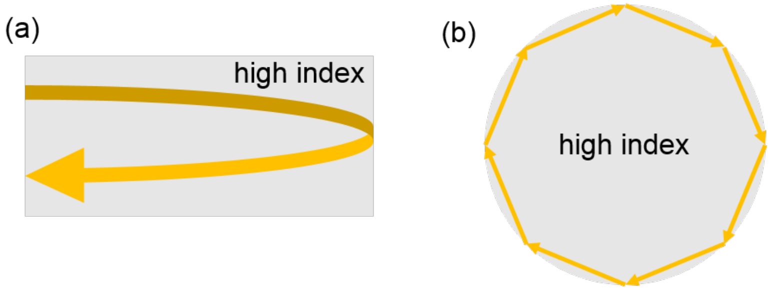

Figure 1.2 (a) Fabry-Perot cavity. (b) Whispering gallery mode cavity.

1.2.2 Plasmonic based low V_m resonators

A surface plasmon polariton (SPP) is an electromagnetic surface wave at a dielectric-metal interface that is formed when electromagnetic fields coupled to the charge density oscillation in the metal surface. In SPP, the energy oscillates between the electrical energy and kinetic energy of free electrons. Figure 1.3 shows the comparison between TIR and plasmonic resonators. In TIR optical resonators, the electrical energy and magnetic energy alternate every half period and are spatially offset by half of a wavelength. Therefore, half of a wavelength is the minimum self-sustaining oscillation. When the size of the resonator is reduced to below half of a wavelength, the energy does not fully recover after each oscillation and results in loss [28, 29]. In plasmonic resonators, the energy is stored in kinetic energy of free electrons:

$$u_k \sim \frac{1}{2}\varepsilon_0\left(\frac{\omega_p^2}{\omega^2}\right)E^2 \tag{1.1}$$

where ω_p denotes the plasma frequency, ε_0 is the permittivity of vacuum and $\boldsymbol{E}$ is the electric strength of the optical field. The size limit for a self-sustaining oscillation is no longer applicable to these devices. Therefore, plasmonic resonators can achieve very small V_m, on the order of 10^{-3} $(\lambda/n)^3$ [6]. Although V_m can be a small fraction of the wavelength cube, the Q-factor in plasmonic devices is typically only on the order of 10, especially in the optical frequency range. This is because Ohmic loss associated with kinetic energy storage of electrons is very high [28, 30].

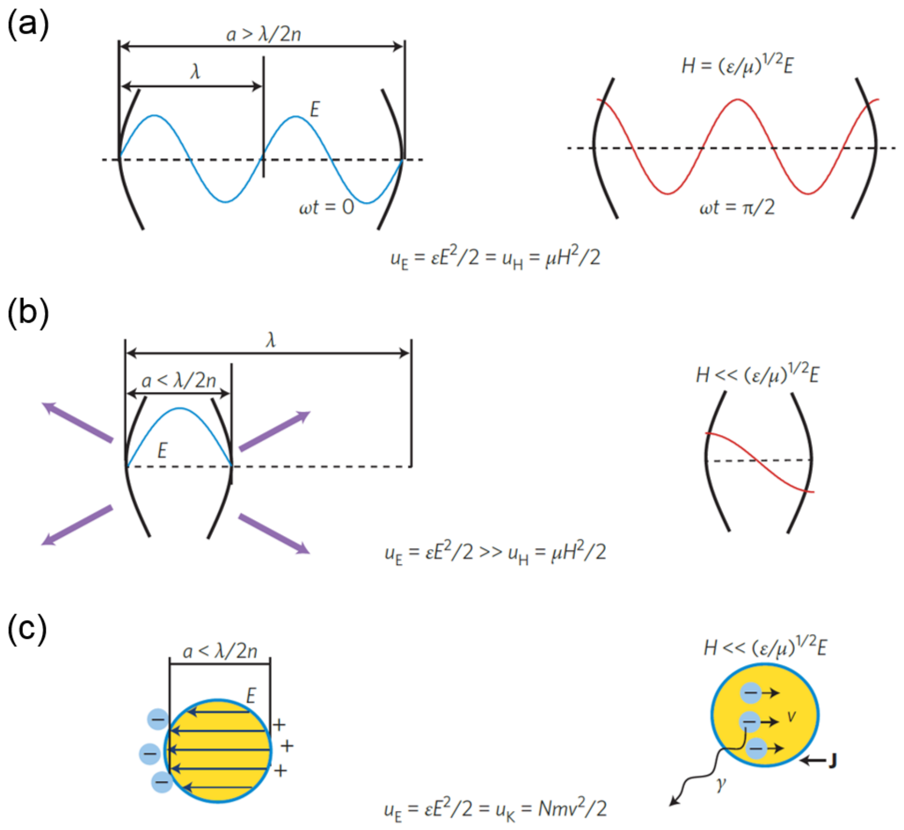

Figure 1.3 Energy oscillations in both (a,b) TIR and (c) plasmonic resonators [28]. Figures reprinted with permission from ©2015 NPG

1.2.3 Photonic band gap (PBG) based optical resonators

In Chapter 4, we provide a detailed discussion of the origin of the PBG and methods to control it. Here, a brief introduction to PhC cavities in comparison to TIR and plasmonic resonators is presented. In PhCs, light within certain range of frequencies can be confined by the photonic band gap (PBG) and is not allowed to propagate. Figure 1.4 shows examples of 1D and 2D PhCs. In a 1D PhC, the PBG confinement is only in the propagation direction, while in a 2D PhC, complete in-plane PBG confinement can be achieved with TIR in the out-of-plane direction. A 3D PhC has complete PBG confinement in all directions. However, the fabrication of 3D PhCs, especially cavities, is very challenging. Therefore, we will not further discuss it in this thesis. Because PBG confinement applies to all angles, the mode volume of PhC can approach the diffraction limit ~ $(\lambda/2n)^3$ while still maintaining a high Q-factor (~ 10^6) [31]. Chapter 4 and 5 discuss the designs of the PhC resonators to further enhance the Q-factor and reduce the V_m beyond the state-of-the art.

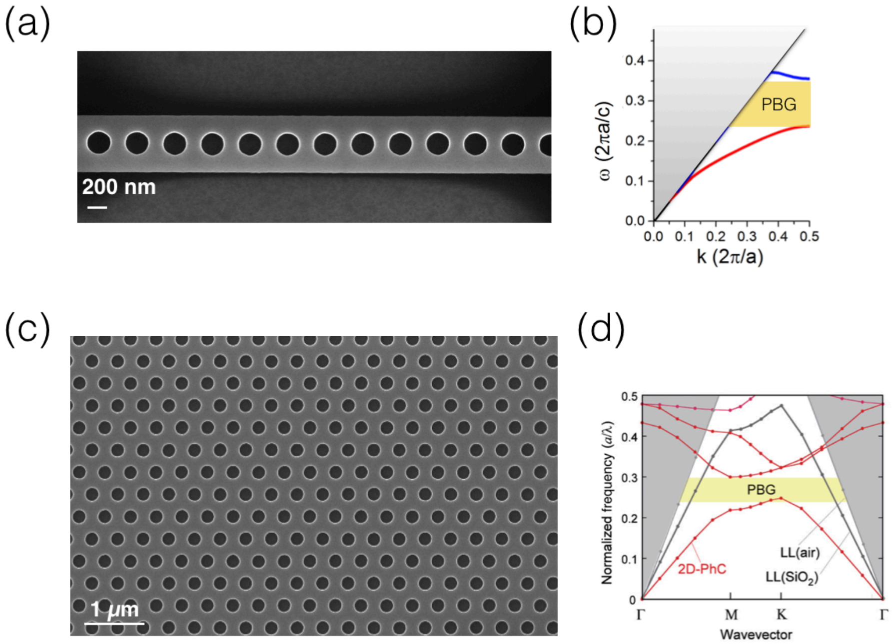

Figure 1.4 1D and 2D PhCs. (a) SEM of fabricated 1D photonic crystal nanobeam. (b) Band diagram of a typical 1D nanobeam unit cell. PBG is highlighted in yellow. (c) SEM of fabricated 2D PhC slab. (d) Band diagram of a hexagonal lattice 2D PhC. (Adapted from Ref. [31])

1.3 Perturbation theory

1.3.1 Master equation

Macroscopic electromagnetism is governed by the four macroscopic Maxwell equations:

$$\nabla \cdot \boldsymbol{B} = \boldsymbol{0} \tag{1.2}$$

$$\nabla \cdot \boldsymbol{D} = \rho \tag{1.3}$$

$$\nabla \times \boldsymbol{E} + \frac{\partial \boldsymbol{B}}{\partial t} = \boldsymbol{0} \tag{1.4}$$

$$\nabla \times \boldsymbol{H} - \frac{\partial \boldsymbol{D}}{\partial t} = \boldsymbol{J} \tag{1.5}$$

where $\boldsymbol{E}$ and $\boldsymbol{H}$ are the macroscopic electric and magnetic fields, $\boldsymbol{D}$ and $\boldsymbol{B}$ are the displacement and magnetic induction fields, and ρ and $\boldsymbol{J}$ are the free charge and current densities. Nearly all nanophotonic designs rely on the boundary conditions for these partial differential equations to obtain the desired eigensolutions, or “modes”.

We begin by formulating electromagnetism as an eigenvalue problem. We first make the assumption of a source-free case with linear, isotropic, dispersionless, nonmagnetic, and transparent materials. Specifically:

$$\boldsymbol{D}(\boldsymbol{r}) = \varepsilon_0 \varepsilon(\boldsymbol{r}) \boldsymbol{E}(\boldsymbol{r}) \tag{1.6}$$

$$\boldsymbol{B} = \mu_0 \boldsymbol{H} \tag{1.7}$$

Where $\varepsilon(\boldsymbol{r})$, the dielectric function, is a scalar function of position that does not depend on frequency or the strength of the electric field (in the linear optics regime).

According to Maxwell’s equations:

$$\nabla \cdot [\varepsilon(\boldsymbol{r}) \boldsymbol{E}(\boldsymbol{r}, t)] = 0 \tag{1.8}$$

$$\nabla \cdot \boldsymbol{H}(\boldsymbol{r}, t) = 0 \tag{1.9}$$

$$\nabla\times\boldsymbol{E}(\boldsymbol{r},t)+\mu_0\frac{\partial\boldsymbol{H}(\boldsymbol{r},t)}{\partial t}=0 \tag{1.10}$$

$$\nabla\times\boldsymbol{H}(\boldsymbol{r},t)-\varepsilon_0\varepsilon(\boldsymbol{r})\frac{\partial\boldsymbol{E}(\boldsymbol{r},t)}{\partial t}=0 \tag{1.11}$$

Separating the temporal component and spatial component of the eigensolution, we obtain:

$$\boldsymbol{E}(\boldsymbol{r},t)=\sum\boldsymbol{E}(\boldsymbol{r})\,e^{i\omega t} \tag{1.12}$$

$$\boldsymbol{H}(\boldsymbol{r},t)=\sum\boldsymbol{H}(\boldsymbol{r})\,e^{i\omega t} \tag{1.13}$$

where ***E(r)*** and ***H(r)*** represent the spatial distribution of optical energy, usually called the "mode profile". Inserting these two harmonic solutions back to Maxwell's equations, we find:

$$\nabla\cdot\boldsymbol{H}(\boldsymbol{r})=0 \tag{1.14}$$

$$\nabla\cdot[\varepsilon(\boldsymbol{r})\boldsymbol{E}(\boldsymbol{r})]=0 \tag{1.15}$$

$$\nabla\times\boldsymbol{E}(\boldsymbol{r})-i\omega\mu_0\boldsymbol{H}(\boldsymbol{r})=0 \tag{1.16}$$

$$\nabla\times\boldsymbol{H}(\boldsymbol{r})+i\omega\varepsilon_0\varepsilon\boldsymbol{E}(\boldsymbol{r})=0 \tag{1.17}$$

From Equation (1.16) and Equation (1.17), we obtain a set of equations:

$$\nabla\times\left(\frac{1}{\varepsilon(\boldsymbol{r})}\nabla\times\boldsymbol{H}(\boldsymbol{r})\right)=\left(\frac{\omega}{c}\right)^2 H(\boldsymbol{r}) \tag{1.18}$$

$$\nabla\times\nabla\times\boldsymbol{E}(\boldsymbol{r})=\left(\frac{\omega}{c}\right)^2\varepsilon(\boldsymbol{r})\boldsymbol{E}(\boldsymbol{r}) \tag{1.19}$$

where the H field in Equation (1.18) is the eigen-equation, often termed the "master equation" [31].

1.3.2 Perturbation theory

Applying the derivation of perturbation theory for a Hermitian eigenproblem onto Equation (1.19), we find:

$$\Delta\omega = -\frac{\omega}{2}\frac{\int \Delta\varepsilon(\boldsymbol{r})|\boldsymbol{E}(\boldsymbol{r})|^2 dV}{\int \varepsilon(\boldsymbol{r})|\boldsymbol{E}(\boldsymbol{r})|^2 dV} + O(\Delta\varepsilon^2) \tag{1.20}$$

This can also be intuitively understood as:

$$\Delta\omega = -\frac{\omega^{(0)}}{2U_{total}}\int \boldsymbol{E}^{(0)^*}\Delta\varepsilon\boldsymbol{E}^{(0)}dV \tag{1.21}$$

where $\boldsymbol{U}_{total} = \int \varepsilon(\boldsymbol{r})|\boldsymbol{E}(\boldsymbol{r})|^2 dV$ is the total optical energy in the resonator. For a particular optical cavity with a resonance ω, $\boldsymbol{U}_{\mathrm{total}}$ is pre-determined. The term $\int \boldsymbol{E}^{(0)^*}\Delta\varepsilon\boldsymbol{E}^{(0)}dV$ represents the optical energy that is perturbed by the external interactions such as biomolecule binding, carrier injection, temperature and background refractive index change.

Hence, as discussed qualitatively and quantitatively in this chapter, there are three key elements for enhancement of light-matter interaction: the strength of the electric field ($\boldsymbol{E}^{(0)}$), the magnitude of the dielectric function change ($\Delta\varepsilon$), and the degree of spatial overlap of the optical field with the external perturbation (V). Optimizing each of these three parameters is of utmost importance and will be the primary focus in the following chapters of this thesis.

CHAPTER 2

ENHANCING THE SENSITIVITY THROUGH INCREASED BIORECEPTOR DENSITY

2.1 Introduction

A label-free photonic biosensor is selected as one platform on which to investigate nanophotonic light-matter interaction in this thesis. Over the last several years, there have been an increasing number of global concerns that challenge healthcare resources including the spread of antibiotic resistance, an increased threat of pandemics through inter-continental transit networks, and rising healthcare costs. The lack of widespread availability of low-cost, rapid screening for diseases is a critical problem. Hence, there is an urgent need to develop cost-effective sensor technology that can be deployed in both clinical and field settings. One of the most promising approaches for achieving such sensors that are suitable for point-of-care (POC) immunodiagnostics applications is to leverage the silicon fabrication infrastructure that forms the basis of modern microelectronics technology [32-34]. Figure 2.1a shows a vision put forward by IBM of a disposable POC diagnostic device costing less than \$1 that leverages standard microelectronics components alongside microfluidics delivery and chemical functionalization, and is capable of monitoring and detecting a wide-array of label-free target molecules within minutes at femtomolar sensitivities using only 1 µL of biological fluids [35]. Utilizing label-free sensing systems is essential for POC applications so that no preprocessing of the analyte under test is required. Unlike conventional enzyme-linked immunosorbent assays, which indirectly test for the presence of target antigens or viruses through the use of secondary antibodies and time-dependent enzymatic reactions [36], label-free biosensors directly transduce the presence of target molecules of interest into a measureable output signal. Label-free photonic biosensors provide the additional benefit of being immune to environmental electromagnetic interference while providing fast response, non-destructive, direct monitoring of biomolecular activity with real-time kinetics information. Figure 2.1b depicts a schematic representation of photonic label-free biosensing. The surface of the optical biosensor is functionalized with probe molecules, using the necessary surface chemistry linkage to the substrate, to specifically capture target analytes of interest. When exposed to a complex bio-fluid, the probes capture only the desired target analytes and the unbound molecules are rinsed away. In most cases for optical biosensors, a spectral shift of the transmission or reflectance spectrum results from target molecule capture when the refractive index near the sensing surface is increased. These spectral changes are used to transduce molecular-binding events. While commercially available surface plasmon resonance instruments can offer label-free biosensing with a low detection limit of ~1 pg/mm^2, bulky housing with precisely controlled temperature and humidity is required to maintain detection accuracy and high-throughput sensor arrays with integrated lab-on-chip technology and reference sensors for mitigating environmental fluctuations, such as those achievable on a silicon photonics platform, are not possible.

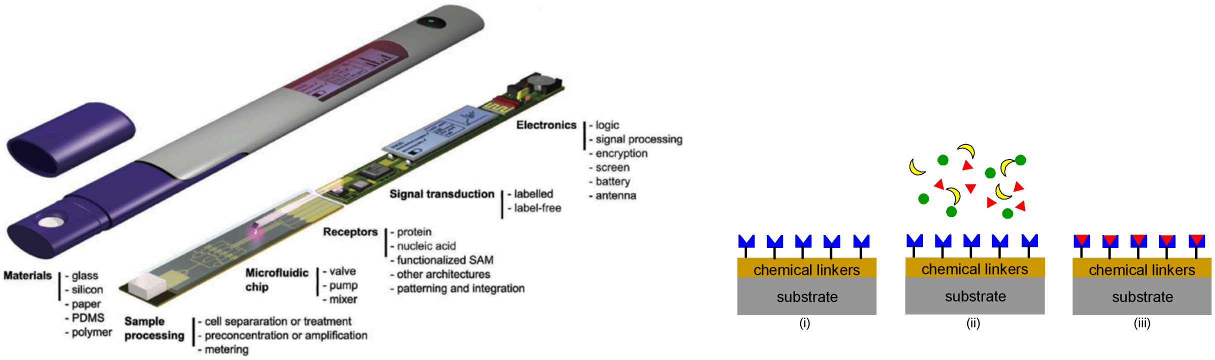

Figure 2.1 (a) IBM's proposed vision for a disposable POC test strip. (b) Schematic of label-free biosensing protocol: (i) sensor functionalized with chemical linkers and probe molecules designed to capture only a specific target molecule; (ii) sensor exposed to analyte under investigation; (iii) specific target molecules bind to probe molecules and other species are rinsed away [35, 37]. Figures reprinted with permission from ©2011 Wiley ©2009 Elsevier

Over the past decade, there has been rapid progress in the fabrication of low V_m, nanoscale optical devices, such as micro-ring resonators [38-42] and PhCs [33, 43-45]. Strong localization of the optical field in such photonic resonators gives rise to enhanced light-matter interaction, which results in a highly sensitive optical response to surface perturbations that is ideal for surface sensing applications [46]. Moreover, light trapped within resonant cavities experiences longer interaction times with surface-bound molecules, further increasing the molecular detection sensitivity of resonant photonic structures and making Si micro-ring resonators and PhCs among the most promising biosensing platforms. To date, micro-ring resonators have been the most widely studied silicon photonic structure for label-free biosensing, and an opto-fluidic, multiplexed micro-ring resonator sensor has been recently commercialized [34, 47-49]. PhCs are believed to be the next generation in optical biosensors with performance metrics in detection sensitivity and detection time that could surpass those of ring resonators [46, 50-55]. In PhC cavities, photons are strongly confined by the photonic bandgap within a sub-wavelength cavity region; PhC resonators with ultra-high quality factors, $Q > 10^6$, have been experimentally achieved [43, 45]. Captured biomolecules of interest can therefore interact with a significantly higher field intensity in PhCs compared to ring resonators, which could significantly increase achievable detection sensitivities [53]. Moreover, the lower mode volume of most PhCs compared to micro-ring resonators suggests that reduced analyte volumes and response times can be realized in PhC sensors. Recently, Chen *et. al*. reported a detection limit of 0.01 nM for cancer biomarkers, demonstrating great potential for ultra-low concentration multiplexed assays [53].

While the relatively small footprint of both micro-ring resonators and PhCs is an advantage for achieving compact sensor devices, the reduced sensing surface area inherent to these devices limits the total number of capture sites for target molecules. Having a reduced number of capture sites poses two challenges. First, if not enough target molecules are captured on the sensor, a detectable signal cannot be transduced. Second, even if there are enough capture sites to enable a sensor transduction event, a detectable signal response for sub-nM analyte concentrations may require increased sample volumes or assay times in order for target molecules to bind to a sufficient number of the probe capture sites. Additionally, these optical sensors will be more susceptible to false positives arising out of non-specific binding events at the sensing surface. In order to achieve rapid, ultra-low detection limits with μL sample volumes, it is imperative to achieve a high surface density coverage of probe molecules that maximizes target capture with minimum incubation times. Without a sufficiently high probe molecule density, signal amplification, for example through the use of a sandwich assay, must be implemented [38]. In this chapter, in-situ, base-by-base synthesis of single stranded DNA (ssDNA) probe molecules directly onto Si photonic sensor surfaces is demonstrated for the first time as reported in Ref [18], resulting in over 5-fold increased ssDNA probe surface coverage and a more than 5-fold increased detection sensitivity compared to sensors functionalized with traditional ssDNA probe attachment methods. Importantly, in addition to the detection of complementary DNA sequences, ssDNA probes can also be used for detecting a variety of other types of molecules when the proper sequence and molecule conformation is designed (*i.e.*, ssDNA aptamer probes [56, 57]). The in-situ probe synthesis approach opens up possibilities for rapid signal transduction of single biomolecule binding events by monitoring shifts of resonance wavelengths with analyte concentrations down to the fM range with μL sample volumes. The development of these optical label-free biosensors is therefore of great importance for the early clinical diagnosis of many life-threatening diseases [55].

2.2 Si photonic sensor platforms

The two prototypical Si photonic sensor platforms employed in this work, the micro-ring resonator and the PhC microcavity, are shown in Figure 2.2 and Figure 2.3. The micro-ring resonators and photonic crystals were fabricated on silicon-on-insulator (SOI) wafers with a 3 μm thick buried oxide layer (SOITEC). The thickness of the silicon device layer was 270 nm for the ring resonators and 220 nm for the photonic crystals. The wafers were cleaved and coated with a 300 nm ZEP520A photoresist (6000 rpm for 45 s). Electron beam lithography was performed using a JEOL9300FS tool at 100 kV voltage, 400 $\mu C/cm^2$. Following exposure, the samples were developed in xylenes for 30 s and rinsed thoroughly with isopropyl alcohol (IPA). The photoresist pattern was then transferred into the silicon layer by reactive ion etching (Oxford PlasmaLab 100) using $C_4F_8/SF_6/Ar$ gases to completely etch the exposed portion of the silicon layer. To further increase the index contrast for the photonic crystals, an undercut was performed to introduce an air gap between the device layer and the substrate. For the undercut procedure, the samples were cleaned with IPA and then baked on a hot plate at 115 °C for 10 min to fully remove absorbed water and IPA on the surface. AZ1513 photoresist was spin coated onto the samples at 4000 rpm for 45 s. Next, the samples were soft baked on a hot plate at 95 °C for 50 s and then exposed under a mask aligner at 70 mJ/cm^2 (Karl Suss MA6). An AZ MIF developer was used for 1 min, and the samples were then placed on a hot plate for 10 min at 115 °C to facilitate photoresist cross-linking. Finally, the samples were soaked in buffered oxide etchant (10:1) for 20 min to etch ~ 1 μm of the buried oxide layer. The samples were rinsed with DI water and dried under nitrogen before measurements.

Figure 2.2a shows a scanning electron microscope (SEM) image of a 5 μm radius micro-ring resonator coupled to a 500 nm width waveguide. The gap between micro-ring and waveguide is 300 nm, which meets the critical coupling condition and gives the highest extinction ratio by finite difference time domain simulations (FDTD). Figure 2.2b shows the electric field distribution of the z-normal plane calculated by FDTD simulations for TM-like polarization. The cross-section of the electric-field distribution (Figure 2.2c) indicates that the field is primarily localized on the top and bottom surfaces of the micro-ring resonator where molecules are most likely to be captured. TM micro-ring resonators are known to be more sensitive to surface changes compared to TE-like micro-ring resonators wherein the field is mainly distributed within the waveguide core [58]. Figure 2.2d shows a typical transmission spectrum of the 5 μm radius micro-ring resonator. The Q-factor is approximately 12,000 and the free spectral range is approximately 15.5 nm. For the transmission measurements, near-infrared light from a tunable continuous wave laser (1500 to 1630 nm, Santec TSL-510) was coupled into and out from millimeter-length bus waveguides using polarization-maintaining lensed fibers (OZ Optics Ltd.) mounted on piezo-controlled XYZ stages.

Photodetection of the transmitted light was performed using a fiber-coupled avalanche photodiode photoreceiver (Newport 1647).

Figure 2.3a-b show SEM images of the 2D PhC resonator used in this study. The multi-hole defect (MHD) design for an L3 cavity introduced by Kang *et. al.* is employed to increase the total surface area for probe molecule capture and to enhance the electric field-analyte overlap through the slot waveguide-like effect that takes place inside the defect holes [51, 59]. The MHD PhC sensor used in this study has a defect hole diameter of approximately 50 nm and a center-to-center defect hole spacing of 380 nm, which was previously shown to achieve the maximum Q-factor for the structure [59]. With the MHD design, both traditional PhC surface sensing, which relies on evanescent field interaction with surface-bound molecules, and sensing within the volume of the defect holes where the resonant mode is localized, are utilized for detecting biomolecule capture. Figure 2.3c shows the simulated electric field distribution in the MHD cavity as calculated by FDTD analysis for TE-polarized light. Since the electric field is highly concentrated in the defect region, capture of biomolecules within the defect holes will strongly perturb the field distribution and result in large shifts in the resonance wavelengths. A typical transmission spectrum with a resonance wavelength near 1550 nm and a Q-factor of ~ 4000 is shown in Figure 2.3d for the MHD L3 PhC.

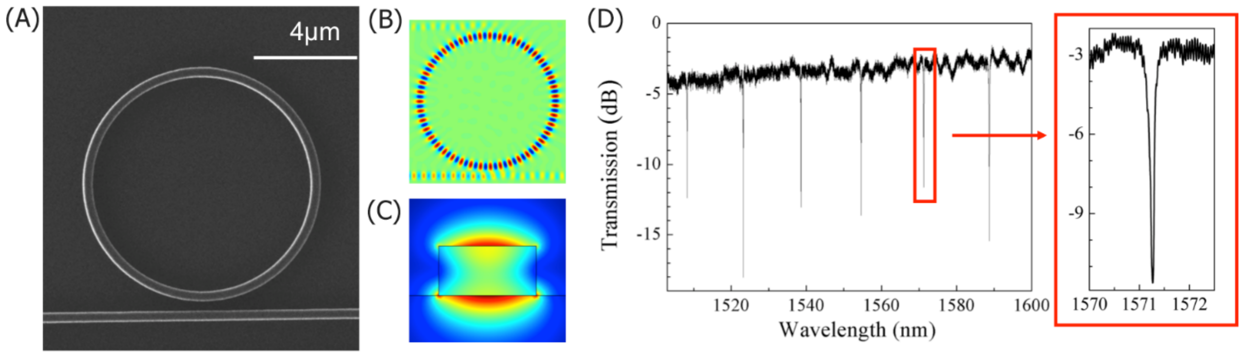

Figure 2.2 (a) SEM image of the 10 μm diameter microring resonator and 500 nm width waveguide. (b) On-resonance FDTD electric-field distribution in the ring resonator and bus waveguide. (c) Cross-sectional field distribution for a TM mode waveguide. (d) Measured transmission spectrum of the 10 μm ring resonator with zoom-in on one resonance. Reprinted with permission from Ref. [18]. Copyright 2014 American Chemical Society.

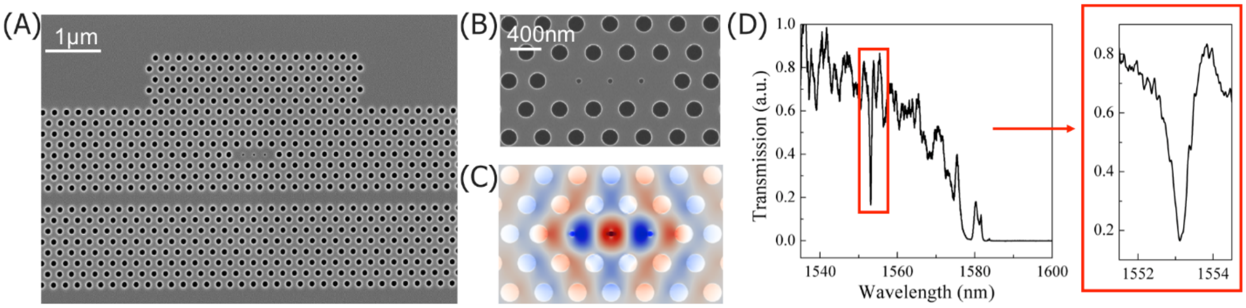

Figure 2.3 (a) SEM image of MHD PhC device with a lattice hole radius of 100 nm and a lattice constant *a* of 410 nm. (b) Zoom-in SEM image of MHD cavity showing the defect holes, ~50 nm in diameter, and neighboring right and left lattice holes that are shifted 0.15a outwards to achieve lower mode profile perturbation at the cavity edge. (c) Simulated electric field distribution (TE mode) for the MHD cavity showing strong field confinement in the defect hole region due to a slot waveguide-like effect. (d) Measured transmission spectrum of MHD PhC with zoom-in on cavity resonance. Reprinted with permission from Ref. [18]. Copyright 2014 American Chemical Society.

2.3 Surface functionalization method

Two methods of surface functionalization were performed on the Si micro-ring resonators and PhCs. For sensors functionalized by in-situ probe synthesis using the phosphoramidite method in which single DNA bases are added in a stepwise fashion, a single silane molecule is sufficient to attach the probe molecules to the oxidized Si surface. For sensors functionalized using a traditional conjugation technique in which the full sequence ssDNA probe molecules are directly attached to the sensor, a different silane molecule and a heterobifunctional cross-linker molecule are utilized to enable probe molecule attachment to the oxidized Si surface. Both silanization approaches have been shown to lead to nearly complete surface coverage of the sensors by silane molecules that are then available for additional molecule attachments [60]. It has been previously reported in the porous silicon (PSi) material system that the density of directly conjugated ssDNA probe molecules is 30-40% lower than in-situ synthesized ssDNA probe molecules inside nanoscale pores, in part due to steric hindrance between the negatively charged ssDNA molecules [60]. This result suggests that in-situ synthesis may be advantageous for functionalizing planar Si photonic biosensors.

In all biosensing experiments, the sample surface was first passivated by thermal oxidation. Samples were rinsed with DI water, acetone, and IPA three times each and then cleaned with piranha solution for 10 min at 120°C. The samples were then oxidized in an oven in an ambient air environment at 500°C for 10 min.

2.3.1 Probe DNA attachment using in-situ synthesis method

For samples functionalized using the in-situ synthesis technique, the oxidized sample surface was functionalized with hydroxyl groups before DNA attachment. Accordingly, samples were silanized with 4% N-(3-triethoxysilylpropyl)-4-hydroxy-butyramide (TEOS-HBA) in ethanol and deionized (DI) water for 4 hours and then rinsed thoroughly with DI water and dried under nitrogen. The samples were then annealed in an oven at 200°C for 16 hours. In order to form stable, cross-linked silane films, hydrolysis was performed after annealing by soaking samples in DI water for 4 hours to remove any unreacted silane molecules. Each sample was then placed in a custom designed sample holder in an Applied Biosystems Model 392 DNA Synthesizer for base-by-base attachment of the 16-mer probe DNA using the phosphoramidite method, similar to what was shown previously. By this method, each DNA base that is added is charge neutral owing to an attached protecting group and is much smaller than the full ssDNA sequence [60, 61]. Steric hindrance is therefore greatly mitigated in the case of in-situ synthesized ssDNA compared to the direct conjugation method. After synthesis, DNA molecules were deprotected in 1:1 ethylenediamine:ethanol solution for 30 min to activate them for future hybridization [60]. The samples were then soaked in ethanol for 30 min, rinsed with ethanol, and dried under nitrogen. For the samples used in fluorescence imaging, DNA probe sequences were labeled with FAM-6 fluorescence dye at the 5' end. The FAM-6 fluorescence dye was deprotected using the same using 1:1 ethylenediamine:ethanol solution for 30 min.

2.3.2 Probe DNA attachment using direct conjugation method

For samples functionalized using the direct conjugation method, the oxidized samples were soaked in a 1% 3-aminopropyltriethoxysilane (3-APTES) solution in anhydrous toluene for 15 min, and then rinsed with toluene and ethanol three times to remove excess unreacted 3-APTES molecules. The samples were annealed in an oven in air ambient at 150°C for 20 min to promote crosslinking among the silane molecules and increased stability in aqueous media. After silanization, the samples were incubated in 2.5 mg/mL sulfosuccinimidyl-4-(N-maleimidomethyl)cyclohexane-1-carboxylate (Sulfo-SMCC, Pierce) in 4-(2-hydroxyethyl)-1-piperazineethanesulfonic acid (HEPES) buffer for 2 hours, rinsed with HEPES buffer and soaked in HEPES buffer for another 1 hour to ensure all unreacted silane molecules were removed. An excess (100 µM) of 16-mer thiol modified probe DNA (5'-TAG CTA TGG TCC TCG T-3', 3' Thiol C3, Eurofins MWG Operon) in HEPES buffer was mixed 1:1 by volume with a disulfide reducing agent tris(2-carboxyethyl)phosphine (TCEP, Pierce) in DI water and ethanol for 30 min and then pipetted onto the sample. After 1 hour incubation at 37°C, the sample was soaked in HEPES buffer for 20 min at 37°C, rinsed with DI water, and dried with nitrogen gas to remove any remaining unattached molecules. For the fluorescence measurements performed to quantify probe molecule surface coverage, the probe DNA was purchased with a FAM-6 fluorescent label, and a cleavable linker molecule, N-succinimidyl-3-(2-pyridyldithio)propionate (SPDP), was substituted for Sulfo-SMCC. After the silanization process described above, the sample was incubated in 6.5 mM SPDP in ethanol for 30 min, then soaked in IPA for 10 min, and rinsed with IPA and DI water three times each. 200 µL of a 100 µM solution containing thiol-modified FAM6-labeled DNA probes in HEPES buffer was reduced using a beaded resin on which TCEP was immobilized. It is essential that no TCEP is present in the DNA solution. If any TCEP were present in the DNA solution upon exposure to the SPDP-functionalized Si sample, it would cleave the SPDP from surface before allowing DNA binding. The SPDP-functionalized sample was incubated in the reduced FAM6-labeled DNA probe solution for 1 hour, followed by a 20 min soak in HEPES buffer. Next, the DNA was cleaved from the surface through exposure to 250 µL of 2 mM TCEP in HEPES buffer for 30 min. Since the FAM6 florescence dye is sensitive to pH (an acid environment will oxidize the dye and quench florescence), the pH of the TCEP solution was adjusted to around 7.5 using sodium hydroxide. Finally, the TCEP solution was collected into a quartz cuvette for quantification of the probe molecule concentration by absorbance measurements.

2.3.3 Target PNA attachment

Complementary PNA sequences (ACG AGG ACC ATA GCT A, BioSynthesis) were chosen as the target molecules for all micro-ring resonator and photonic crystal sensors. Complementary PNA in DI water at a concentration of either 1 or 100 μM was pipetted onto each sample and incubated at 37 °C for 1 h. Samples were then soaked in HEPES buffer for 20 min to remove unhybridized oligos, thoroughly rinsed with DI water, and dried under nitrogen.

2.4 Sensitivity enhancement with increased probe molecule surface coverage

Figure 2.4a,c and Figure 2.5a show the sensing results for the hybridization of ssDNA and single strand peptide nucleic acid (ssPNA) target molecules to Si micro-ring resonators and PhCs, respectively, which have been functionalized by in-situ synthesized ssDNA probe molecules. Figure 2.4b, d and Figure 2.5b show the sensing results for ssDNA and ssPNA hybridization to Si micro-ring resonators and PhCs, respectively, which have been functionalized by directly conjugated ssDNA probe molecules. The sensing experiments shown in Figure 2.4a and b were performed using 100 μM target ssPNA, while Figure 2.5c and d shows the sensing results for 100 nM ssDNA detection. Experiments conducted using a variety of other target molecule concentrations are presented in Section 2.5 and suggest that the silicon photonic sensors respond similarly to ssPNA and ssDNA target molecules and that the probe molecule binding sites are nearly all saturated when exposed to at least a 100 nM concentration of complementary target molecules.

For both the ring resonators and PhCs, the resonance shifts after ssDNA probe and ssDNA/ssPNA target attachment are significantly larger when in-situ synthesized ssDNA probe molecules are utilized. In all cases, when a sufficiently high concentration of target molecules was used to saturate the available probe molecule binding sites (*i.e.*, > 100 nM), the resonance wavelength shift resulting from target molecule hybridization was nearly the same as the resonance shift following probe attachment. This suggests that nearly 100% hybridization efficiency can occur for all probe molecule densities employed in this work. Since the magnitude of the resonance shift is a direct indication of the number of molecules attached to the surface, we can infer that the enhanced sensitivity of the in-situ probe functionalized sensors is due to the increased number of probe molecules on the surface available for hybridization. The in-situ synthesis method enables the increased probe coverage by adding uncharged DNA monomers in a base-by-base fashion, which reduces the effects of steric hindrance and charge repulsion that challenge the immobilization of longer, negatively charged ssDNA molecules. In an attempt to minimize charge repulsion in the conjugated probe ssDNA molecules, $MgCl_2$ was added, as described later in Section 2.6.1. However, only a slight increase in the resonance wavelength shift corresponding to a small increase in the probe molecule coverage resulted even after an increased incubation time and increased probe molecule concentration were utilized.

As summarized in Figure 2.4c and Figure 2.5c, the increased resonance shift due to probe molecule attachment and the detection sensitivity enhancement for the target molecules are approximately 5-fold for the ring resonators and 7-fold for the PhCs functionalized by the in-situ synthesis method. The larger resonance shifts for the MHD PhC structure are likely due to an increased number of ssDNA probes within the ~50 nm sized defect holes where the electric field is strongly localized. Prior work demonstrated that the in-situ DNA synthesis process is capable of achieving a high density of ssDNA molecules inside 30 nm – 60 nm sized pores in silicon [60]. Hence, the increased number of probe molecules within the PhC defect holes along with the strong light-matter interaction inside the defect holes gives higher detection sensitivity enhancement factors in the MHD PhCs. This result highlights the importance of optimizing probe molecule coverage in regions of strong light-matter interaction and shows the potential of the in-situ probe synthesis method for achieving improved probe surface coverage on silicon photonic sensors.

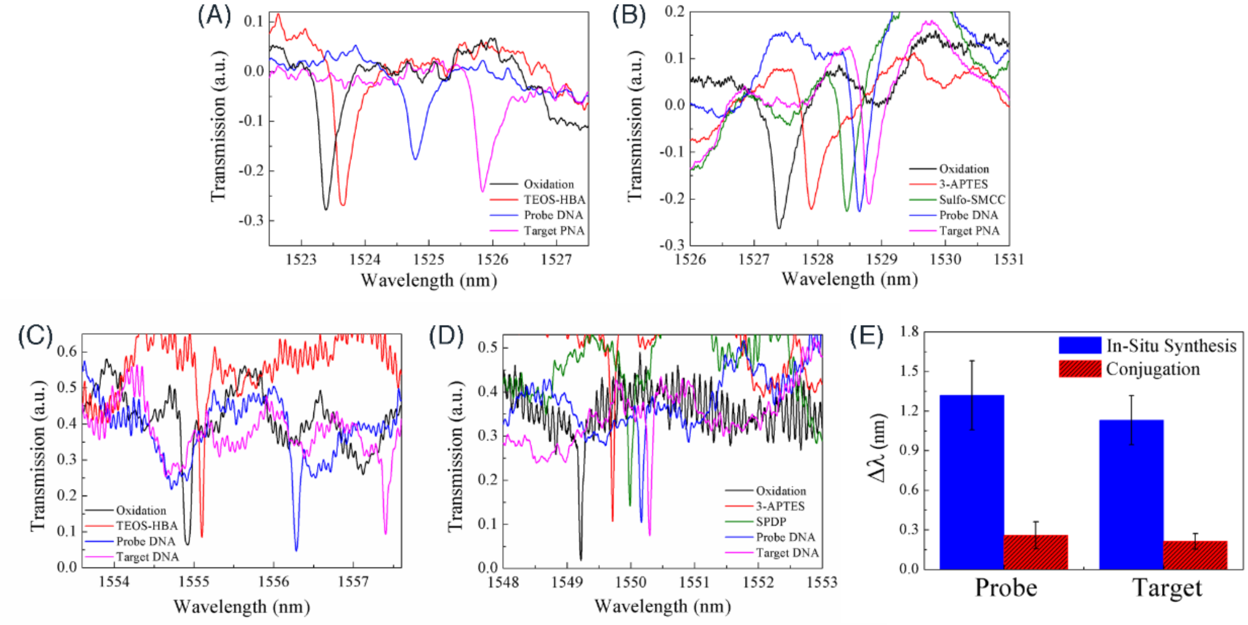

Figure 2.4 Transmission spectra of ring resonators functionalized by in-situ synthesis of ssDNA probes (a, c) and direct conjugation of ssDNA probes (b, d). (a) and (b) show ssPNA target detection, while (c) and (d) show ssDNA target detection. Each spectrum corresponds to a transmission measurement made after a different molecule was attached to the surface. A significantly larger resonance shift upon both ssDNA probes attachment and ssPNA/ssDNA target hybridization results for the ring resonator prepared using the in-situ probe synthesis approach. (e) Average resonance wavelength shifts for probe and target binding on four ring resonator sensors functionalized by the in-situ ssDNA probe synthesis method and four ring resonators functionalized by the traditional ssDNA probe conjugation technique. Reprinted with permission from Ref. [18]. Copyright 2014 American Chemical Society.

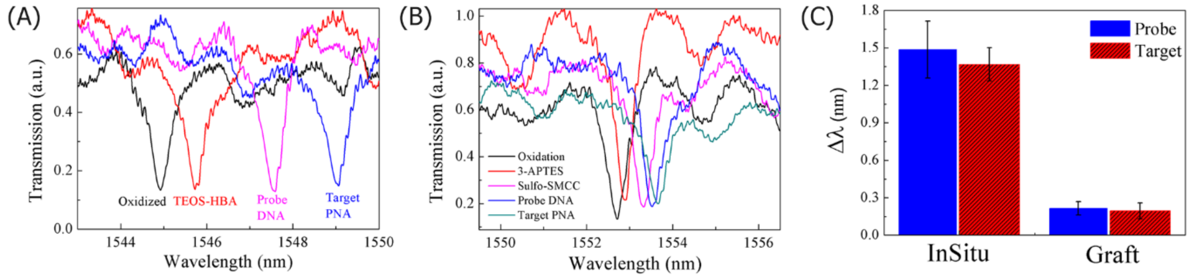

Figure 2.5 Transmission spectra of MHD PhCs functionalized using (a) in-situ synthesis and (b) direct conjugation methods for probe molecule attachment. Each spectrum corresponds to a transmission measurement made after a different molecule was attached to the surface. The ssDNA probes attachment by in-situ synthesis, as well as subsequent ssPNA hybridization, results in a significantly larger resonance wavelength shift compared to the direct conjugation method (c) Average resonance wavelength shifts for probe and target binding on three MHD PhCs functionalized by the in-situ ssDNA probes synthesis method and three MHD PhCs functionalized by the traditional ssDNA probes conjugation technique. Reprinted with permission from Ref. [18]. Copyright 2014 American Chemical Society.

2.5 Target concentration-dependent sensor response

Experiments were also conducted using a variety of other target molecule concentrations to estimate the minimum detectable target molecule concentration. As shown in Figure 2.6, a concentration-dependent resonance shift was observed when the target ssDNA concentration was varied between 10-100 nM. However, no change in the magnitude of the resonance wavelength shift of the sensors was observed when the target ssPNA concentration was varied between 1-100 µM. Note that the resonance shifts measured for sensors exposed to 100 nM target ssDNA molecules in Figure 2.6c are only slightly less than those shown in Figure 2.4 for 100 µM concentration, suggesting that nearly all probe molecule binding sites are saturated when exposed to at least 100 nM concentration of target molecules.

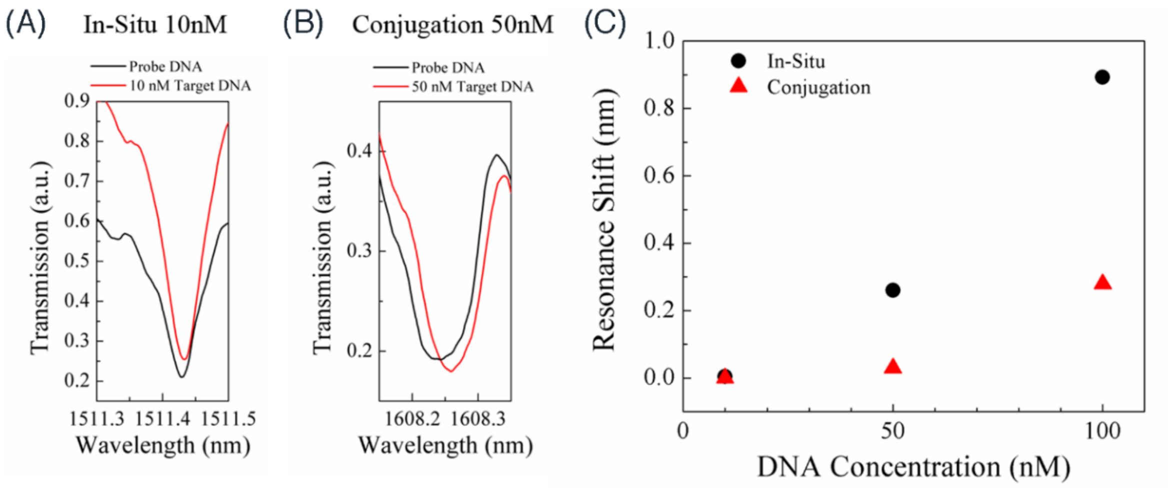

Figure 2.6 (A) Resonance shift (0.005 nm) when 10 nM target ssDNA is exposed to a micro-ring resonator functionalized with in-situ synthesized ssDNA probe molecules. (B) Resonance shift (0.02 nm) when 50 nM target ssDNA is exposed to a micro-ring resonator functionalized with directly conjugated ssDNA probe molecules. (C) Comparison of resonance shifts at different target ssDNA concentrations for both in-situ and conjugation prepared sensors.

Micro-ring resonators functionalized with in-situ synthesized ssDNA probe molecules could detect down to 10 nM target ssDNA concentration while sensors functionalized with directly conjugated ssDNA probe molecules could detect down to 50 nM target ssDNA. Since the target molecule concentration in solution decreases as the target molecules are hybridized to ssDNA probe molecules, for ultra-low concentration detection, it is important to reduce the non-transducable area on the sensor surface. In the experiments presented in this work, the entire Si chip surface was functionalized with probe molecules. Therefore, most of the target molecules in low concentration solutions are bound to regions of the chip that do not overlap with the resonant mode of the ring resonators and PhCs and thus do not contribute to a shift of the resonance wavelength. Assuming that target molecules uniformly bind onto surfaces across the Si chip, it is possible to estimate the sensor detection limit based on the area ratio between the device region (*i.e.*, micro-ring) and the entire Si chip. The ring resonators are 5 μm in radius with 500 nm wide waveguides. The size of the Si chip is approximately 5 mm by 5 mm. Accordingly, this means that only 0.00006% of the total number of bound target molecules contribute to a resonance shift in our sensors. For in-situ functionalized samples, the detection limit could be as low as 6 fM, while the detection limit of ring resonators prepared by the conjugation method could be as low as 31 fM if only the ring resonator region was exposed to target molecules.

2.6 Saturation of probe coverage by conjugation method

The probe density resulting from the conjugation functionalization method described above was further explored by examining different probe attachment conditions, including varying the ion strength in buffer solution, varying the probe attachment time, and varying the probe solution concentration. The results for ion strength and attachment time are discussed below. For sensors tested with ssDNA probe attachment with concentrations of 10 μM, 20 μM, 50 μM and 100 μM in an excess volume of incubation solution (> 200 μL solution), the resulting resonance wavelength shifts were all consistent and did not show any dependence on the probe solution concentration. This result is in agreement with the results presented in Section 2.5 that nearly all probe molecule binding sites are hybridized when exposed to only 100 nM concentration of complementary target molecules.

2.6.1 Varying the ion strength in ssDNA probe solution

It has been demonstrated that when using a traditional ssDNA conjugation method, steric hindrance can be mitigated by increasing the ion strength in the probe ssDNA solution, for example by adding $MgCl_2$ into the probe solution [62]. In order to investigate whether adding $MgCl_2$ into the ssDNA probe solution could affect the resulting resonance shift, three chips with four micro-ring devices each were functionalized in probe solutions with different $MgCl_2$ concentration using the traditional conjugation method. As shown in Figure 2.7, the resonance wavelength shift increased slightly when $MgCl_2$ was added to the probe solution with the shift saturating for $MgCl_2$ concentrations above 50 mM. However, the resulting resonance shift (0.35 nm) is much less than that of micro-rings functionalized using in-situ synthesized probe molecules (1.3 nm).

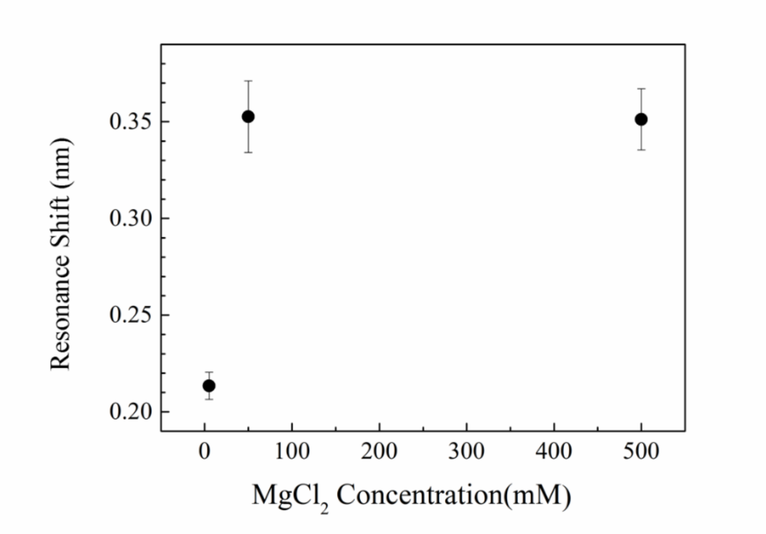

Figure 2.7 Micro-ring resonator resonance shifts after ssDNA probe attachment in different $MgCl_2$ concentrations. Three concentrations were tested: 5 mM, 50 mM and 500 mM. The resonance shift is saturated for a $MgCl_2$ concentration of 50 mM, implying a saturation of the probe surface coverage by the conjugation method.

2.6.2 Varying the probe ssDNA attachment time

In order to determine whether longer ssDNA probe incubation times increased the number of bound probe molecules, the probe attachment time was varied from 1-12 hours, as shown in Figure

2.8. The 12 hours ssDNA attachment results in only a slight increase (~6%) of the resonance wavelength shift on average, implying that the probe surface coverage is nearly saturated after one hour incubation.

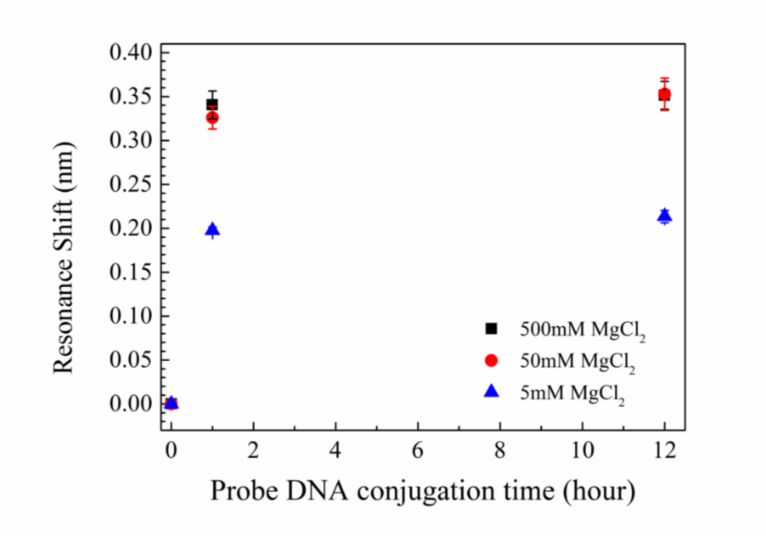

Figure 2.8 Micro-ring resonator resonance shifts after probe attachment for different incubation times. After 12 hours incubation, the average resonance shift only increases by 6%.

2.7 Control experiments

To verify the selectivity of the ring resonators and PhC sensors towards the complementary nucleic acid sequence and to rule out the possibility that measured spectral shifts were due to non-specific binding events, two types of control experiments were performed. Non-specific binding of ssPNA target molecules was tested by exposing the ssPNA to ring resonators and PhCs functionalized only with linker molecules (*i.e.*, no complimentary ssDNA probes). In addition, ring resonators and PhCs functionalized by the in-situ synthesis or conjugation method for ssDNA probes attachment were exposed to non-complimentary ssPNA sequences. Figure 2.9a shows the negative control test results for a ring-resonator prepared to be functionalized by in-situ ssDNA probe synthesis. After silanization with TEOS-HBA and before ssDNA probe synthesis, the sample was incubated in a 100 µM ssPNA target solution. Negligible resonance wavelength red-shift (~0.034 nm) was detected verifying that ssPNA target sequences do not bind to the sensing surface in the absence of complementary ssDNA probe sequences. After carrying out in-situ ssDNA probe synthesis (5'-GGT TCC GAA CGG AGA C-3'), the sample was then exposed to a 100 µM solution containing a completely mismatched ssPNA sequence (ACG AGG ACC ATA GCT A) in DI water. Almost no red-shift (~0.002 nm) of the resonance wavelength was detected confirming the absence of non-specific binding of the mismatched ssPNA sequence to in-situ synthesized ssDNA probe molecules. Figure 2.9b shows the negative control test results for a ring-resonator prepared to be functionalized by the direct conjugation method of ssDNA probe attachment. A negligible resonance red-shift (~0.008 nm) was measured after exposure of ssPNA target molecules to the ring containing silane and linker surface species but no ssDNA probe molecules. After ssDNA probes were conjugated to the sensing surface (same sequence as synthesized probes), the sample was incubated in a 100 µM solution containing completely mismatched ssPNA target in DI water (ACG AGG ACC ATA GCT A). The very small resulting resonance red-shift (~ 0.018 nm) verifies that non-complimentary nucleic acid sequences will not bind to the conjugated ssDNA probe molecules.

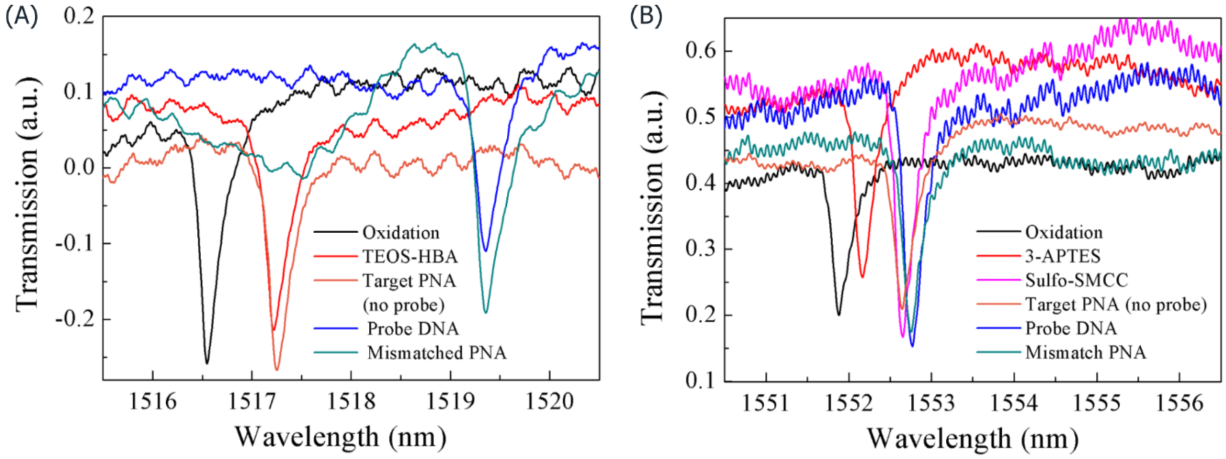

Figure 2.9 Control experiments demonstrating the absence of non-specific binding for ring resonators functionalized using (a) the in-situ ssDNA probe synthesis method and (b) the direct conjugation method of ssDNA probe attachment, as described in the text above.

2.8 Quantification of probe molecule surface coverage

In order to quantify the ssDNA probe density on the Si photonic sensor surfaces, ssDNA fluorescently labeled with FAM6 (absorbance peak at 495 nm; emission peak at 520 nm) were utilized for both the in-situ synthesis and direct conjugation approaches. The fluorescently labeled ssDNA probes were attached to planar Si samples for these measurements instead of the Si photonic structures for ease of examination by a fluorescent microscope (*i.e.*, uniform focal depth and attachment over a large area). Florescence images were taken using a Nikon AZ100 M upright florescence microscope. As shown in Figure 2.10a, the fluorescence intensity of the in-situ synthesized ssDNA probes is approximately 4 times higher than that of the ssDNA probes immobilized by direct conjugation, as estimated using image processing software (ImageJ). This implies that the surface coverage of in-situ synthesized ssDNA probes is at least 4 times higher than directly conjugated ssDNA probes. Note that the sample prepared by direct conjugation of the fluorescently labeled ssDNA probes exhibited multiple bright dots in the fluorescence image attributed to cluster formations, as shown in Figure 2.11, which may result from silane aggregation; these ssDNA clusters are likely not fully accessible for hybridization [63, 64]. The absolute probe density on the surface cannot be quantified solely from the brightness of fluorescence images since it is difficult to obtain a known standard surface density of the FAM6 fluorescence dye. When known concentrations of FAM6-labeled DNA molecules were drop cast onto Si wafers, the resulting coffee ring effect (Figure 2.12) precluded accurate image analysis; ssDNA molecules were not evenly distributed over the Si surface and exhibited significant aggregation towards the edges of the sample. Therefore, to quantify the surface area coverage of ssDNA probe sequences, measurements were performed in the solution phase as described below. Figure 2.10b shows the absorbance spectra for FAM6-labeled ssDNA in solution at various concentrations as measured using a Varian Cary 5000 UV−VIS−NIR spectrophotometer at a step size of 0.5 nm. The resulting calibration curve that links the peak absorbance intensity at 495 nm with FAM6 concentration is presented in Figure 2.13.

In order to obtain a solution-phase absorbance measurement of the FAM6-labeled ssDNA probes attached to the Si sample, the ssDNA was cleaved from the surface. Accordingly, a slightly different surface chemistry for the directly conjugated ssDNA probes was employed, as described in Figure 2.14. Experiments were performed to verify that the average resonance shifts due to ssDNA probe and ssPNA target attachment did not change when the cleavable linker was utilized. Hence, the estimated surface density of ssDNA probes estimated by the solution phase measurement is indicative of the surface density of ssDNA probes on the Si photonic sensors functionalized by the direct conjugation approach for probe molecule attachment. By comparing

Figure 2.10b and Figure 2.13, the concentration of the cleaved ssDNA probes is estimated to be ~ 130 nM. Note that the presence of the second absorption peak near 343 nm in Figure 2.10b for the solution containing molecules cleaved from the Si surface corresponds to the presence of cleavable linker molecules that did not react with ssDNA probes (see Figure 2.14 for details), and confirms that the directly conjugated ssDNA probe molecules only attach to a fraction of the available linker sites on the sample surface. Since the surface area of the Si sample onto which the ssDNA probes were attached was approximately 3.6 cm^2 and the total volume of solution used for the measurement was 250 μL, the overall surface density of the directly conjugated ssDNA probes is estimated to be 5×10^{12} /cm^2. This surface density is consistent with other reports of DNA surface densities on planar surfaces [65-67]. Based on the intensity comparison of fluorescence images in Figure 2.10a, and the resonance shift data presented in Figure 2.2 and Figure 2.3, the ssDNA probe surface density on Si photonic structures functionalized by the in-situ synthesis method is estimated to be at least 2×10^{13} /cm^2.

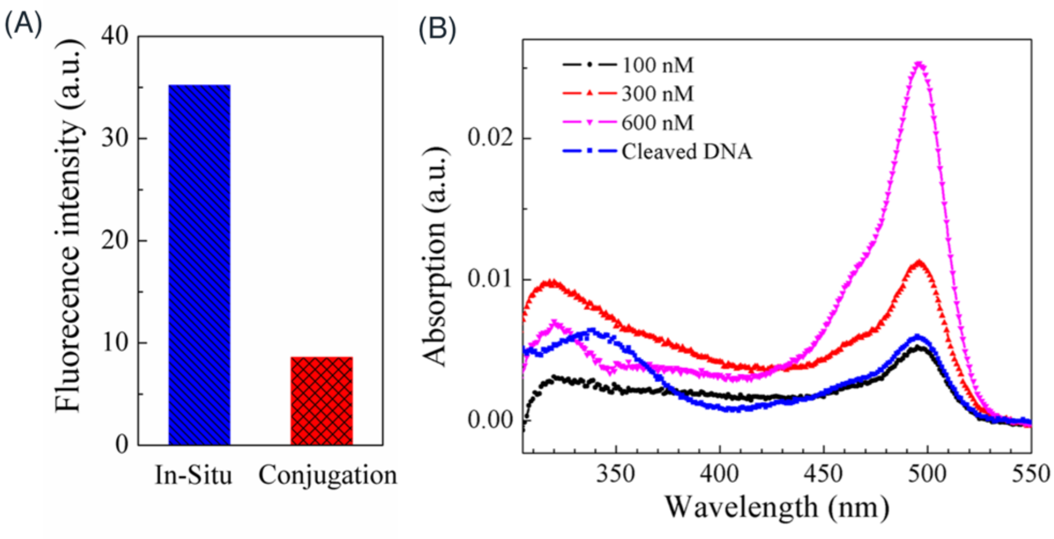

Figure 2.10 (A) Comparison of fluorescence intensity of Si samples functionalized with in-situ synthesized ssDNA probes and directly conjugated ssDNA probes that have been fluorescently tagged with FAM6 dye. Fluorescence images are shown in Figure 2.11. (B) Absorbance spectra of solutions with known concentrations of FAM6-labeled DNA (100 nM, 300 nM, 600 nM) and the solution containing molecules cleaved from the surface of a Si sample functionalized with directly conjugated FAM6-labeled probe DNA molecules (cleaved DNA). The concentration of probe DNA conjugated to the Si surface (~ 130 nM) is obtained through comparison to the intensity of the FAM6 absorption peak (495 nm). Reprinted with permission from Ref. [18]. Copyright 2014 American Chemical Society.

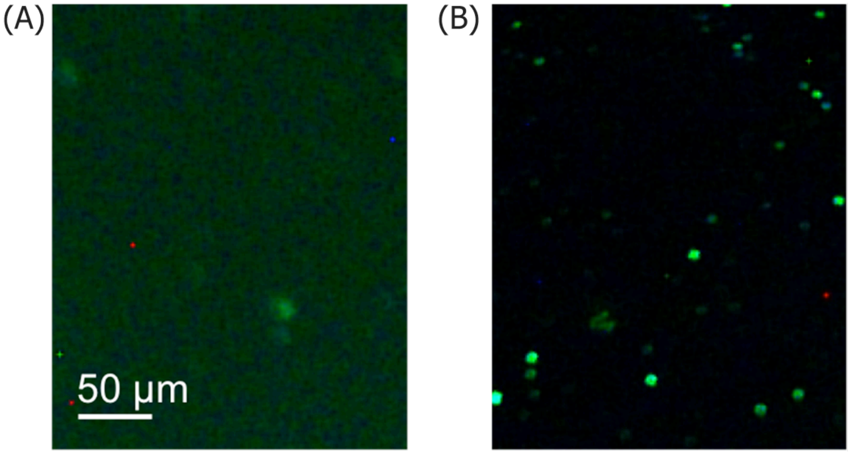

Figure 2.11 Fluorescence images of substrates prepared with (a) in-situ synthesized and (b) directly conjugated FAM6-labeled fluorescent ssDNA.

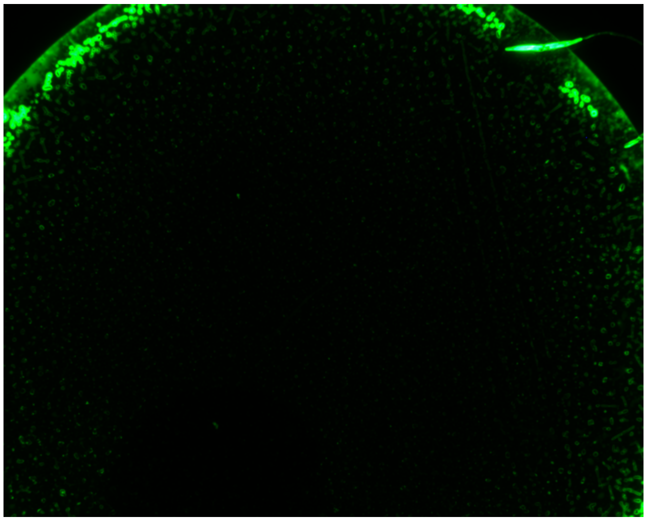

Figure 2.12 "Coffee ring" effect of drop-cast FAM6-labeled fluorescent ssDNA on Si surface as imaged in a fluorescence microscope.

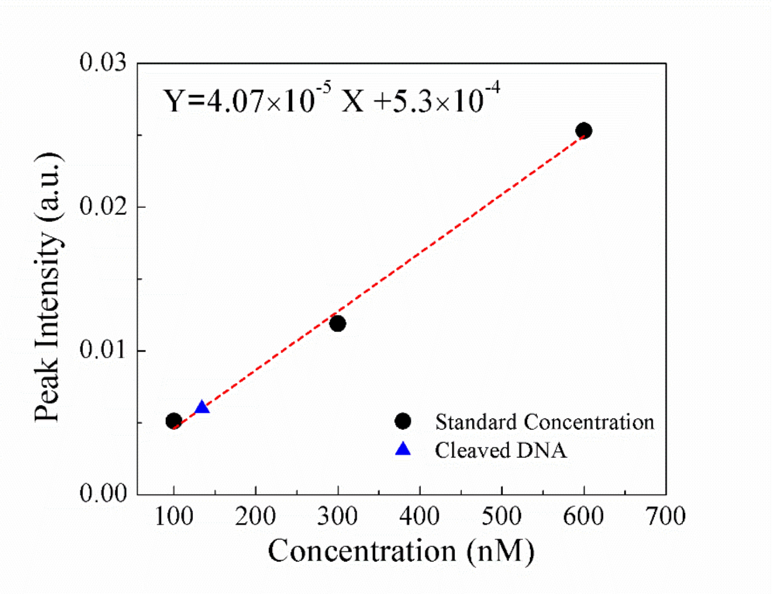

Figure 2.13 Calibration curve linking peak absorbance intensity measured at the characteristic absorption peak of the FAM6 dye to known concentrations of FAM6-labeled ssDNA in solution. A linear fit of the data and associated equation are shown. Based on comparison to this data, the concentration of ssDNA cleaved from a Si sample functionalized by the direct conjugation approach with a cleavable linker is estimated to be 134 nM.

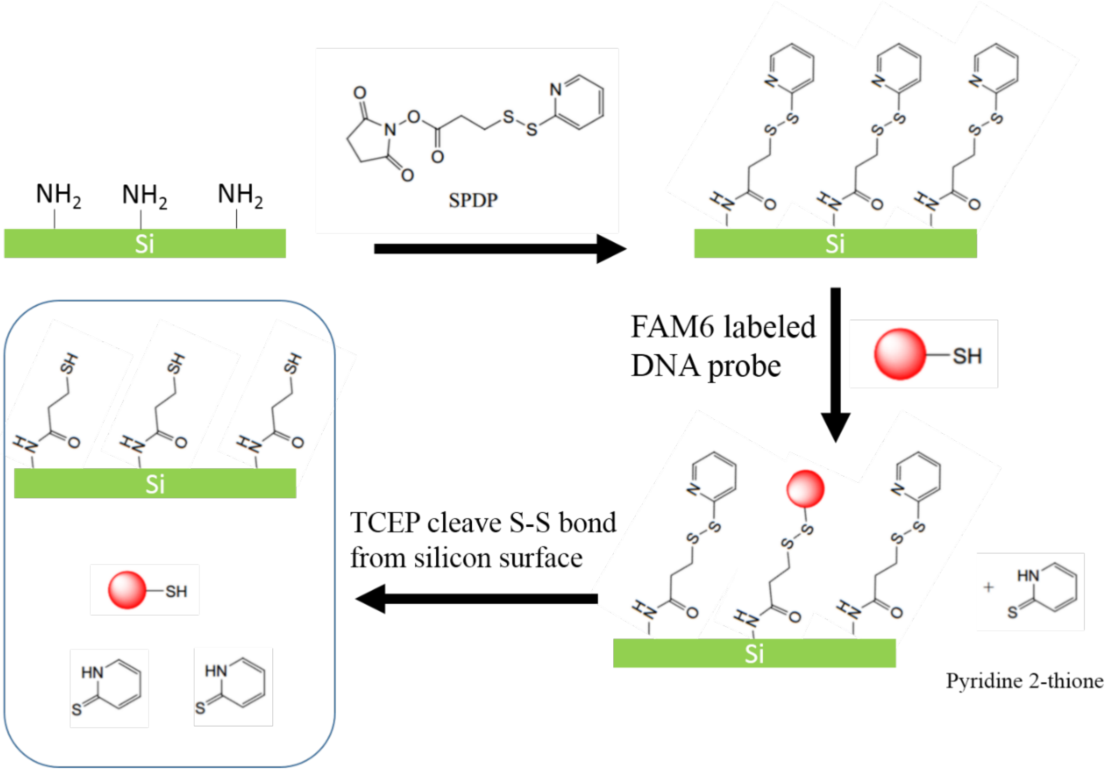

Figure 2.14 Schematic representation of the steps involved in cleaving FAM6-labeled ssDNA from an amine-terminated (3-APTES) Si surface following covalent immobilization through the cleavable SPDP linker molecule. Complete details are found in Section 2.3.2. Briefly, SPDP is attached to 3-APTES on the Si surface. FAM6-labeled ssDNA probe molecules are then attached to the SPDP linkers. Pyridine 2-thione groups on the SPDP molecules are displaced when the ssDNA is attached. Next, a TCEP solution is used to cleave the SPDP molecules, releasing the FAM6-labeled probe DNA into solution. Pyridine 2-thione is also present in the solution since not all SPDP sites capture a ssDNA probe molecule. The concentration of ssDNA probe molecules and pyridine 2-thione can be determined by measuring the absorbance at 495 nm and 343 nm, respectively.

2.9 Faster response time with increased probe molecule surface coverage

In order to investigate the influence of probe molecule surface coverage on sensor response time, microfluidic flow cells were attached to the micro-ring and PhC sensors. A mold of the flow cell was formed by optical lithography on a 100 μm thick SU-8 layer (SU-8 2100) on a 4-inch Si wafer. A mixture of PDMS and curing agent (10:1) was poured onto the surface of the mold to form a PDMS flow cell which was cured in an oven at 60°C for 4 hours. The cured PDMS flow cell was then carefully peeled off the mold and cut out using a graver. An 18 gauge punch was used to make holes at each end of the channel for the inlet and outlet. To achieve optimized adhesion, the bottom surface of the PDMS flow cell was treated with oxygen plasma for 25 s, and then an adhesive curing glue (a 2:1 mixture of PDMS and curing agent) was uniformly applied. The PDMS flow cell channel was then aligned with the Si photonic devices (micro-rings or PhCs) under an optical microscope and attached to the silicon-on-insulator (SOI) substrate. Next, the SOI substrate and PDMS flow cell were clamped and cured in an oven for 4 hours at 60°C. Finally, two connection pins (outside diameter 16 gauge) with tubing were plugged into the inlet and outlet of the PDMS shell, as shown in Figure 2.15.

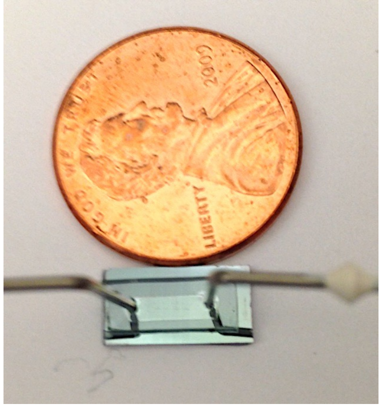

Figure 2.15 Photograph of microfluidic channel integrated with Si micro-ring resonators.

The measured transmission spectra of the Si photonic sensors integrated with the PDMS microchannels can be monitored in real-time to ascertain the influence of probe molecule surface density on the binding kinetics of target molecules. A 1 μM complimentary ssPNA solution was injected at a constant flow rate of 0.003 mL/min into the flow cells. The time-dependent resonance shifts of Si micro-ring resonators functionalized with either in-situ synthesized ssDNA probe molecules or directly conjugated ssDNA probe molecules are shown in Figure 2.16**.** Following ssPNA hybridization, non-specifically bound ssPNA molecules were rinsed away by flowing DI water through the microchannels; small blue shifts can be observed in Figure 2.16 for both ring resonator samples following the rinsing. The kinetic binding rates for ssPNA target sequences onto the Si photonic sensors were obtained by a simple linear fit to the two time-dependent resonance shift curves in the pre-saturation regime (first 40 minutes). For the case of the ring resonator functionalized with in-situ synthesized ssDNA probes, $\Delta\lambda/\Delta t$ = 9.6 pm/min while for the ring resonator functionalized with conjugated ssDNA probe molecules $\Delta\lambda/\Delta t$ = 2.7 pm/min. Accordingly, the kinetic binding rate and response time of Si photonic biosensors is approximately 3.5 times faster when the sensor is functionalized using the in-situ synthesis method for probe molecule functionalization that allows for higher probe molecule coverage than direct conjugation approaches. Faster binding rates can likely be achieved by increasing the flow rate. Note that in this flow cell experiment, the resonance shift for ssPNA target hybridization on a Si ring resonator functionalized with in-situ synthesized ssDNA probe sequences is smaller than the average resonance shift reported in Figure 2.2. This smaller resonance shift is attributed to a loss of ssDNA probe molecules that likely occurs during attachment and curing of the PDMS microfluidic channel. In future experiments, it may be possible to modify the DNA synthesizer tool to accommodate attachment of in-situ synthesized ssDNA probe molecules delivered through flow cell. For the ring resonator functionalized by directly conjugated ssDNA probes, all surface functionalization steps were carried out by microfluidics delivery within the PDMS flow cell and the resulting ssPNA target resonance shift is comparable to the average resonance shift reported in Figure 2.2. By examining the resonance shifts upon ssPNA target molecule binding for the two different functionalized ring resonators in Figure 2.16 (~ 3.2:1 for in-situ synthesized:directly conjugated ssDNA probes functionalization), and assuming the probe surface coverage ratio is similar to the ssPNA resonance shift ratio, it can be concluded that the kinetic binding rate scales approximately with the bio-receptor surface area coverage. Complete integration of microfluidics with Si photonic sensors functionalized with in-situ synthesized ssDNA probes could enable individual array elements on multiple sensors to be functionalized with the same probe sequences at same time. This would facilitate the functionalization of multiple array sensors with different sequences in the same amount of time required to functionalize a single array sensor with multiple sequences.

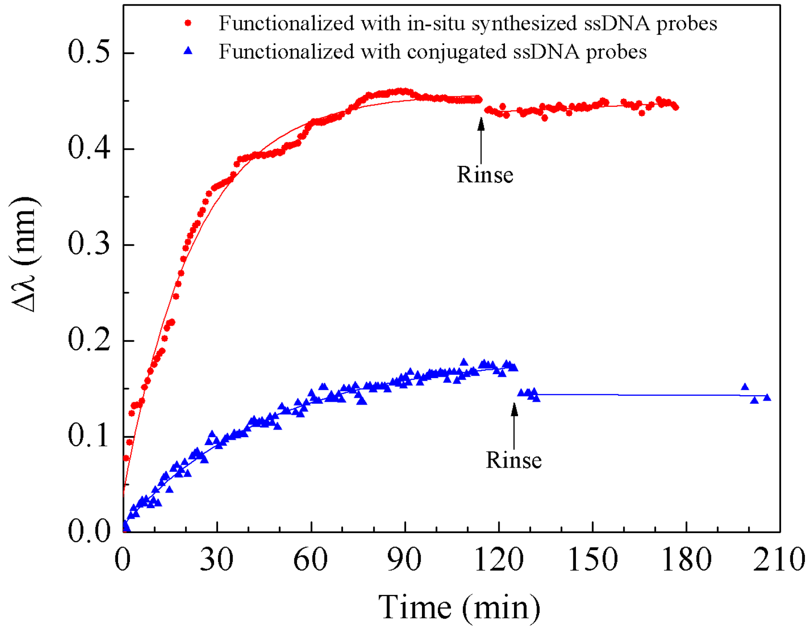

Figure 2.16 Kinetic binding curves for ssPNA target sequences using microfluidic channels as an analyte delivery system to 5 μm radius Si ring resonators functionalized with either in-situ synthesized or directly conjugated ssDNA probe molecules. The solid lines connecting data points taken before the rinse step indicate exponential fits of the kinetic binding rates of ssPNA for the two different rings. The faster response time of the ring functionalized with in-situ synthesized probes is proportional to the increased probe surface coverage on that ring. Reprinted with permission from Ref.[18]. Copyright 2014 American Chemical Society.

2.10 Conclusion

We have demonstrated the importance of achieving high probe molecule surface area coverage over the active sensing regions of Si photonic devices that are progressively utilizing smaller footprints and realizing increased modal confinement over sub-wavelength dimensions. An in-situ ssDNA probe synthesis technique was utilized to increase the surface coverage of ssDNA probe molecules by 5-7 times on Si micro-ring resonators and PhCs compared to standard probe molecule conjugation techniques. The enhanced probe surface coverage led to a 5-7 times enhancement in the measured resonance wavelength shifts upon target molecule capture, suggesting that the probe molecule density is below that which would cause steric hindrance of hybridization events. Fluorescence measurements quantified the density of the in-situ synthesized ssDNA probes to be on the order of 10^{13} /cm^2. The enhanced probe molecule coverage achieved by using the in-situ synthesis technique also led to a more than 3-fold reduction in the response time of the Si photonic sensors. These results suggest improved detection sensitivities and response times for sub-nM target biomolecule concentrations are achievable. Integration of the label-free, functionalized photonic devices with microfluidics and high-throughput multiplexing via cascaded devices has exciting possibilities for point-of-care, lab-on-a-chip sensor development.

CHAPTER 3

ENHANCING THE SENSITIVITY THROUGH INCREASED MODAL OVERLAP

3.1 Introduction

With improvements in microfabrication technologies over the past decade, tremendous advancements have been made in the design and fabrication of high quality, micron-scale, silicon optical ring resonators [68]. The increased light-matter interaction length in these resonant devices compared to ridge waveguides or fibers makes them highly sensitive to chemical and biomolecular binding events on the device surfaces [69]. Over the past few years, micro-ring resonator (MRR) sensors have been utilized for detecting a variety of different biomolecules including proteins, microRNAs, DNA and antibodies with sensitivities ranging from 10 pM for antibodies to 0.5 nM for DNA [70-72]. The high detection sensitivities together with CMOS compatible fabrication technology, small device footprint, well-characterized silicon surface chemistry, and lab-on-chip integration capability have resulted in their emergence as front-runners in the label-free, point-of-care diagnostics market [34, 73, 74]. Leading industry standard labeled and label-free detection techniques such as enzyme-linked immunosorbent assay (ELISA) and surface plasmon resonance (SPR) also demonstrate similar detection sensitivities [75-77], but are incompatible with CMOS fabrication technologies and are not scalable down to low-cost lab-chip sensor arrays. Moreover, silicon MRR sensors can achieve a significantly higher level of multiplexed detection than ELISA and SPR through larger sensor array strategies that enable more rapid and higher-throughput molecular detection [70, 78]. Label-free sensors based on silicon photonic crystal resonators have also been reported to achieve ultra-low detection sensitivities [79, 80]; however, the complexities of photonic crystal fabrication, higher manufacturing costs and increased sensitivity to false positives have prevented their more widespread use as label-free sensors.

In this Chapter, we report on design improvements for MRR sensors. Most MRR sensors reported to date utilize a supported structural framework wherein the ring resonator is fabricated directly atop a SiO_2 substrate on a standard silicon-on-insulator (SOI) wafer [81]. This approach results in an asymmetrical optical mode distribution with a significant fraction of the optical mode present in the underlying SiO_2 substrate where it is inaccessible for the attachment of target analytes. In our approach, suspending the MRR sensors and allowing molecules to attach to both the top and bottom of the MRRs enables a near 60% improvement in the achievable mode overlap with target analytes. The structural illustrations of both supported and suspended MRRs are shown in Figure 3.1a and b respectively. Using suspended MRRs, we experimentally demonstrate a 3-fold enhancement in bulk detection sensitivity and a 2-fold increase in the sensitivity of detecting Herceptin, a clinically relevant humanized monoclonal antibody (mAb) used for the treatment of certain types of metastatic breast cancer that overexpress anti-human epidermal growth factor receptor-2 (HER2) protein and/or show HER2 gene amplification on tumor cells [82-84]. Compared to the most widely used assay for the detection of Herceptin – ELISA – which requires the use of enzymatic labels, long reaction times and trained personnel, suspended MRRs are much more promising for high-throughput, rapid response time diagnostics due to their compatibility with on-chip sensor arrays and microfluidic systems.

3.2 Design and Simulation

Label-free optical biosensors typically detect and quantify analyte based on measuring spectral changes, with the most sensitive sensors relying on resonant optical structures with narrow linewidth spectral features. As discussed in Section 1.2, Equation 1.21 describes the light-matter interaction and can be applied to relate the shift in resonance frequency of an optical structure such as a micro-ring resonator sensor to the strength of the electric field ($\boldsymbol{E}^{(0)}$), the magnitude of the refractive index change ($\Delta\varepsilon$), and the degree of spatial overlap of the electric field with chemical and biological species captured by the sensor surface (V). Optimizing each of these three parameters will result in increased device sensitivity and reduced detection limits.

In general, TM-mode MRRs have much higher sensitivities for biosensing applications in comparison to TE-mode MRRs because a larger fraction of their optical fields are present outside of the silicon waveguide where target biomolecules can be captured, leading to increased spatial overlap (V in Equation 1.21) of the electric field and refractive index perturbation [85]. However, for traditional TM-mode MRRs fabricated on SOI wafers (shown schematically in Figure 3.1a), the SiO_2 substrate creates an asymmetric index profile along the out-of-plane direction. The upper surface of the ring resonator is exposed to air while the lower surface is enclosed by the SiO_2 substrate. This leads to an asymmetric TM mode distribution with a higher percentage of the mode distribution concentrated within the inaccessible underlying SiO_2 substrate layer. As shown in Figure 3.1c, in conventional TM-mode MRRs and waveguides (green squares and trend line), less than 20% of the optical energy is accessible for interaction with analytes. Moreover, it is not possible to increase the modal interaction with analytes bound on the top surface of traditional MRRs by simply reducing the waveguide thickness and delocalizing the optical mode. As shown in Figure 3.1d, when the waveguide thickness is decreased, the optical mode becomes increasingly delocalized but the asymmetric refractive index profile leads to an increasingly asymmetric field distribution where most of the mode resides near the silicon-SiO_2 interface and little enhancement to the modal intensity near the silicon-air interface that is accessible for target molecules can be achieved.

In order to increase modal overlap with target analytes in MRRs, we consider the use of suspended TM micro-ring resonators (shown schematically in Figure 3.1b), wherein 1) the symmetric refractive index profile of the sensor in the out-of-plane direction results in a symmetric optical mode distribution that is more amenable to design optimizations that increase the optical mode distribution present at the silicon-air interfaces of the MRRs and 2) opening up access of target analytes to the bottom surface of the MRRs directly allows increased spatial overlap of the optical mode and target molecules.

In order to estimate the fraction of the optical mode extending into the air region surrounding the MRRs, finite element method (FEM) simulations were carried out in the COMSOL Multiphysics software package. First, the waveguide effective index for supported and suspended MRRs was calculated. Next, a small imaginary contribution to the refractive index of air ($\kappa = 0.01$) was added to the material parameters for air. Then, the waveguide effective index was recalculated for the MRRs. The ratio of the imaginary part of the recalculated waveguide effective index to the added imaginary part of the refractive index of air is taken to be the approximate percentage of the optical mode of the MRR that extends into the air region because the only source of the imaginary contribution to the effective index arises from the artificially added complex index of air.

The blue circles and trend line in Figure 3.1c shows increased fraction of the optical mode in air that accompanies a reduction of the thickness of suspended MRRs. Unlike the trend for the supported MRRs, the mode of the suspended MRRs continues to be delocalized into the surrounding air medium in a symmetric manner with decreasing waveguide thickness (Figure 3.1d). For a TM-mode MRR with a waveguide thickness of 220 nm, nearly 75% of the optical energy can spatially overlap with target analytes. In comparison, a supported TE-mode waveguide achieves only 5% mode overlap, a suspended TE-mode waveguide achieves a near ~8% overlap, and a supported TM-mode waveguide achieves a mode overlap of ~14%. The detection sensitivities of MRRs are expected to scale directly with the percentage of mode overlap with target analytes. However, increasing the fraction of the mode that resides in the air region also results in higher propagation losses, reduced temporal confinement and, thus, lower Q-factor resonances with broader linewidths. As a result, there exists a trade-off between achievable mode overlap with target analytes and high Q-factors, which are important for achieving low detection limits. We therefore choose a waveguide thickness of 270 nm to allow for a large mode overlap of ~43% (3.3 times higher than supported MRRs) while also maintaining reasonable Q-factors of ~20,000.

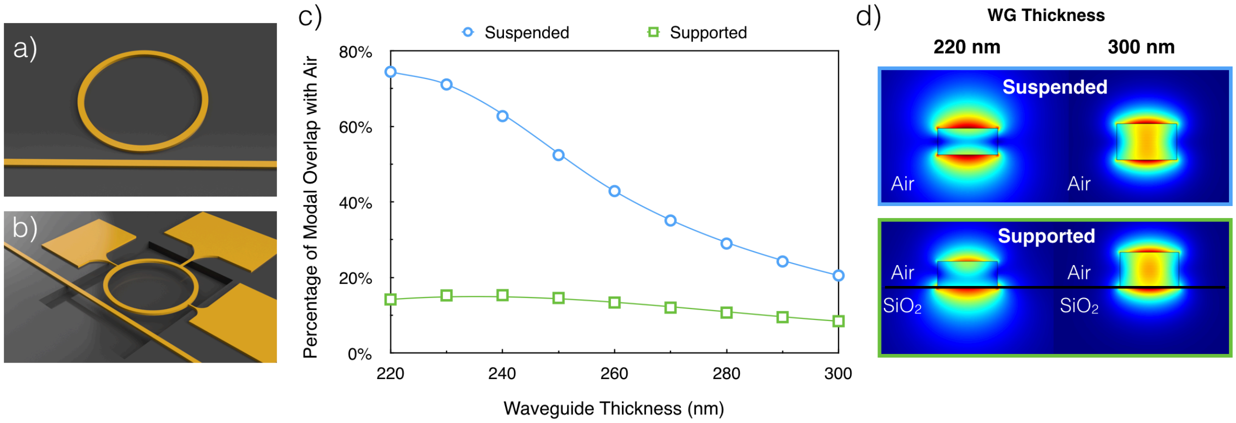

Figure 3.1 Schematic of (a) supported and (b) suspended micro-ring resonators. (c) Percentage of optical mode overlap in air region around suspended and supported TM-mode waveguides with respect to changes in the thickness of the waveguides. (d) TM-mode distributions for suspended and supported TM-mode waveguides with thicknesses of 220 nm and 300 nm.

3.3 Fabrication

A CMOS compatible fabrication process was followed for the suspended TM-mode MRRs implemented in this work. A SOI wafer (SOITEC) with a silicon top layer of 270 nm and a buried oxide layer (BOX) of 3 μm was chosen to accommodate the waveguide dimensions required for TM mode MRRs operating near 1.55 μm. First, 300 nm thick photoresist (ZEP 520A) was spin coated onto the wafer followed by a 180 °C, 2 minutes bake on a hot plate. Electron-beam lithography (JEOL9300F) was then used to expose the designed pattern at 100 kV voltage, 400 C/cm^2. One of the challenges to achieving small features, such as the nano-trusses employed to support the suspended rings, using electron beam lithography is the proximity effect. Electron backscatter from underneath the photoresist can over-dose the surrounding patterns, resulting in a non-uniform width of the nano-trusses. To address this effect, Monte Carlo simulations were performed to model the dosage distribution after electron scattering. Then, the actual dosage applied during exposure was adjusted accordingly to compensate for the scattered electrons. Following exposure, the sample was developed in xylene for 30 seconds and rinsed thoroughly with isopropyl alcohol (IPA). The photoresist pattern was then transferred into the silicon layer by reactive ion etching (Oxford PlasmaLab 100) using $C_4F_8/SF_6/Ar$ gases to completely etch the exposed portion of the silicon layer. Photoresist residue was then stripped upon exposure to O_2 plasma. At the end of this process, the fabrication of traditional, supported MRRs was complete.

To fabricate suspended MRRs, a wet etch step using buffered oxide etch (BOE) was performed on the supported MRRs. The sample was first cleaned with IPA and then baked on a hotplate at 115^{o}C for 10 minutes to evaporate any adsorbed water and IPA residue from the surface. Next, 1.3 μm of photoresist (AZ1513) was spin coated onto the sample at 4000 rpm for 45 seconds, and the sample was soft baked on a hotplate at 95^{o}C for 50 seconds. Optical lithography (Karl Suss MA6) was then carried out to selectively open an etch window in the photoresist over the ring region. An AZ MIF developer was used for 1 minute and the sample was then placed on a hotplate for 10 minutes at 115^{o}C to facilitate photoresist crosslinking (i.e., hard bake) after development. Finally, the sample was soaked in BOE for 8 minutes to etch ~ 1 μm of the BOX layer. The sample was then rinsed with DI water and dried under nitrogen.

Figure 3.2 shows the fabricated structure after electron-beam lithography and the wet-etch step. The ring radius and width are approximately 5 μm and 500 nm respectively. The trusses are about 100 nm in width and 260 nm in height. The high aspect ratio gives a large stiffness with respect to vertical displacement. Therefore, the trusses are able to provide good mechanical support to the entire suspended ring structure without any noticeable bending or fracture. The resonator is about 1 μm above the SiO_2 layer. Taking into account that the evanescent field extends out to ~200 nm from the lower ring surface, a 1 μm separation from the underlying substrate is sufficient to achieve enhanced light-matter interaction upon molecular binding events at the now exposed lower waveguide surface. The design of the suspended micro-ring resonator structure for sensor applications must consider how the necessary supporting trusses lead to both increased scattering and thus reduced light-matter interaction (*i.e.*, lower device sensitivity) as well as increased mechanical stability of the suspended ring for withstanding multiple wetting and drying steps associated with sensor functionalization and molecular detection events. Some scattering seen near the supporting trusses may account for slight scattering losses in FDTD simulations. Further optimizations in the placement and design of the supporting trusses may reduce these losses.

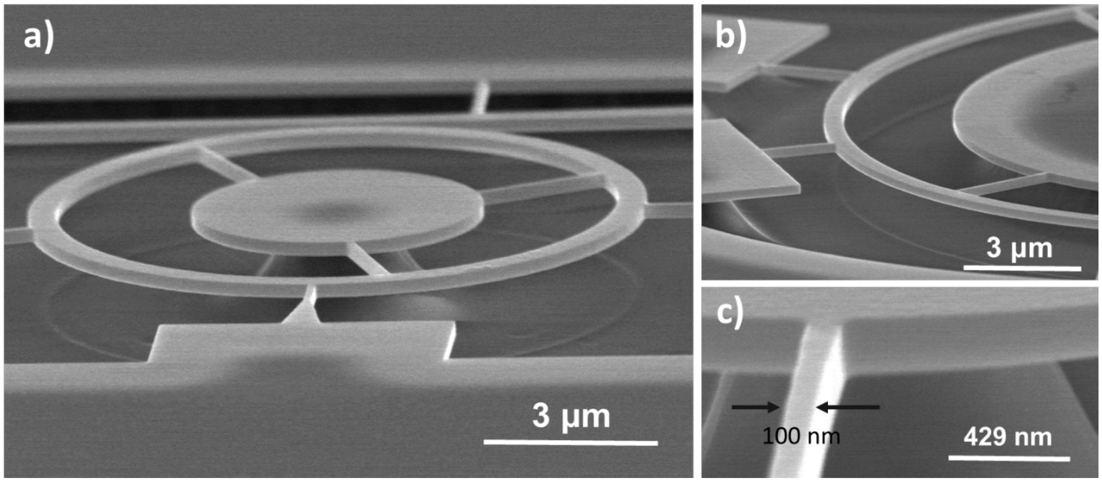

Figure 3.2 (a – b) SEM images of a 10 μm diameter suspended microring resonator. (c) The width of a supporting truss is approximately 100 nm. The height is approximately 260 nm for the supporting trusses and the microring resonator. A designed aspect ratio of 2.6 for the supporting trusses provides sufficiently robust mechanical support for the suspended optical biosensor and is capable of withstanding all incubation, rinsing, and drying steps involved in the assay development.

3.4 Bulk Refractive Index Sensitivities

Determination of the bulk refractive index sensitivity of the suspended ring resonator sensor chips was carried out by comparing the sensitivity improvements over traditional supported ring resonator sensor chips when exposed to varying concentrations (1%, 3%, 5%, 7% and 9%) of salt solutions. Figure 3.3 shows the comparative experimental performance for both types of sensor chips in terms of the measured resonance wavelength shifts for each solution. The suspended ring resonator sensors are seen to demonstrate a near 3-fold improvement in detection sensitivities (310 nm/RIU) over the supported ring resonator sensors (115 nm/RIU). This is consistent with the simulation results as well (Figure 3.1a). The quality factor for both supported and suspended TM MRRs is approximately 30,000.

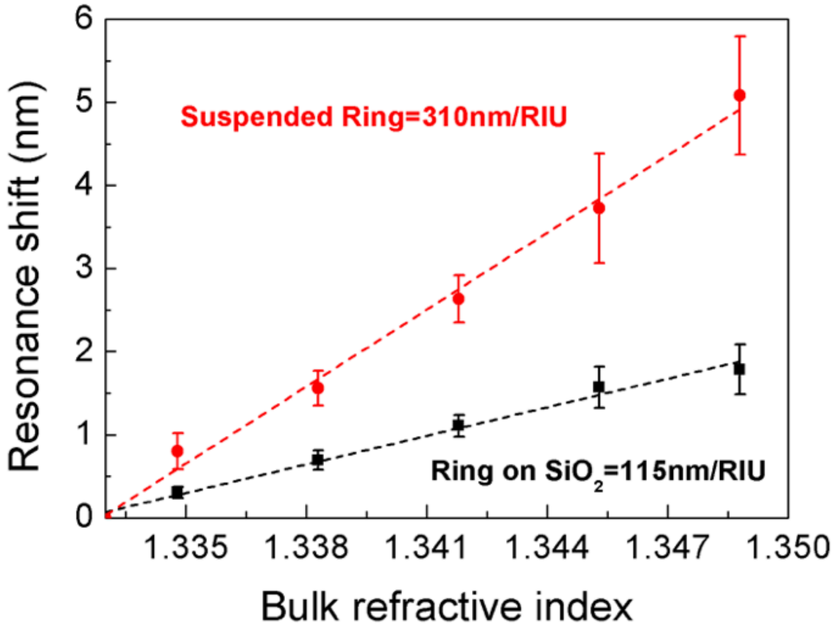

Figure 3.3 Bulk refractive index sensitivity comparison for suspended and supported micro-ring resonators. The resonance wavelength shift as a function bulk refractive index change for suspended micro-ring resonators is larger than that for supported micro-ring resonators.

3.5 Specific Detection of Heat Denatured Herceptin

3.5.1 Materials

Human therapeutic antibodies Herceptin (Trastuzumab) and Avastin (Bevacizumab) were provided as reconstituted solutions (21 μg/μL) Herceptin and (12.5 ng/μL) Avastin respectively in Sterile Water for Injection (SWFI) by the Vanderbilt University Medical Center pharmacy. All other chemicals were used without further purification. Reagents used in this study include 3-aminopropyltrimethoxysilane (3-APTES, 99% Acros Organics), 25% aqueous glutaraldehyde (EM grade Polysciences), 3 M ethanolamine (>99% ethanolamine, Aldrich), and sodium cyanoborohydride (5 M cyanoborohydride, 1 M NaOH, Aldrich).

3.5.2 Surface chemical functionalization of micro-ring resonators

The fabricated MRR chips were thermally oxidized at 500 °C for 15 min to provide a chemically inert, oxidized surface that would enable the covalent attachment of amine terminated 3-aminopropyltriethoxysilane (APTES) linker molecules on the sensor surface. Following oxidation, the samples were immersed in a freshly prepared piranha solution for 15 min to ensure a chemically clean surface prior to the attachment of the APTES linker molecules. The samples were then thoroughly rinsed in DI water and dried under nitrogen. Next, the chips were incubated in a freshly prepared 2% APTES solution in anhydrous toluene for 10 min. The excess APTES was thoroughly rinsed from the chips three times with ethanol and de-ionized (DI) water, dried under nitrogen flow and baked in an oven at 120 °C for 20 min to increase the cross-linking density followed by a 1 hr soak in DI water to remove any remaining unbound APTES molecules. The samples were then thoroughly rinsed with ethanol and dried under nitrogen. The amine terminated sensor chips were then exposed to an aqueous glutaraldehyde solution, which is a homobifunctional cross-linker.

Each chip (~ 1 cm × 5 cm) was exposed to 10 μL of a 2.5% glutaraldehyde solution, formed by mixing 50 μL of 25% aqueous glutaraldehyde (EM grade, Polysciences) with 950 μL of HEPES buffer (20 mM HEPES, 150 mM NaCl, 5 mM EDTA, pH = 7.4), for 30 min. Excess glutaraldehyde solution was pipetted off the sensor surface and 1 μL of sodium cyanoborohydride in 100 μL of HEPES buffer was pipetted onto the sensor surface in order to stabilize the Schiff base (C=N) formed during reaction of the aldehyde group with the amine group. After 30 min of exposure to the reducing agent, the chips were thoroughly rinsed with HEPES buffer and DI water to remove any unreacted glutaraldehyde molecules from the sensor surface and dried under nitrogen. Following aldehyde surface functionalization, the sensor chips were exposed to 10 μL of a 10 μM streptavidin solution in PBS buffer for 30 min. An incubation time of 30 min was found to be sufficient for the attachment of streptavidin molecules across the sensor surfaces. The Schiff based formed during the attachment of streptavidin to the aldehyde functional groups on the sensor surface was similarly stabilized by exposure to the sodium cyanoborohydride reducing agent for 30 min. The chips were then thoroughly rinsed with DI water and dried under nitrogen. Any remaining unreacted aldehyde groups were blocked by exposing the sensor surfaces to a 3 M ethanolamine (> 99% ethanolamine, Aldrich) solution for 30 min. The chips were then rinsed with DI water and, dried under nitrogen, and the transmission spectra of the sensors were measured. In order to further ensure stability of the sensing surface, all samples were incubated for extended durations of 2 hrs in DI water to remove any excess and unreacted APTES, aldehyde and streptavidin molecules. The chips were then rinsed with DI water, dried under nitrogen and re-measured. This step is referred to as a rinse step.

3.5.3 Immobilization of 2B4 single chain fragment variable recombinant antibodies

The 2B4 single chain fragment variable (scFv) recombinant antibodies, specific to the heavy chain CD3 region of Herceptin, were selected and then biotinylated according to procedures reported earlier [86, 87]. Briefly, a phage-displayed recombinant antibody library was used to develop the 2B4 scFv antibody. Recombinant scFvs are the smallest possible antibody fragments that contain functional domains of antibodies necessary for antigen-binding activity. Genetically engineered scFv antibody fragments have good antigen-binding activity and can be inexpensively synthesized, making them highly suitable for antigen-specific immunoassays [86]. Streptavidin-functionalized MRR chips were exposed to 10 μL of a 145 ng/μL biotinylated-2B4 probe molecule solution for 1 hr. Unbound biotinylated-2B4 molecules were then rinsed away with DI water and the samples dried under nitrogen. In order to ensure the chemical stability of the functionalized sensor surfaces, the 2B4-functionalized sensors were additionally incubated in DI water for 2 hrs to ensure removal of any unreacted residual linker molecules. The samples were again rinsed and dried under nitrogen, and were then ready for exposure to the target Herceptin mAb molecules.

3.5.4 Preparation of heat-denatured Herceptin and Avastin

First, 1 mL of the as-received 21 μg/μL Herceptin was diluted down to a 100 nM concentration in HEPES buffer and then denatured at a temperature of 80 °C for 10 min, following prior work [86]. Specific detection of the Herceptin target molecules was carried out by pipetting 10 μL of 100 nM heat denatured Herceptin solution onto the biotinylated-2B4 functionalized MRRs for an incubation time of 1 hr. Unbound Herceptin molecules were then rinsed away with DI water and ethanol and the samples dried under nitrogen.

For use in control experiments, 100 μL of a 12.5 ng/μL Avastin solution was diluted down to a 100 nM concentration using HEPES buffer. Heat denaturation of Avastin was then performed at 80 °C for 10 min. Biotinylated-2B4 functionalized MRRs were exposed to 10 μL of a 0.125 ng/μL Avastin solution for 1 hr. The samples were then rinsed with DI water and ethanol and dried under nitrogen.

3.5.5 Experimental Results

In order to determine the detection sensitivity enhancement of suspended TM-mode MRRs for surface-based molecular sensing, experiments were carried out to investigate label-free, specific detection of heat denatured Herceptin using TM-mode, suspended and supported MRR sensors. Figure 4a-b shows the increase in resonance wavelengths upon covalent attachment of APTES, aldehyde and streptavidin for both the supported and suspended TM-mode MRR sensors, respectively. The magnitude of the resonance wavelength shift directly correlates to the size and coverage density of the molecules. The rinse step described earlier in Section 3.5.2 is seen to result in an approximately ~ 1.5 nm and ~ 1.0 nm blue-shift in resonance wavelengths for the suspended and supported MRR sensors respectively (not shown). Since it is not possible to determine which molecules were removed during the rinse step, the magnitude of the resonance shifts shown for each molecule attachment in Figure 3.4a and b should be considered as an upper bound. We note that the suspended MRR sensors demonstrate excellent mechanical stability throughout the experiments, withstanding the multiple, prolonged rinsing and drying steps described in Section 3.5.2.

After the rinse step, 2B4 scFv antibodies were covalently immobilized on the silicon MRR surfaces to enable selective binding to Herceptin's heavy chain CDR3. The small size of these single chain fragment variable recombinant antibodies (~ 27,000 Da; ~ 1.5nm) in comparison to IgG antibodies (~ 150,000 Da; ~ 30 nm) makes them desirable target specific capture agents for surface based optical sensing schemes, such as MRRs, that rely on strong light-matter interactions close to the sensing surfaces where the electromagnetic field intensities are known to be the highest. Hence, the use of 2B4 is expected to further improve the sensing performance of optical biosensors that have traditionally used larger antibody probe molecules with capture sites further away from optical sensing surfaces where the electromagnetic field intensities are weaker. Increasing red-shifts in the resonance wavelength of the MRR sensors were measured upon exposure to the biotinylated-2B4 solutions for time durations up to 1 hr. After 1 hr, the resonance shifts due to 2B4 binding were ~0.14 nm and ~0.10 nm for the suspended and supported MRRs, respectively. Exposure of the functionalized sensor surface to the biotinylated-2B4 solutions for time durations exceeding 1 hr did not produce any noticeable additional increase in resonance wavelength. These results suggest that an exposure of 1 hr was sufficient to ensure saturation of the biotinylated-2B4 binding curve for the streptavidin functionalized sensor surfaces. Following the biotinylated-2B4 binding, an additional rinse step discussed in Section 2.6 resulted in a small blue-shift in the resonance wavelength of both MRR sensors corresponding to a loss of some of the linker molecules. The transmission spectra labeled Biotin-2B4 in Figure 3.4c and d were measured after this rinse step.

To demonstrate the capabilities of suspended MRRs for specific molecular detection, suspended and supported MRRs functionalized with 2B4 were exposed to heat-denatured Herceptin molecules. Figure 3.4c and d shows the resonance wavelength shift exhibited by the sensors upon capture of Herceptin molecules. The suspended MRR sensors demonstrate a near 2-fold larger resonance wavelength shift of ~ 1 nm in comparison to the ~ 0.5 nm shift for the supported MRR sensors. Figure 3.4e summarizes the results obtained for the specific detection of heat denatured Herceptin using the suspended and supported TM-mode MRR sensors.

Avastin, a therapeutic mAb also used in the treatment of metastatic breast cancer, was used as a negative control antibody molecule. No measureable shift in MRR sensor responses were found upon exposure to Avastin control solutions for the suspended and supported structures (not shown). These results confirmed that the biotinylated-2B4 sensor surfaces provided the required selectivity for capturing heat denatured Herceptin mAbs. The specificity of denatured Herceptin attachment to biotynylated-2B4 was additionally tested by exposing both suspended and supported MRR sensor surfaces, after each step of surface functionalization (APTES, aldehyde and streptavidin), to the denatured Herceptin molecules. There were no measureable changes in resonance wavelengths for each of the tested sensors (not shown). These additional control experiments further verified that Herceptin molecules only bind to the 2B4 bioreceptor.

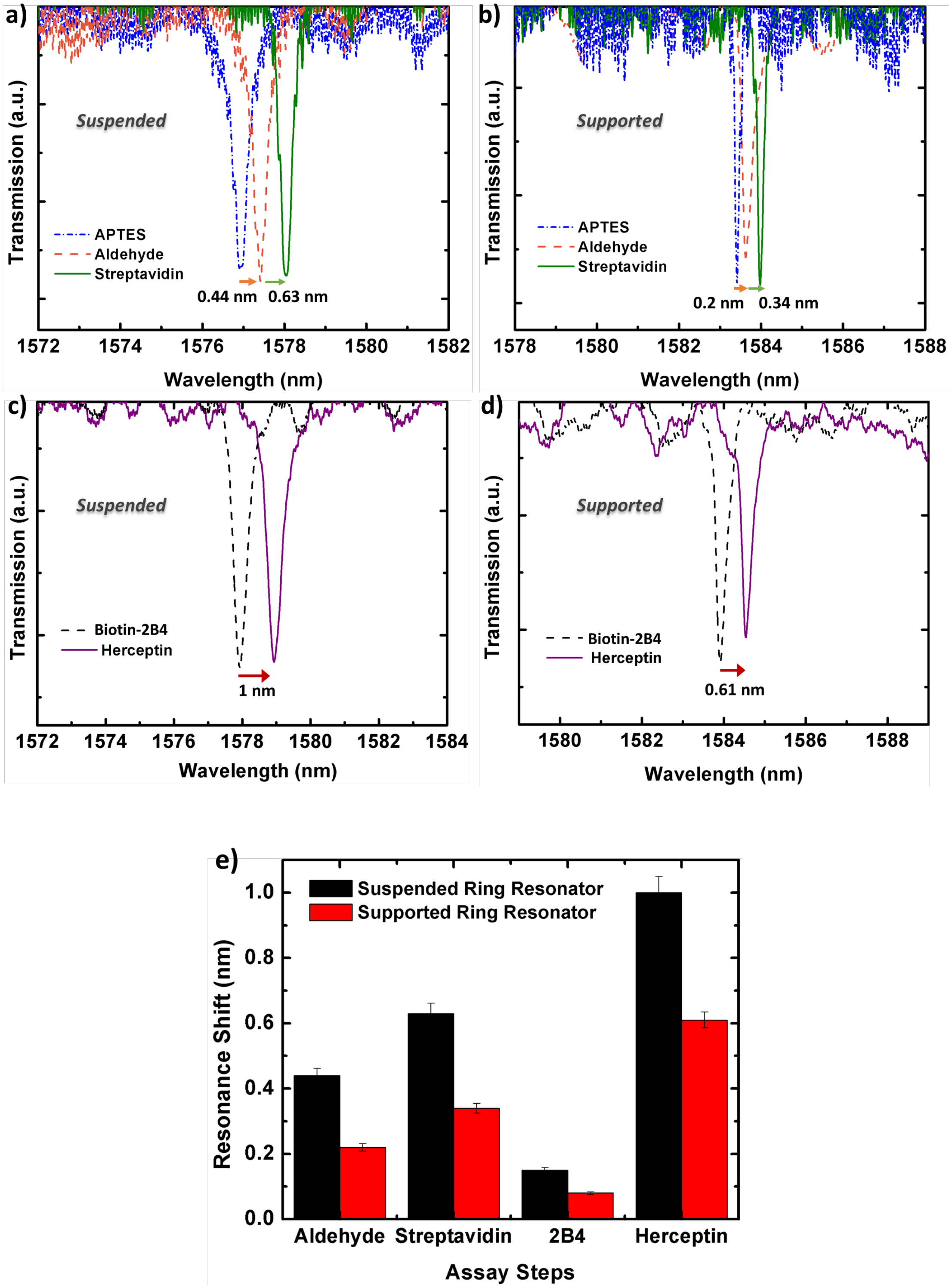

Figure 3.4 Surface-based specific detection of Herceptin mAb on suspended and supported TM micro-ring resonator sensors. Transmission spectra showing resonance wavelength shifts that result from the

molecular attachments that functionalize the surface of the (a) suspended and (b) supported micro-ring resonator sensors. Transmission spectra showing the increase in resonance wavelength upon the capture of Herceptin using biotinylated-2B4 probe molecules for the (c) suspended and (d) supported micro-ring resonator sensors. The resonance shifts due to the rinsing steps before and after the 2B4 attachment are not shown. (e) Comparative sensing results for suspended and supported micro-ring resonator sensors showing a near 2-fold improvement in the detection sensitivity of the suspended rings.

3.6 Conclusion

In this Chapter, we demonstrate ~3-fold improvement in bulk detection sensitivity and a near 2-fold improvement in detection sensitivity for Herceptin, a therapeutic monoclonal antibody, by engineering suspended MRR sensors that inherently provide a higher optical mode overlap with captured molecules compared to supported MRRs. Use of a small, single chain fragment variable recombinant antibody instead of a more traditional antibody as the selective bioreceptor for Herceptin further promotes stronger interaction between the optical mode and target Herceptin molecules by capturing the target molecules closer to the sensor surface where the electromagnetic field is stronger. Control experiments carried out using similar concentrations of Avastin, another therapeutic monoclonal antibody, showed no measureable response by the sensor, confirming the selectivity of the sensor and the stability of the silicon surface chemistry. Importantly, the suspended MRRs exhibit excellent mechanical stability throughout the assays, suggesting that they will be compatible with high-throughput sensor arrays integrated with microfluidic systems.

CHAPTER 4

DE NOVO PHOTONIC CRYSTAL DESIGN METHOD

4.1 Introduction

In his 1987 seminal paper “Inhibited Spontaneous Emission in Solid-State Physics and Electronics,” E. Yablonovitch proposed the PhC as an optical analogy of a solid state crystal [88]. Analogous to “color centers” or “defect states” in an electrical band, PhC cavities have been realized by introducing defects into the perfectly periodic dielectric lattices. Typically, for simplicity, the unit cells in PhCs are comprised of highly symmetrical shapes (*e.g.*, squares, circles).

Figure 4.1 shows the comparison between a Si crystal and Si PhC, along with their corresponding band structures [31]. Figure 4.1a and c present the crystal structure of a typical Si lattice and its electrical band diagram. In comparison, Figure 4.1b and d show a typical 2D Si PhC and its photonic band diagram. The vertical and horizontal axes in electric band diagram are energy and momentum of the electrons, while in photonic band diagram, the two axes are frequency and wave vector and each line represents a ω-k dispersion relation. For frequencies of light within the photonic bandgap, no light propagation is allowed. A Bragg mirror consisting of a one-dimensionally periodic stack of alternating dielectric materials, is typically considered the simplest form of a PhC.

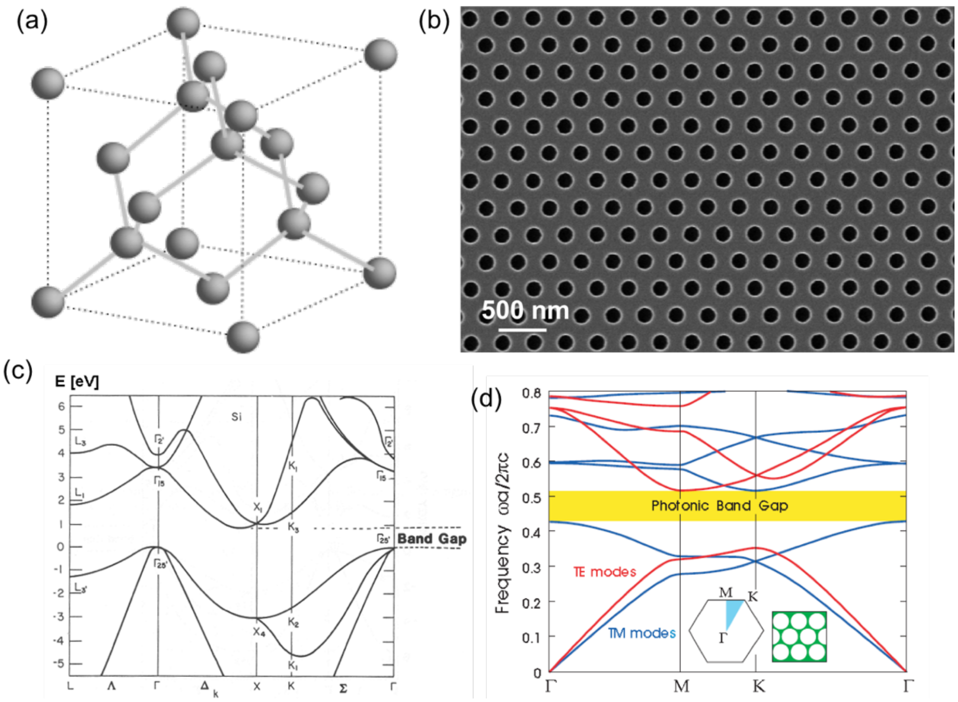

Figure 4.1 Comparison between crystal and PhC. (a) Crystal structure of Si. (b) SEM image of a PhC made on a SOI wafer. (c) Electrical band structure of Si crystal. (d) Photonic band structure of PhC shown in (b). [31] ((c) is from http://www.tf.uni-kiel.de/matwis/amat/semi_en/kap_2/backbone/r2_1_5.html)

4.2 Photonic crystal design

4.2.1 2D photonic crystal cavities

The most common design of a PhC cavity is to remove a certain number of lattice holes and form a defect state in the photonic band gap (PBG). The nomenclature for these types of cavities is based on the number of removed air holes, such as H1 to signify a single missing air hole, and L3, L5, L7, and L11 to signify 3, 5, 7 and 11 missing air holes, respectively, along light propagation direction [17, 43, 89, 90]. The drawback of this "missing hole" approach is that the mode is abruptly cut off at the edge of the cavity and the Q-factor is reduced due to the modal mismatch at the interface between the introduced cavity and surrounding lattice holes that act similar to Bragg mirrors [43]. Scattering due to the modal mismatch at this interface, along with scattering inside the mirror segments due to fabrication imperfections are the two sources of intrinsic loss in these cavities.

For the light at frequencies inside of the band gap, the optical field exponentially decays in the mirrors and can be expressed as

$$H_{mirror} = H_0 \sin(\beta_{mirror} x)\, e^{-\gamma x} \tag{4.1}$$

where β_{mirror} is the wave vector inside the mirror and γ is the decay constant. To minimize the scattering, the wave vector inside the Bragg mirror needs to be at the band edge ($\beta_{mirror} = \pi/a$) to match the periodicity of the photonic crystal design.

The field in the cavity can be expressed as

$$H_{cavity} = H_0 \sin(\beta_{cavity} x) \tag{4.2}$$

where β_{cavity} is the wave vector of the resonance mode. To avoid an abrupt mode change at the interface between the cavity and mirrors, the wave vectors must be matched: $\beta_{cavity}=\beta_{mirror}=\pi/a$. Applying the continuity condition at the interface, $H_{cavity}|_{x=interface}=H_{mirror}|_{x=interface}$

$$H_0 \sin(\beta_{mirror} x)\, e^{-\gamma x} = H_0 \sin(\beta_{cavity} x) \tag{4.3}$$

requires the decay constant γ at $x=interface$ to be 0 in order to obtain the best mode match. A common design strategy that meets this requirement is to keep $\gamma=0$ at the immediate interface, but gradually increase γ with increasing distance from the interface to maintain the desired confinement of light in the cavity. One simple solution to satisfy this condition is to linearly increase γ

$$\gamma = \sigma x \tag{4.4}$$

σ denotes linear increase rate of the decay rate. Inserting this linear relation back into the mirror field profile, we obtain:

$$H_{mirror} = H_0 \sin(\beta_{mirror} x)\, e^{-\sigma x^2} \tag{4.5}$$

One can easily recognize that such a field profile represents Gaussian decay inside the mirrors. Indeed, it has been discovered that a Gaussian mirror design can significantly increase the Q-factor of PhC cavities by reducing the scattering losses from modal mismatch. Noda *et al.* first reported in 2003 that by gently shifting the two holes adjacent to an L3 cavity, the Q-factor increased from 3,000 to 45,000, as shown in Figure 4.2 [43].

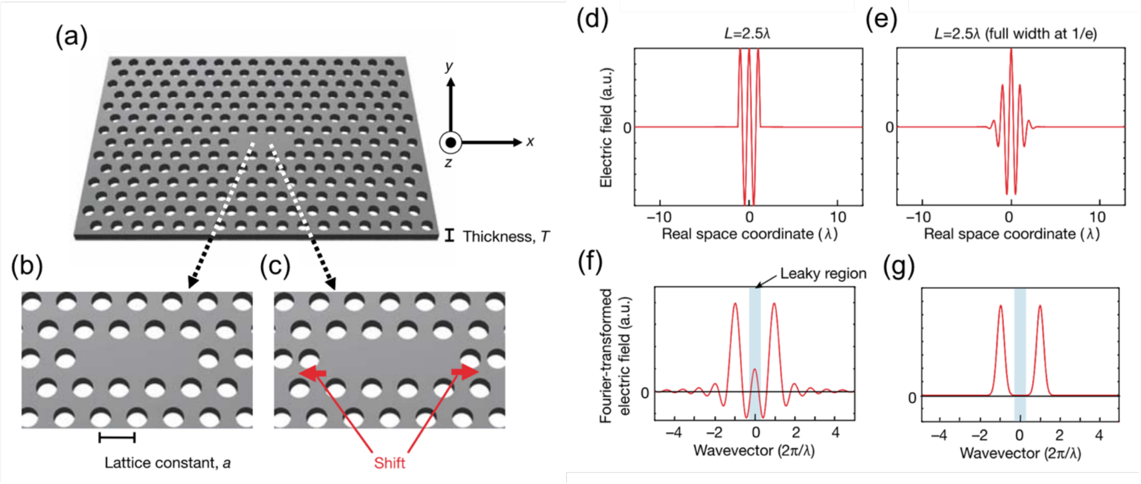

Figure 4.2 Schematics and analysis of a Gaussian mirror design in an L3 cavity that is achieved by slightly shifting two lattice holes adjacent to the cavity. (a-c) Design of L3 cavity. The two holes specified in (c) are shifted by $0.15a$ where a is the period of PhC. (d) Real space field distribution without hole shift. There is a hard cutoff at the edge of the cavity. Such an abrupt change results in spatial harmonics in the light cone, as shown in (f). (e) Real space field distribution showing that a Gaussian envelope is created by shifting the holes (e). The resulting field intensity in the leaky region is minimized, as shown in (g). Figures reproduced from Ref. [43] with permission from ©2003 NPG.

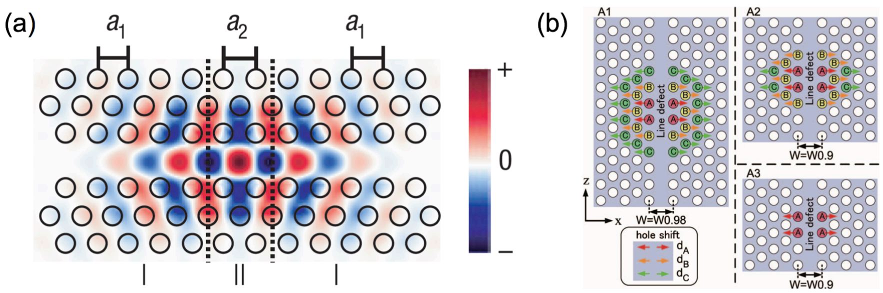

Figure 4.3 PhC waveguide based cavity designs. (a) Photonic double heterostructure. A mode gap is formed by changing the lattice constant from a_1 to a_2 [45]. (b) Local width modulated photonic cavity. A mode gap is formed by changing the waveguide width [91]. Figures reproduced with permission from ©2005 NPG and ©2006 AIP.

Slightly shifting lattice holes near a cavity provides room for the field to decay more gradually outside the cavity and, hence, the optical field is better matched at the boundary between the cavity and the mirrors. However, it requires a rigorous parameter search to find optimized hole positions for a field distribution close to a Gaussian mode profile. Further studies have investigated the design of shifting the 2nd or 3rd nearest holes and found the Q-factor is increased only by an additional factor of two [92]. Therefore, this hole position tuning method is not ideal to realize a complete Gaussian mode profile and an ultra-high Q-factor (> 10^6) PhC cavity.

To obtain a better Gaussian mode profile, a new design method based on an "open ended" waveguide mode was proposed. Figure 4.3 shows the two cavity designs from this approach: photonic double heterostructure [45] and width modulated cavity [91, 93]. The cavities are formed by slightly perturbing a PhC waveguide mode, by either changing the local lattice constant or shifting the holes to enlarge the waveguide width. Since the resonance is based on a PhC waveguide mode, it is a lossless guided mode with minimal out-of-plane radiative loss. The mode is not terminated, but slightly modified to create a local trapping defect. Furthermore, the gradual tapering from the center cavity to the PBG region produces confinement with minimum mode profile perturbation, resulting in reduced scattering and much higher Q-factor cavities (Q ~ 7×10^7) [91].

4.2.2 2D vs 1D photonic crystal resonators:

As discussed in Chapter 1, TIR only confines light at a limited range of angles (limited values of k). A complete PBG, on the other hand, confines light regardless of the k vector range. Based on Fourier transform, squeezing light in real space causes delocalization of k vectors. The delocalized k vectors may exceed the confinement range by TIR and causes the leakage of optical energy. Therefore, it is generally believed that 2D PhC resonators should have higher Q-factors than 1D resonators, because it has one more dimension of PBG than 1D PhC. However, in practice, the difference is very subtle. In 1D PhC, the majority of k vectors are along the propagation direction (k_x). TIR should be sufficient for the confinement in y and z direction in such high directional propagation mode. Therefore, the additional PBG confinement along y direction in 2D PhC only provides very limited improvement as very little light has k_y component outside of TIR confinement range.

Figure 4.4a and b shows the results from a study of impact of in-plane PBG confinement in the direction orthogonal to light propagation on the Q-factor of a PhC cavity [94]. The results indicate that three periods of lattice holes are sufficient to achieve a Q-factor as high as 5×10^5 (Figure 4.4b). Combining the analysis above and the experimental results, PBG confinement orthogonal to the light propagation direction doesn't have a large impact on the Q-factor if the mode is the highly directional propagation mode. TIR is sufficient to hold high Q-factor 1D PhC cavities. In the 1D PhC design as proposed in Figure 4.4c and d, the position of red, green and blue dielectric bars are shifted by 9, 6, and 3 nm respectively [21]. This modulation of lattice hole size creates cavity modes in the PBG, which follows the same basic mechanism of the light confinement as line-defect mode-gap cavity shown in (a) and Figure 4.3.

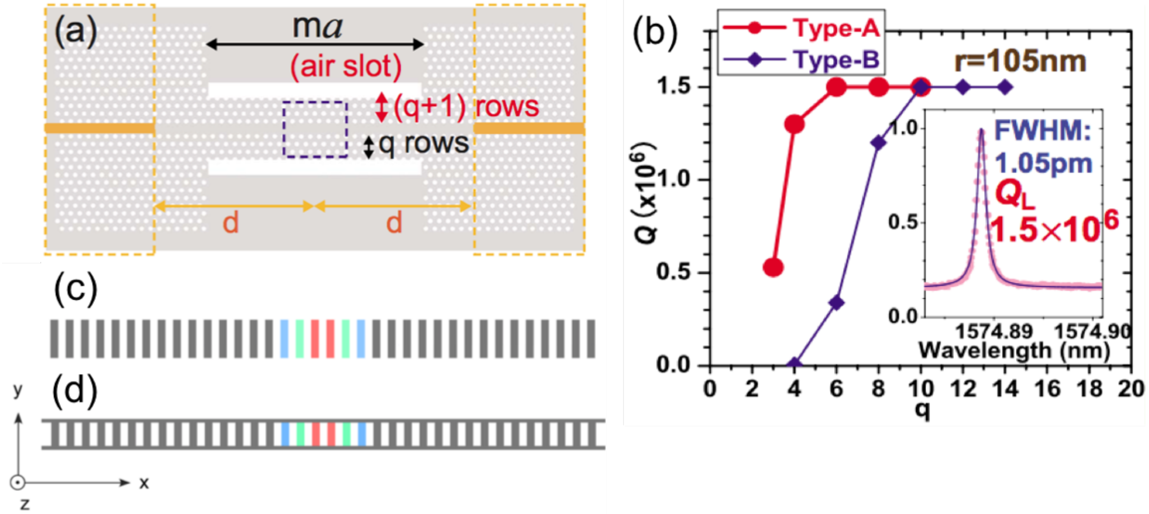

Figure 4.4 Investigation of the necessity of a PBG barrier in the *y* direction. (a) High Q 2D PhC cavity designed with various periods of lattice holes forming PBG barriers. (b) Q-factor versus PBG barrier thickness [94]. (c) and (d): Proposed 1D PhC cavity designs without PBG in y-direction [21]. Figures reproduced with permission from ©2008 AIP and ©2008 OSA.

4.2.3 1D Photonic Crystal Cavities

From the analysis in Section 4.2.1, the best resonance mode for a 1D PhC should be based on a lossless wave-guiding mode. However, unlike the 2D PhC for which the PhC waveguide is formed by a missing row of lattice holes, the guiding modes of 1D PhC are the slow light modes at the photonic band edge. To minimize the intrinsic scattering losses from modal mismatch, both the cavity length and tapering strategy of the unit cell dimensions between the cavity and mirror segments must be prudently designed.

The magnitude of the out-of-plane radiative loss with respect to the cavity length is shown in Figure 4.5 [19]. The η in the plot relates to the calculated fraction of energy associated with spatial harmonics in the light cone. The energy in the light cone is an indicator of the out-of-plane radiative loss. As shown in the figure, η in a Gaussian tapering cavity is roughly two orders of magnitude smaller than exponential decay in a traditional Bragg mirror. The optimal cavity length for a Gaussian mirror is L=0 such that the 1D PhC resonator consists of a finite number of mirror segments and taper segments, and no extended cavity segments. Therefore, a promising design strategy is to maintain the same lattice constant throughout the structure, but modulate the decay constant, or mirror strength, to form a Gaussian mirror on both sides of the L=0 cavity for confinement. It is worth noting that L3 in Ref [43] is the 2nd best cavity length indicated Figure 4.5.

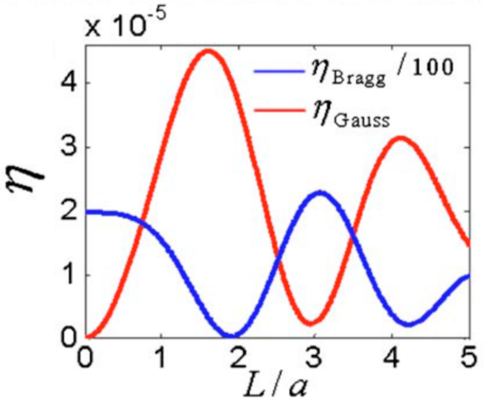

Figure 4.5 Fraction of Fourier components that are within the light cone for different cavity lengths. *L* is the length of the cavity, and *a* is the lattice constant [19]. Figures reproduced with permission from ©2010 AIP

Following optimization of the cavity length, a tapering strategy needs to be determined to form the Gaussian mirrors. As discussed in Section 4.2.1 and shown in Equation 4.4, the key is to construct a linearly increasing decay rate inside the mirror. Inside the PBG, the wavevector k for a given frequency is a complex number. The imaginary part of k denotes the decay rate γ. The real part of the wavevector inside the cavity must be π/a to match the wavevector of the Bragg mirrors. Therefore, a complex k vector can be written as:

$$k = \frac{\pi}{a} + \frac{i\gamma\pi}{a} \tag{4.7}$$

The frequency for a high Q cavity can be written as

$$\omega = \frac{(1-\delta)\sqrt{\kappa_0}\pi c}{a} \tag{4.8}$$

where κ_0 is the 0^{th} order Fourier component of the dielectric profile given by:

$$\kappa_0 = \frac{f}{\varepsilon_{air}} + \frac{1-f}{\varepsilon_{si}} \tag{4.9}$$

where f is the filling factor of the air hole [95]. Inserting Equation 4.7 and Equation 4.8 into the Master equation (Equation 1.18), we find:

$$\gamma = \sqrt{\frac{(\omega_2-\omega_1)^2}{(\omega_2+\omega_1)^2} - \frac{(\omega_{res}-\omega_0)^2}{{\omega_0}^2}} \tag{4.10}$$

where ω_1 and ω_2 are the dielectric band edge and air band edge frequencies, ω_0 is the midgap frequency given by $\omega_0 = (\omega_1 + \omega_2)/2$, and ω_{res} is the targeted cavity resonance frequency [19].

As discussed in Section 4.2.1, a Gaussian mirror is just one way of matching the continuity conditions at the interface between the mirrors and the cavity. As long as both the group velocity and decay rate match at the interface, out-of-plane radiative losses will be minimized. Therefore, many tapering profiles of decay rate (*i.e.*, mirror strength) could achieve high Q-factor resonances.

However, one should pick a tapering design within practical fabrication tolerances. For example, even using the state-of-art electron beam lithography techniques, the radii differences below 5 nm may not be resolved and will very likely turn out to be the same size in the final structure.

4.2.4 Exploration of 1D PhC design space

Traditional designs utilize circles and squares as PhC unit cells. In such highly symmetrical shapes, the only degree of freedom is the filling factor. Therefore, a 1D PhC cavity, commonly referred to as a nanobeam cavity, is formed by gradually changing the overall size of the air holes over the length of the nanobeam. Recalling the well-developed analogy between solid state physics and PhCs, it is not surprising that a defect can be created by changing the air hole size as it is similar to the idea of a dopant or substitutional atom in a crystal lattice. In the following section of this Chapter, we explore a broader parameter space of PhC unit cells with the goal of extending the functionality of PhC nanobeam cavities.

In order to build our intuition on the photonic band gap, we first analyze the guiding mode in a normal waveguide. Shown in Figure 4.6a and b is a guided mode (mode I and II, respectively) with spatial phase difference of π. Due to the translational invariance, modes I and II are degenerated and corresponding to the same mode in the band diagram. To break the translational invariance, an array of air holes is superimposed on the wave guiding mode I and II in Figure 4.6d and e. In mode I, the maximum of the optical field intensity spatially overlaps with the air holes, while in mode II, the minimum field intensity overlaps with the air holes. As discussed in the perturbation theory section in Chapter 1, these two modal overlaps cause different energy perturbations of the total optical field, and result in a mode split in the photonic band diagram. The opening of this mode split is essentially the photonic band gap in a 1D nanobeam, in which light is not allowed to propagate, as shown in Figure 4.6f. The upper band (Mode I) corresponds to the “air mode”, since the majority of the field is in the air holes, while the lower band (mode II) corresponds to the “dielectric mode”. The magnitude of the mode splitting scales with the size of the air holes. As shown in Figure 4.6g, the PBG opening increases with larger air holes.

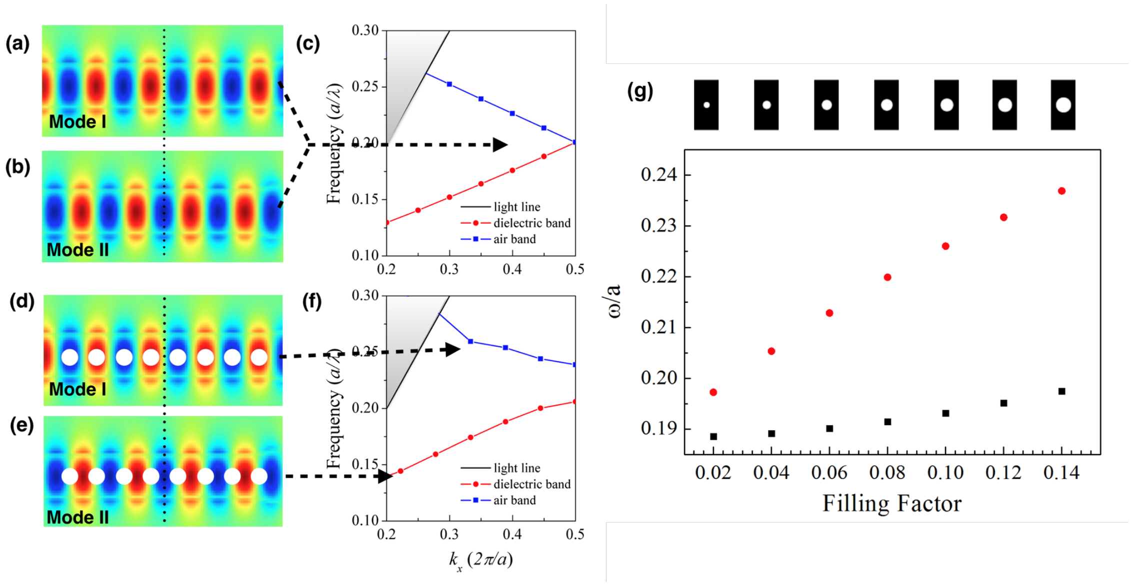

Figure 4.6 In a 1D PhC, degeneration of the guided mode forms the PBG. (a) and (b) are the waveguide mode (mode I and II) with spatial phase difference of π. (c) Band diagram for mode I and II in (a) and (b). (d) and (e) are the PhC with an air holes superimposed on the wave guided mode I and II. (f) Band diagram for mode I and II in (d) and (e). (g) The frequency range of the PBG scales with the size of air holes.

The study above suggests that any geometrical shapes with the correct periodicity can open a photonic band gap and form a cavity through proper design. As an example, Figure 4.7a and b shows a 1D PhC nanobeam design based on a “cat paw” shaped unit cell. Similar to the traditional method of changing the size of a circular air hole, the photonic band structure is expected to change with deliberate variations in the size of the “cat paw” [95]. By simulating the resulting band structures for each variation in the "cat paw" size, we can engineer a PhC cavity with the smallest "cat paw" at the two ends and the biggest "cat paw" forming the center of the cavity. In this way, light at the resonance wavelength will be trapped within the cavity. Tapering of the "cat paw" size from the cavity center to the nanobeam edges follows the deterministic design method in Ref. [95] and ensures the linear change of mirror strength. Such tapering profile avoids an abrupt cut-off in cavity field intensities and minimizes scattering losses. As shown in Figure 4.7 (b), the resonance mode is well confined within the nanobeam center and the simulated Q-factor is ~ 10^5.

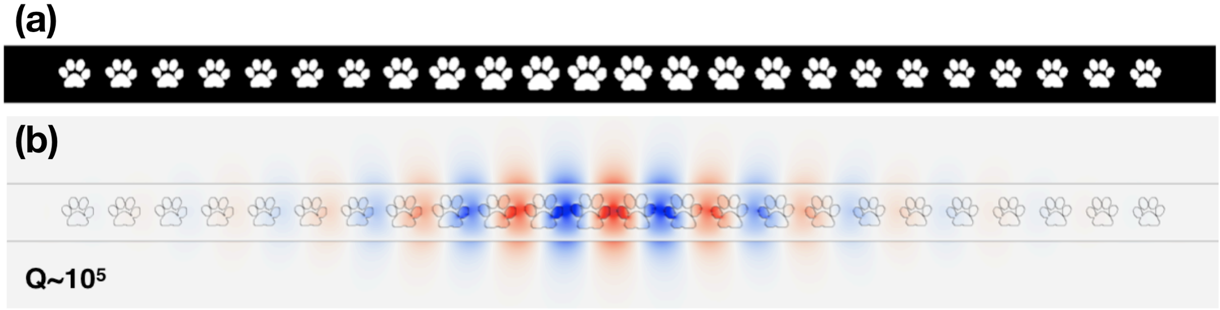

Figure 4.7 "Cat paw" PhC cavity design. (a) and (b) dielectric and resonance mode profile of 1D PhC nanobeam design by cat paw shaped unit cell.

4.3 Expanding the design space: engineering degrees of freedom of the unit cells

As proved by the cat paw PhC cavity, high Q PhC can be designed using arbitrary geometrical shapes. We propose a new perspective in PhC design: engineering the shape of the unit cell to introduce more degrees of freedom, allowing for additional light-matter interactions not achievable in traditional PhCs. We name this design perspective *de novo* PhC design in order to differentiate with the traditional design approach that suggests only to change the filling factors and positions of highly symmetric unit cells. Our *de novo* PhC design method exploits new unit cell design features to predictably tune the PhC band structure while keeping the lattice constant unchanged. The advantages to this approach are two-fold. First, we are able to introduce new degrees of freedom by choosing different unit cell geometries. These additional degrees of freedom give new ways of controlling the band structure. Second, we are able to add subwavelength elements into the unit cell. These elements can be used to predictably perturb the optical mode to achieve the desired mode distribution.

4.3.1 Controlling the optical field distribution by breaking the rotational symmetry

While the "cat paw" PhC illustrates an extreme example of unit cell design freedom, Figure 4.8 shows a more practical example of using the *de novo* design methodology. To demonstrate how modifying a PhC unit cell can modify the band structure and mode profile, we consider a building block unit cell of a one-dimensional (1D) PhC waveguide consisting of a circular air hole with a narrow dielectric beam spanning its diameter, as depicted in Figure 4.8. Light propagates along the waveguide in the direction labeled k_x. The addition of the dielectric beam in the unit cell breaks the rotational symmetry. The rotation angle here is defined as the angle between the long axis of the beam and direction of light propagation. Therefore, when the beam is parallel to the light propagation direction, the rotation angle is 0^o or R0 (Figure 4.8a) and when the beam is perpendicular to the light propagation direction, the rotation angle is 90^o or R90 (Figure 4.8b). As a result of breaking the rotational symmetry of the unit cell, the optical mode changes according to the rotational angle, as shown in Figure 4.8c. The higher frequency air band that gives maximum mode confinement within the air holes reduces in frequency as the beam is rotated from 0^o to 90^o. The lower frequency dielectric band remains largely unchanged as a function of the beam rotation angle because the mode is primarily confined in the dielectric regions between the PhC lattice holes. Therefore, the mode sees very little interaction with the dielectric beam within the air holes. The electric field energy density profile at the air band edge for both R0 and R90 unit cells (Figure 4.8d) provides insight on why the rotation angle of the unit cell controls the position of the air band. For the R0 unit cell, the energy is almost uniformly distributed throughout the air hole with almost no energy localized within the dielectric beam. In contrast, for the R90 unit cell, the majority of the field is localized within the narrow dielectric beam, increasing the effective permittivity of the air hole and therefore decreasing the air band edge frequency. The position of the air band can be nearly continuously tuned between the R0 position and R90 position by changing the rotation angle between 0° and 90°.

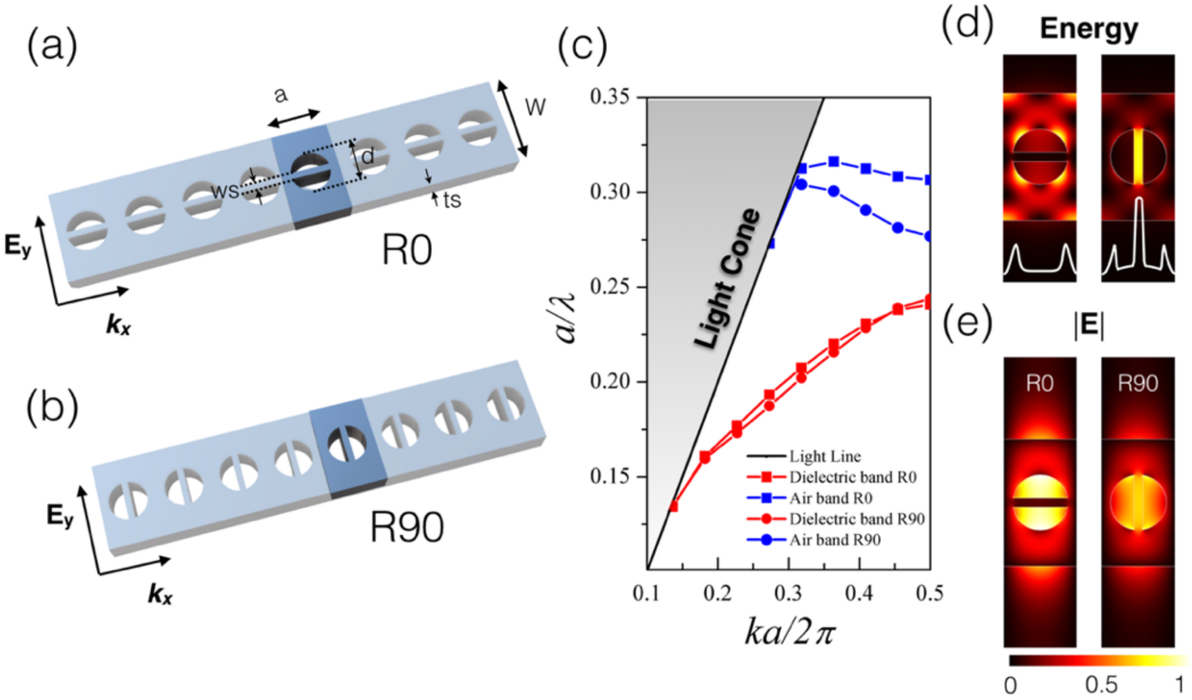

Figure 4.8 Mode change due to breaking the rotational symmetry of the photonic crystal unit cell. The unit cell consists of a circular air hole in a dielectric material with a thin dielectric beam spanning the diameter of the air hole. (a) Dielectric beam parallel to the direction of light propagation (R0). (b) Dielectric beam perpendicular to the direction of light propagation (R90). (c) Band diagram for 1D silicon photonic crystal waveguides with R0 or R90 unit cells displaying mode change due to the breaking of rotational symmetry within the unit cell. The width of the Si beam (w_s), diameter of the circular holes (*d*), width of the waveguide (*w*), and photonic crystal lattice spacing (*a*) are 50 nm, 300 nm, 700 nm, and 400 nm, respectively. (d) Electric field energy distribution for R0 and R90 unit cells at band edge. The white traces show the 1D (horizontal) energy profile at the middle of the respective unit cell. (e) Electric field distribution for R0 and R90 unit cells at band edge (*k*=0.5). Reprinted with permission from Ref. [96]. Copyright 2016 American Chemical Society.

4.3.2 Exploring electromagnetic boundary conditions: anti-slot effect

We term the phenomenon of squeezing light into nanoscale regions of high permittivity dielectric materials (Figure 4.8d) as the *anti-slot effect* because it is opposite to the well-known slot effect. Understanding the complimentary nature of the slot and anti-slot effects can lead to new approaches for manipulating the mode profile and energy distribution of light in photonic structures. Here, we provide a more comprehensive explanation of the newly coined anti-slot effect and its relationship to the slot effect.

As shown in Equation 4.11, the electromagnetic boundary conditions dictate that the tangential component of the electric field, $\boldsymbol{E}_t$, is continuous across an interface between two materials. In this equation, $\boldsymbol{E}_{t,,high}$ and $\boldsymbol{E}_{t,,low}$ are the intensities of the tangential components of the electric field in the media of higher and lower permittivity, respectively, on opposite sides of the interface. Accordingly, the corresponding tangential component of the electric displacement field, $\boldsymbol{D}_t = \varepsilon \boldsymbol{E}_t$, is discontinuous across the interface as shown in Equation 4.12.

$$E_{t,high} = E_{t,low} \tag{4.11}$$

$$D_{t,high} = D_{anti-slot} = \frac{\epsilon_{high}}{\epsilon_{low}} D_{t,low} \tag{4.12}$$

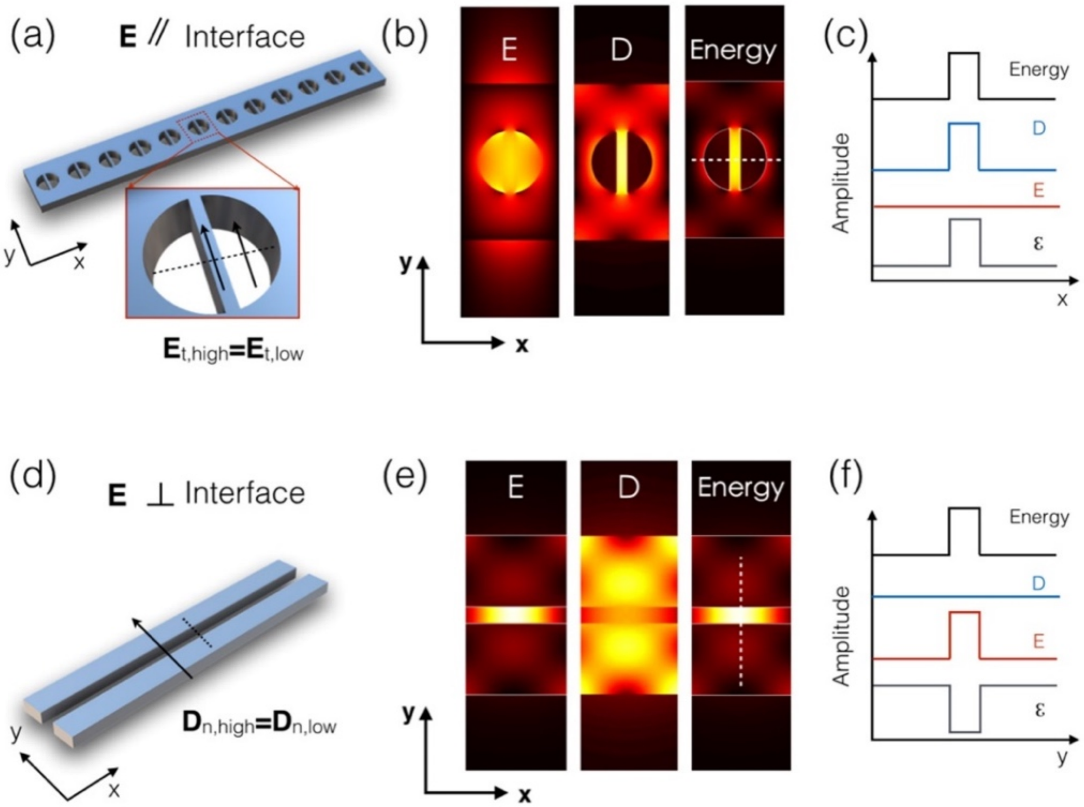

Figure 4.9 Explanation of anti-slot effect and comparison to slot effect. (a) Schematic of a photonic crystal waveguide formed with a R90 unit cell – termed an anti-slot waveguide. (b) Simulated profiles of ***E***, ***D***, and electric field energy density of a silicon anti-slot waveguide assuming the same dimensions as given in Figure 4.8. (c) Schematic line profiles of the dielectric constant (ε), electric field amplitude (***E***), electric displacement field amplitude (***D***), and electric field energy density across the anti-slot along *x*-axis as indicated by the dashed line in (a). (d) Schematic of a slot waveguide. (e) Simulated profiles of ***E***, ***D***, and electric field energy density of a silicon slot waveguide assuming the widths of the waveguide and slot are 500 nm and 50 nm, respectively. (f) Schematic line profiles of ε, ***E***, ***D***, and electric field energy density across the slot waveguide along the y-axis as indicated by the dashed line in (d). Reprinted with permission from Ref. [96]. Copyright 2016 American Chemical Society.

Considering a 1D PhC with a R90 unit cell and light polarized in-plane (TE-polarization), as illustrated in Figure 4.9a, the electric displacement field in the high permittivity dielectric beams is enhanced by a factor of $\varepsilon_{high}/\varepsilon_{low}$ compared to the surrounding lower permittivity air regions inside the lattice holes (Equation 4.12), while the electric field intensity in the beams is the same as that of the surrounding regions inside the air hole (Equation 4.11). Importantly, the electric field energy density, $u_E = \frac{1}{2}\boldsymbol{DE}$, inside the dielectric beams is also enhanced by a factor of $\varepsilon_{high}/\varepsilon_{low}$ due to the enhancement of the electric displacement field, as shown in Figure 4.9b and c.

The traditional slot effect, on the other hand, squeezes light into nanoscale low permittivity regions surrounded by higher permittivity media, which is the opposite of the anti-slot effect. To explain the slot effect, electromagnetic boundary conditions for the normal components of the electromagnetic field are considered. As given in Equation 4.13, considering that there is no surface charge, the normal component of the electric displacement field is continuous across the interface between two different materials, where $\boldsymbol{D}_{n,,low}$ and $\boldsymbol{D}_{n,,high}$ are the intensities of the normal components of the electric displacement field in the media of lower and higher permittivity, respectively, on opposite sides of the interface. The corresponding normal component of the electric field, $\boldsymbol{E}_n$, is therefore discontinuous across the interface, as shown in Equation 4.14.

$$D_{n,low} = D_{n,high} \tag{4.13}$$

$$E_{n,low} = E_{slot} = \frac{\epsilon_{high}}{\epsilon_{low}} E_{n,high} \tag{4.14}$$

As a result of these boundary conditions, and as illustrated in Figure 4.9d-f, when a material of lower permittivity is squeezed into a nanoscale slot between two higher permittivity regions, the electric displacement field (TE-polarization) in this slot has the same intensity as that in the surrounding higher permittivity regions (Equation 4.13), while the electric field intensity is enhanced by a factor of $\varepsilon_{high}/\varepsilon_{low}$ (Equation 4.14). The electric field energy density inside the low permittivity slot is therefore also enhanced by a factor of $\varepsilon_{high}/\varepsilon_{low}$ due to the enhancement of the electric field. We note that the slot effect leads to the lower electric field intensity and lower energy density in the dielectric beam in the R0 unit cell compared to the surrounding air regions inside the lattice hole for TE-polarized light, as well as the slight energy density enhancements that arise at edges of the lattice holes for both the R0 and R90 unit cells (Figure 4.8d,e) [97].

Unlike the slot effect that is supported using a traditional waveguide geometry, the anti-slot effect displayed in the R90 unit cell can only be supported when incorporated as part of a PhC or engineered material that supports light propagation based on the designed periodicity of the arrayed unit cells. For the anti-slot effect, light is confined in a thin dielectric beam that is positioned with its long axis perpendicular to the propagation direction of light to satisfy the electromagnetic boundary condition shown in Equation 4.12. Hence, an anti-slot waveguide cannot be formed in the same way as a slot waveguide. For a guided mode to interact with an anti-slot, the light confinement must be provided by incorporating the anti-slot into another structure that can support the necessary waveguide confinement. For example, when a 1D PhC is used to provide confinement for a guided mode, the peaks of the electric field are localized within the lattice holes for the air band edge mode ($k=\pi/a$). The anti-slot effect can then be supported in the 1D PhC when thin dielectric beams are placed at the peak locations of the electric field inside the PhC lattice air holes where the strongest electromagnetic energy can be squeezed into the dielectric beam.

4.3.3 Design of a single PhC with both air mode and dielectric mode resonances

Figure 4.10 shows the change of band edge frequencies with respect to the rotational angle of an added antislot beam. A key observation is that the air mode and dielectric mode band edges shift in opposite directions as the antislot rotates from 0^o to 90^o. As discussed in the previous section, the reduced air band edge frequency with increasing rotation angle is due to the antislot effect. The increase of the dielectric band edge frequency with rotation angle is due to the fact that the R0 unit cell supports a larger effective index in the dielectric mode compared to the R90 unit cell. In the R0 configuration, the tail of the optical field can expand into the antislot bar that is directly connected to the dielectric region between air holes where light supported in the dielectric mode is primarily localized; in the R90 configuration, the evanescent field only interacts with air in the air hole. Hence, by rotating the antislot bar from parallel to perpendicular to the light propagation direction, both air and dielectric modes of the R90 unit cell are shifted into the band gap of the R0 unit cell. This implies that we are able to design a novel cavity with dual-resonances.

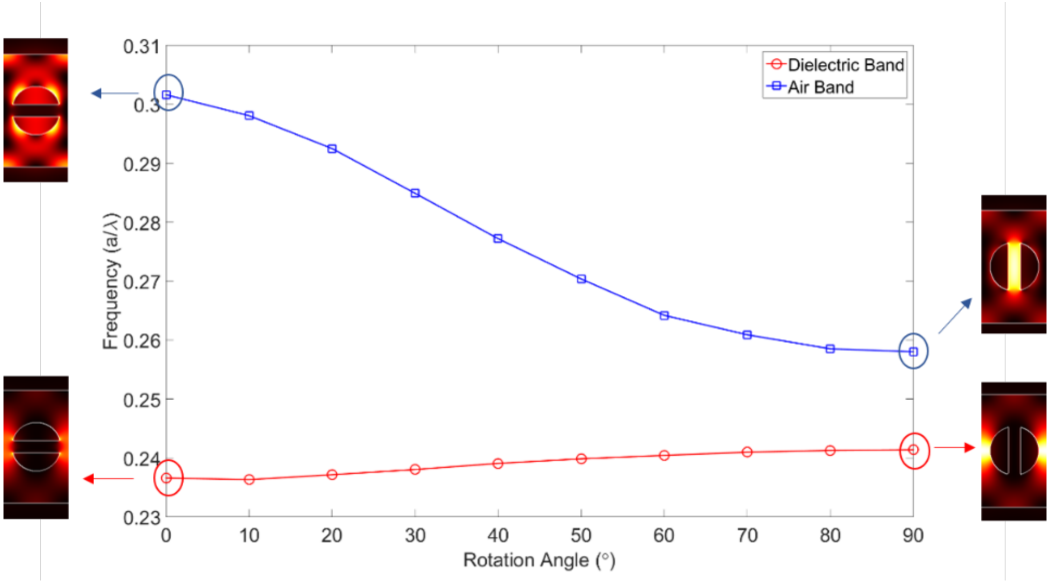

Figure 4.10 Change of photonic band edge versus rotational angle of an 80 nm wide anti-slot. Band edge modes of R0 and R90 unit cells are shown as inserts. Blue curve is air mode and red one is dielectric mode.

The capability of simultaneously confining multiple resonances in a spatially overlapped region is important to many applications. For example, to enhance the emission of fluorophores or quantum dots, a shorter wavelength resonance can be used to enhance the excitation light and a longer wavelength resonance can be tuned to enhance the emission light. If tuned appropriately, multiple resonances could also be used for enhancement of multiple orders of harmonic generations. Other nonlinear processes, such as combs and multi-wave mixing, could also be benefit from the spatially overlapped multiple resonances.

Until now, almost all PhC cavities have been primarily designed for single resonance operation [19, 98, 99]. This is mainly because traditional PhCs uses highly symmetric unit cells (*i.e.*, circles, squares) and are limited in their design parameters space. For these structures, both the air and dielectric bands shift in the same direction as the filling factor changes. Consequently, while the dielectric band edge frequency can be pushed up into the band gap by increasing the filling factor, the frequency of the air band edge would also moves up and hence not fall within the band gap. Therefore, for traditional high Q-factor PhCs, both the dielectric and air bands cannot be simultaneously confined. We note that it is possible to design a cavity that supports more than one mode in the same cavity by using different polarizations [100], but such cavities require additional polarization control elements to convert light between TE and TM states and it is difficult to independently control the frequencies of each mode. A crossbeam PhC nanocavity was also proposed to achieve dual resonances based on two crossing waveguides [101]. The pitches and filling factors are tuned independently for each waveguide to have different wavelength resonances at center. One drawback of this design is that the Q-factor is comparatively low (~ 1000).

As a first step towards experimentally realizing a 1D PhC with both air mode and dielectric mode resonances, we fabricated an R90 PhC nanobeam to verify the expected air band edge and dielectric band edge wavelengths. One practical challenge of simultaneously measuring air and dielectric modes in a PhC cavity is that the PBG is usually a few hundred nanometers, which is much wider than typical measurement spectrum range (1500 – 1630 nm). Hence, it would be easy to miss one of the modes simply because it fell outside the measurements window due, perhaps, to minor fabrication variations from the designed feature sizes. By initially measuring an R90 waveguide, the possibility to couple into multiple modes outside PGB makes the measurement more straightforward and facilitates selection of the appropriate dimensions to enable both resonances to fall within the measurement window (*i.e.*, both band edges of the R90 waveguide must fall within the measurement window). To fit within our 130 nm wide measurement window, we choose the anti-slot width to be 80 nm. Such a wide anti-slot decreases the air mode frequency of the R90 below the center of the R0 band gap and thus puts it close to the dielectric band edge, as shown in Figure 4.10.

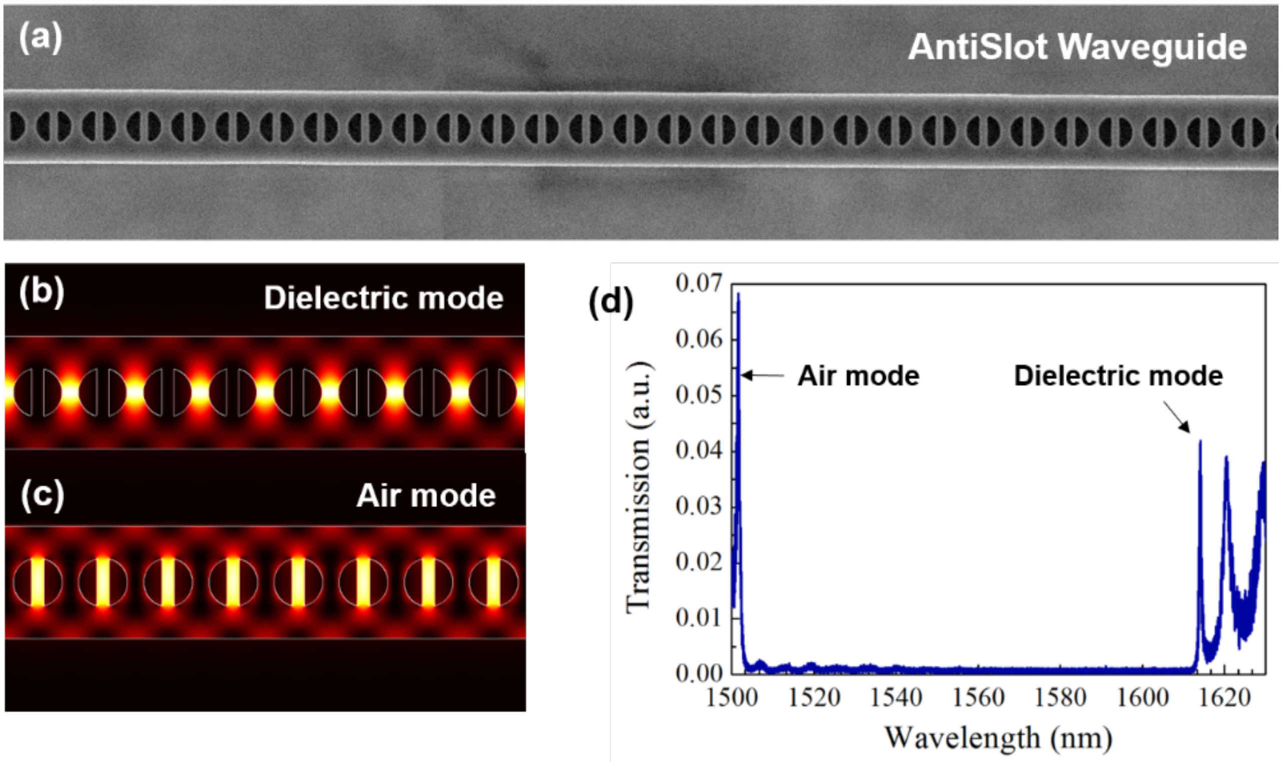

Figure 4.11 Experimental measurement of an anti-slot PhC waveguide. (a) SEM image of fabricated anti-slot PhC waveguide. Simulated (b) dielectric and (c) air band edge modes of the anti-slot PhC waveguide. (d) Measured transmission of the waveguide in (a). Both the air mode (~ 1505 nm) and dielectric mode (~1615 nm) band edge appear within the measurement window.

Figure 4.11a shows a SEM image of the fabricated anti-slot waveguide with period *a*=400 nm, radius *r*=150 nm and nanobeam width *w*=700 nm. The simulated optical field distribution of the dielectric and air band edge modes is shown in Figure 4.11b and c, respectively. The measured transmission (Figure 4.11d) shows both the air (~ 1505 nm) and dielectric band edge (~ 1615 nm). This measured band gap is in good agreement with the simulation (130 nm).

After tuning both band edge modes into our measurement window, we design a cavity by rotating the anti-slot as per the band calculation shown in Figure 4.10. From the discussion above, the R0 unit cell acts as a mirror and is capable of confining both air and dielectric modes of the R90 unit cell. To keep it simple, we chose a linear decrease of rotational angle, 10^{o} per unit cell. Figure 4.12 shows a SEM image of the PhC nanobeam and its measured transmission spectrum. The Q-factor is about 40,000 for the air mode and 8,000 for the dielectric mode. This difference in Q-factor is because of the different mirror confinement for each mode. As shown in Figure 4.10, the air mode of R90 is deep into the band gap, while dielectric mode is still very close to the R0's band edge. Therefore, a mirror formed by R0 unit cells has much higher confinement strength for the air mode compared to the dielectric mode.

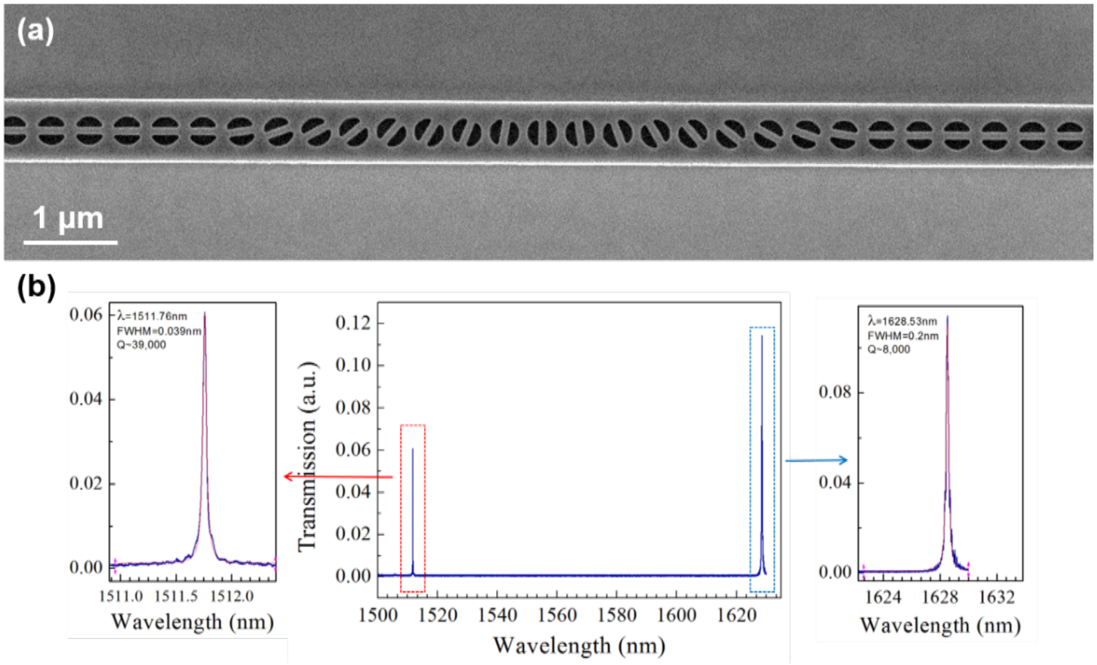

Figure 4.12 Dual resonances anti-slot PhC cavity. (a) SEM image of the rotational tapering between the R0 and R90 unit cells. (b) Experimental transmission spectrum shows both air mode and dielectric mode resonances.

4.4 Conclusion

In this chapter, we reviewed the traditional PhC design strategy and proposed a *de novo* design method. This new method exploits non-traditional unit cell design features to predictably tune the PhC photonic bands. With this new perspective, we are able to introduce new degrees of freedom by choosing different unit cell geometries, permitting previously untapped control of nanoscale light matter interactions. The *de novo* design method provides better control of the band structure by expanding the design space. As an example, by simply unlocking the rotational degree of freedom, we discovered the anti-slot effect, which confines light in the subwavelength high index region in the nanophotonic structure. Such an anti-slot effect is complimentary to the well-known slot effect and could make an impact in applications which require strong light-matter interaction within a high index material. We also showed that with the additional degree of freedom, we are able to design a dual-resonance PhC cavity that simultaneously supports both air mode and dielectric mode resonances. Such a dual-resonance cavity could also be used in photon-emission enhancement, high harmonic generation, and multi-wave mixing.

CHAPTER 5

BOWTIE PHOTONIC CRYSTAL WITH DEEP SUBWAVELENGTH CONFINEMENT

5.1 Introduction

Plasmonic and metal-based metamaterial structures capable of strong light-matter interaction based on concentrating light into deep-subwavelength volumes (*e.g.*, $V_m \sim 10^{-3}\ (\lambda/n)^3$) were long thought to be the most promising avenue for interfacing nanophotonic structures with electronics and advancing technologies related to generating, guiding, modulating, and detecting light [6]. However, ohmic losses (*i.e.*, leading to a $Q \sim 10 - 100$) have precluded the realization of practical devices to date [28, 30] despite attempts to mitigate losses through the use of hybrid plasmonic elements [102], the incorporation of gain [103], and the fabrication of alternative plasmonic materials [30] or all-dielectric metamaterials [104] and metasurfaces [105]. Low-loss (*i.e.*, supporting $Q \sim 10^5 - 10^6$), all-dielectric cavities, on the other hand, have been the basis for practical devices, despite their largely diffraction-limited mode volume (typically $V_m \sim (\lambda/2n)^3$, with slotted cavities approaching $V_m \sim 0.01\ (\lambda/n)^3$) [20, 31, 106].

In this chapter, we continue exploiting the *de novo* photonic crystal design method and report the design, simulation, fabrication and testing of an all-dielectric PhC cavity that can overcome both the loss limitations of plasmonic elements and the modal volume limitations of traditional dielectric cavities.

5.2 Design of bowtie photonic crystal unit cell

As introduced in Chapter 4, the anti-slot effect concentrates the optical field in the nanoscale region of high index material, while the slot effect pushes light into the nanoscale regions of low index material. Due to the orthogonal nature of electromagnetic boundary conditions that give rise to the slot and anti-slot effects, light can be progressively squeezed in both the propagation direction (*i.e.*, *x*-direction) and the perpendicular in-plane direction (*i.e.*, *y*-direction) by introducing a series of interlocked anti-slots and slots, respectively.

Figure 5.1 shows unit cells containing an increasing number of interlocked anti-slots and slots. Detailed dimensions of these simulated unit cells can be found in Figure 5.2. The nomenclature for these interlocked anti-slot – slot designs follows the number of anti-slots and slots introduced within the unit cell. . Accordingly, the 0th order structure does not contain any anti-slots (A) or slots (S), the 1st order structure contains a single anti-slot, and subsequent orders are given by AS (2nd order), ASA (3rd order), ASAS (4th order), etc., as labeled in Figure 5.1. Light is localized within the last anti-slot or slot introduced and therefore the optical energy is progressively squeezed into smaller and smaller mode volumes. The energy density cross sections shown in Figure 5.1b and Figure 5.1c indicate that the mode profile along the *y*-direction is squeezed only when a slot is introduced while the mode profile along the *x*-direction is squeezed only when an anti-slot is added. Figure 5.3 shows these line traces on a log scale to more clearly show the energy density enhancements of the interlocked and bowtie unit cells compared to the 0th order structure and the fact that the reported energy density of the bowtie structure is a lower bound due to mesh-size limitations in the simulation. Magnetic field distributions, which complement the electric field distributions in the anti-slot and higher order interlocked unit cells, are shown in Figure 5.4. The figure clearly shows how the magnetic field distribution is affected by adding an anti-slot to a conventional photonic crystal unit cell that is characterized by a circular air hole surrounded by dielectric material. In the conventional unit cell, the electric field is almost uniform within the air hole (see Figure 5.1) and the magnetic field is strongest in the dielectric surrounding the air hole. In contrast, when the dielectric anti-slot is added to the unit cell, the magnetic field distribution is modified in accordance with Maxwell's equations such that the electric field remains largest along the nodal planes of the magnetic field. Therefore, as expected, we find that the magnetic field distributions shown in Figure 5.4 complement the electric field localizations shown give rise to the slot and anti-slot effects, light can be progressively squeezed in both the propagation direction (*i.e., x*-direction) and the perpendicular in-plane direction (*i.e., y*-direction) by introducing a series of interlocked anti-slots and slots, respectively. Figure 5.1 shows unit cells containing an increasing number of interlocked anti-slots and slots. Detailed dimensions of these simulated unit cells can be found in Figure 5.2. The nomenclature for these interlocked anti-slot – slot designs follows the number of anti-slots and slots introduced within the unit cell. Accordingly, the 0th order structure does not contain any anti-slots (A) or slots (S), the 1st order structure contains a single anti-slot, and subsequent orders are given by AS (2nd order), ASA (3rd order), ASAS (4th order), etc., as labeled in Figure 5.1. Light is localized within the last anti-slot or slot introduced and therefore the optical energy is progressively squeezed into smaller and smaller mode volumes. The energy density cross sections shown in Figure 5.1b and Figure 5.1c indicate that the mode profile along the *y*-direction is squeezed only when a slot is introduced while the mode profile along the *x*-direction is squeezed only when an anti-slot is added. Figure 5.3 shows these line traces on a log scale to more clearly show the energy density enhancements of the interlocked and bowtie unit cells compared to the 0th order structure and the fact that the reported energy density of the bowtie structure is a lower bound due to mesh-size limitations in the simulation (2 nm mesh for the bowtie unit cell in Figure 5.1). Magnetic field distributions, which complement the electric field distributions in the anti-slot and higher order interlocked unit cells, are shown in Figure 5.4. The figure clearly shows how the magnetic field distribution is affected by adding an anti-slot to a conventional photonic crystal unit cell that is characterized by a circular air hole surrounded by dielectric material. In the conventional unit cell, the electric field is almost uniform within the air hole (see Figure 5.1) and the magnetic field is strongest in the dielectric surrounding the air hole. In contrast, when the dielectric anti-slot is added to the unit cell, the magnetic field distribution is modified in accordance with Maxwell's equations such that the electric field remains largest along the nodal planes of the magnetic field. Therefore, as expected, we find that the magnetic field distributions shown in Figure 5.4 complement the electric field localizations shown in Figure 5.1 for the unit cells with various interlocking anti-slot and slot designs.

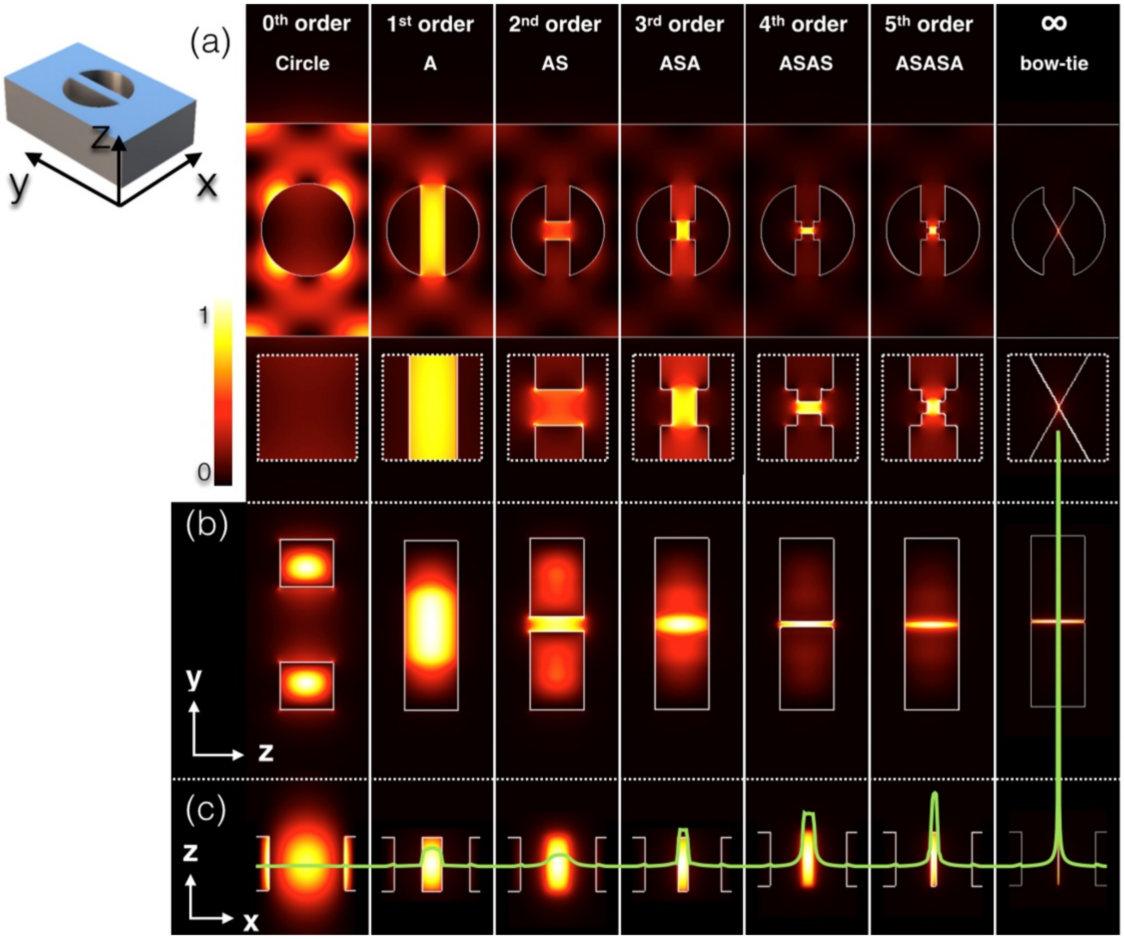

Figure 5.1 Nano-focusing of light into ultra-small mode volumes by progressively interlocking anti-slot and slot designs. (a) Top view (*x*-*y* plane) of the proposed unit cells (air holes in silicon) with increasing numbers of incorporated silicon anti-slots (A) and air slots (S) from left to right. The R90 until cell with one anti-slot is shown schematically for reference. The propagation direction of light is in the *x*-direction. In the limit of an infinite number of interlocked, orthogonal anti-slots and slots, the geometry approaches that of a bowtie shape. (b) and (c) Energy density cross sections (*y*-*z* and *z*-*x* planes, respectively) through the center of the unit cells shown in (a). The line traces in (c) show the electric field energy density of each unit cell (Figure 5.3 shows these line traces on a log scale). All color maps are scaled according to the minimum and maximum values of each individual unit cell. Reprinted with permission from Ref. [96]. Copyright 2016 American Chemical Society.

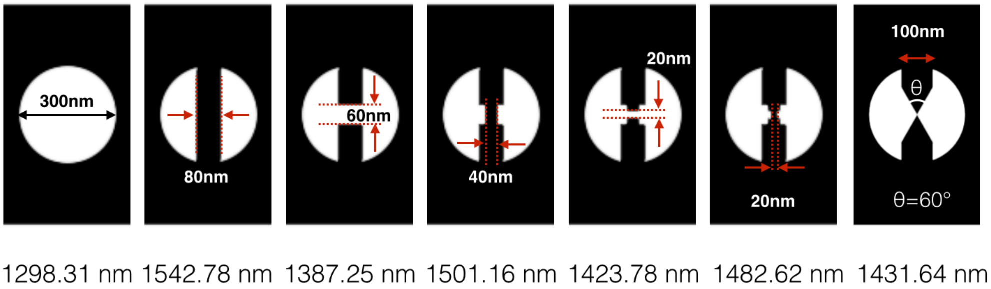

Figure 5.2 Design dimensions of inter-locked unit cells shown in Figure 5.1. The period of each PhC waveguide is 400 nm. The air band edge wavelength for each unit cell is shown below the respective unit cell schematic.

Interlocked configurations of anti-slots and slots lead to stronger light localization compared to non-interlocked configurations having the same final anti-slot width. A 1st order anti-slot unit cell (A) is compared to a 3rd order (ASA) and 5th order unit cell configuration (ASASA), as shown in Figure 5.5. The mode profiles in Figure 5.5a show that the mode becomes more highly localized in the center of the unit cell with increasing orders of interlocked configurations. Figure 5.5b shows the same mode profiles, but with the color map scaled such that the maximum and minimum values of the electric field energy density are the same across all three unit cells. This figure clearly shows that the energy is most confined at the center of the highest order interlocked anti-slot/slot unit cell. Figure 5.5c gives the detailed design parameters of the three unit cell configurations. The ASASA unit cell configuration increases the maximum energy density by a factor of 2 compared to the ASA unit cell and a factor of 5 compared to the single anti-slot unit cell, as shown in Figure 5.5d and e.

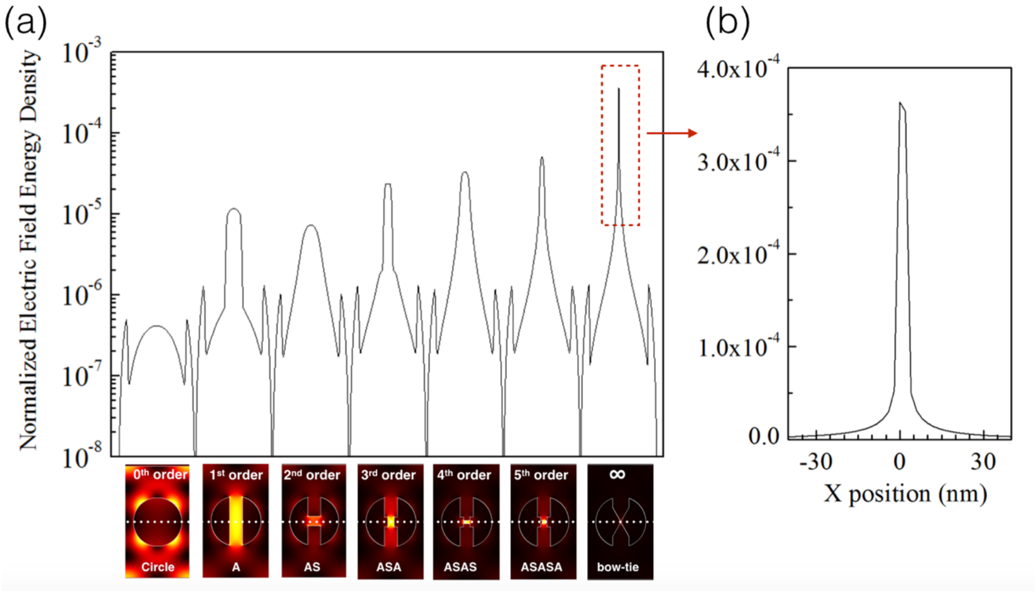

Figure 5.3 Logarithm plot of the line trace shown in Figure 5.1c and mesh-size limited enhancement factor in bowtie unit cell. (a) Comparison of electric field energy density along *x*-axis (*y*=0, *z*=0) of different interlocked anti-slot/slot structures on a logarithm scale. The energy density in the bowtie unit cell is three orders of magnitude higher than that in the 0th order unit cell. (b) Zoom-in plot of bowtie energy density enhancement on a linear scale. The truncated tip at the peak (*x*=0) shows the highest energy density cannot be accurately determined due to the mesh size used in the simulation (2 nm mesh grids). This implies the energy density enhancement of the bowtie unit cell is even higher.

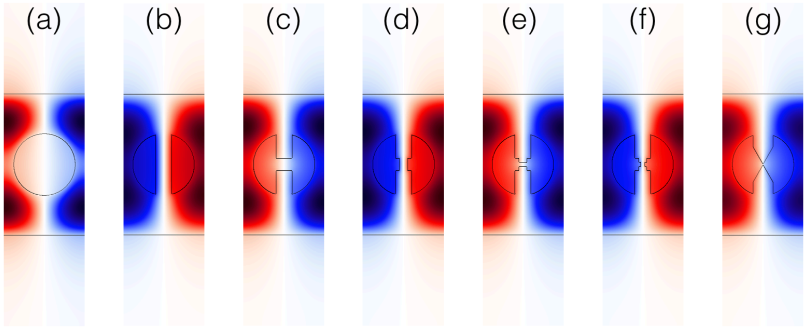

Figure 5.4 Magnetic field distributions in different iterations of slot/anti-slot interlocked unit cells, complementing the electric field distributions in these structures that are shown in Figure 5.1.

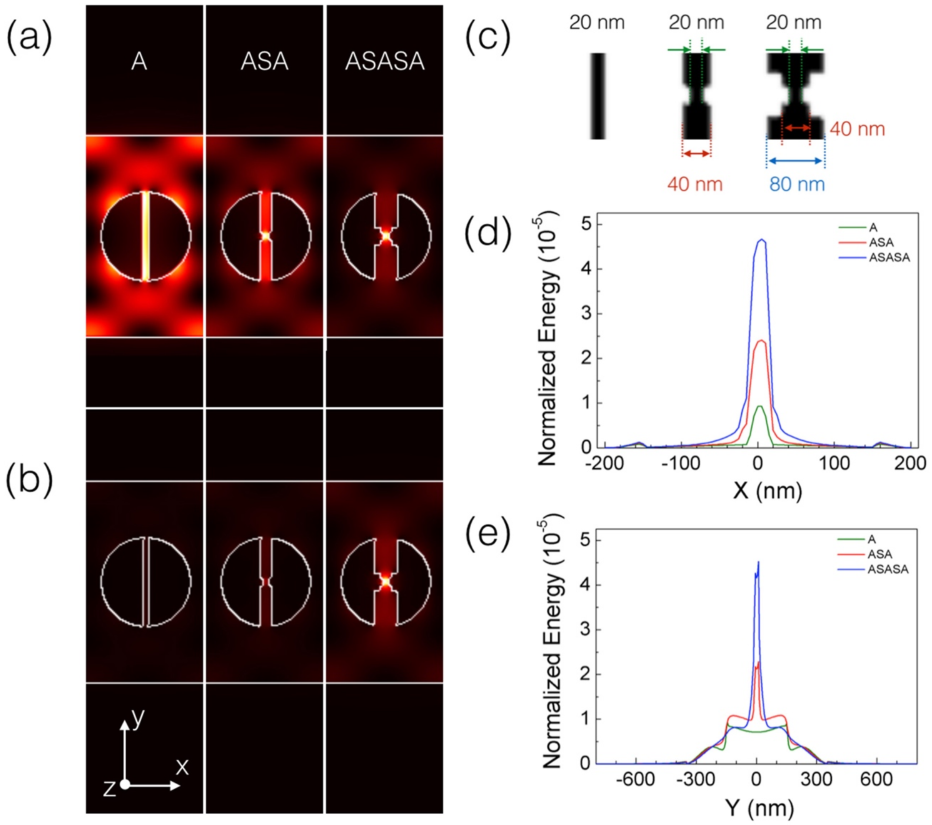

Figure 5.5 Nanoscale focusing of light by alternating anti-slot/slot configurations. (a) Mode profiles of the 1st order, 3rd order, and 5th order interlocked anti-slot/slot unit cells with the same final anti-slot width (20 nm). The color map is scaled according to the maximum and minimum of each individual unit cell. (b) Mode profiles in (a) with color map scaled to the same maximum and minimum electric field energy density across all three unit cells. (c) The geometries of the unit cells. The 1st order has only one 20 nm anti-slot. The 3rd order has a 40 nm anti-slot, a 20 nm slot, and then a 20 nm anti-slot. The 5th order starts with a 80 nm anti-slot, then a 60 nm slot, and then follows the 3rd order design with a 40 nm anti-slot, 20 nm slot, and finally a 20 nm anti-slot. (d) and (e) show the electric field energy density enhancements from a center line profile along the *x*- and *y*-directions, respectively. The energy density is normalized to the total energy of each unit cell.

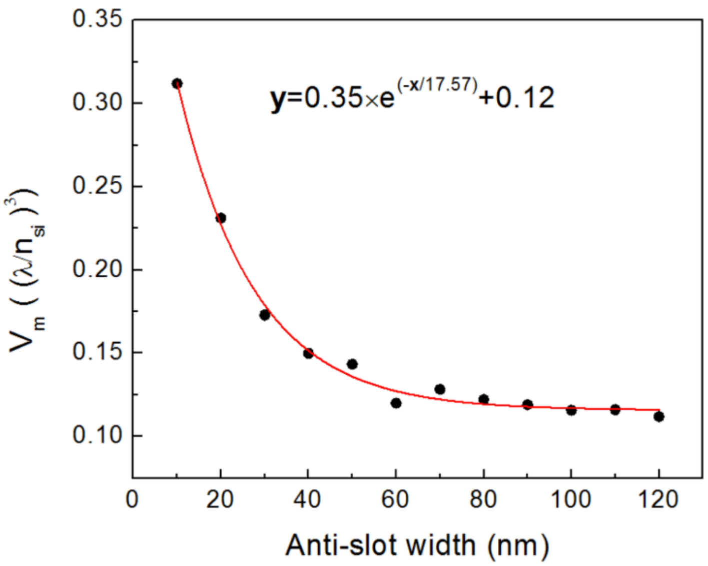

Figure 5.6 Scaling of mode volume with anti-slot width. The increasing mode volume with decreasing anti-slot width implies narrower anti-slots have smaller effective indices. The electric displacement field and electric field energy density enhancements supported by anti-slots are scaled by the effective index of the dielectric beam (assumed to be Si in this calculation) in the anti-slot (R90) unit cell.

Since the dimensions of the anti-slot are in the deep sub-wavelength regime, the electric displacement and energy density enhancements of the anti-slot are related to the effective index rather than the refractive index of Si. Therefore, the energy density does not approach infinity for higher order interlocked anti-slot/slot unit cells (see Figure 5.1 and Figure 5.6). For anti-slots, the effective index decreases from the bulk Si refractive index with decreasing feature size. For slots, the effective index increases from the refractive index of air with decreasing feature size. Therefore, the energy density does not approach infinity as the number of interlocked anti-slots and slots increases.

Figure 5.6 shows how the mode volume increases when the width of a first order anti-slot decreases. The larger mode volume for narrower anti-slots implies a smaller effective index and therefore a smaller enhancement factor for the electric displacement field intensity and energy density of narrower anti-slots. This trend is opposite to that of traditional slots in which the highest field enhancement is achieved in the smallest slot. Extremely low mode volumes can only be achieved in narrow anti-slots when they are integrated into a high order interlocked anti-slot/slot configuration.

In the limit of an infinite number of interlocked anti-slots and slots added to the unit cell, the geometry approaches that of a bowtie shape. The advantages of the bowtie unit cell design are two-fold. First, the design provides extreme sub-wavelength confinement of light with a mode volume that is on par with plasmonic bowtie structures, as discussed in the next section. The energy density in the center of the bowtie structure is 1,500 times higher than the energy density in the center of a 0^{th} order unit cell (Figure 5.1 and Figure 5.3 line traces). Second, a high quality bowtie structure is easier to fabricate with high fidelity compared to a high order interlocked geometry. Importantly, unlike plasmonic bowties, all-dielectric bowties support the design freedom and fabrication tolerance to allow extreme light localization in either an air gap or a dielectric connection between the two sides of the bowtie, while maintaining a high Q [107]. If there is an air gap between the tips such that the interlocked geometry ends with a slot, then energy is confined to that air gap. Alternatively, if there is no gap between the tips, corresponding to an interlocked geometry ending with an anti-slot, then energy is confined within the tiny region of dielectric material spanning the tips.

5.3 Design of high *Q* photonic crystal cavity with deep sub-wavelength confinement

In this section, we demonstrate the capabilities of the proposed bowtie PhC unit cell to form a cavity with deep subwavelength confinement comparable to plasmonic elements and ultra-high *Q* on par with PhC structures. Such a combination of ultra-low V_m and ultra-high *Q* was previously thought to be impossible for an all-dielectric structure. The confinement of light in a bowtie PhC cavity can be intuitively understood as a two-step process. First, light is confined within a unit cell by the well-known band gap confinement of PhCs. Then, the optical field within the unit cell can be redistributed by modifying the dielectric profile inside the unit cell where electromagnetic boundary conditions must still be satisfied – the dielectric bowtie design is one example of such a dielectric profile modification. Since the first step of light confinement is simply based on the creation of a photonic band gap, many different approaches can be employed to design the PhC cavity confinement of a bowtie PhC cavity. Any degree of freedom in the unit cell that perturbs the band structures can be used to design a PhC cavity. In this work, we demonstrate bowtie PhC cavities by modifying the (a) rotating the angle and (b) changing the air hole size of the bowtie unit cell presented above.

5.3.1 Rotational angle modulated PhC cavity

We select the bowtie unit cell for this demonstration and spatially vary the rotation angle of the unit cell to create a cavity. Figure 5.7 shows the band edge (k=0.5) frequencies of dielectric bowtie unit cells with different rotation angles. Similar to the band diagram in Figure 4.10 for R0 and R90 unit cells, the air band of the R90-bowtie lies in the middle of the R0-bowtie band gap.

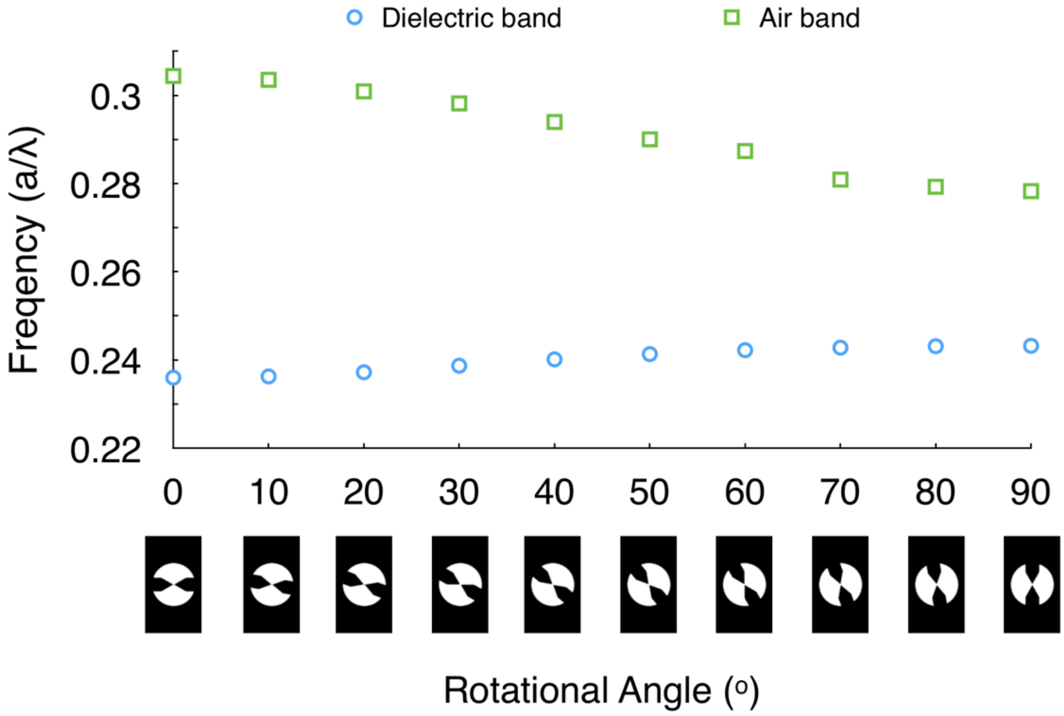

Figure 5.7 Band diagrams of dielectric bowtie unit cell with different rotation angles. The air band of the R90 bowtie unit cell falls in the middle of the band gap of the R0 bowtie unit cell. It is therefore possible to design a cavity to confine the band edge mode of a R90 unit cell by using R0 unit cells. Rotating the bowtie provides a natural way to taper the cavity from R0 to R90 and back to R0. Reprinted with permission from Ref. [96]. Copyright 2016 American Chemical Society.

Accordingly, we place a R90-bowtie unit cell in the center of the cavity and use R0-bowtie unit cells to create mirrors on either side of the cavity. As is the case for all 1D PhC cavities, the *Q* factor is governed in large part by the selected band gap tapering from the cavity to mirror unit cells and the number of mirror unit cells. For simplicity, we choose to transition between the R0-bowtie mirror segments and the cavity center R90-bowtie unit cell by rotating the intermediary bowtie unit cells by 5 degrees per step in the taper segments as schematically illustrated in Figure 5.8a. Ten R0-bowtie unit cells are placed at each end of the PhC, serving as mirrors at the end of the cavity. The taper segments between the mirrors and cavity increase the mode volume. However, in order to support a high Q-factor resonance, it is essential to form a Gaussian mode profile that minimizes losses. The bowtie PhC cavity possesses an ultrahigh Q of 1.76×10^6 at a resonance wavelength of 1496 nm with an ultra-small V_m of 5.6×10^{-4} $(\lambda/n)^3$. Since the cavity is designed using slot terminated bowtie unit cells, the optical energy is highly localized in the air gap between the bowtie tips, as shown in Figure 5.9, and the refractive index n given in the mode volume of the bowtie PhC cavity is close to that of air. The mode volume is calculated as follows:

$$V_m = \frac{\int \epsilon |E|^2 \, dV}{\max\left(\epsilon |E|^2\right)} \tag{5.1}$$

The mode profile shown in Figure 5.8b along with a superimposed outline of the dielectric structure reveals that the electric field energy is concentrated between the bowtie tips, similar to the case for a plasmonic bowtie hot spot. By plotting the energy distribution on a log scale in Figure 5.8c, it is clear that the mode decays gradually into the mirror segments, giving a Gaussian-shaped electric field profile (Figure 5.8d) that minimizes radiation losses. The Fourier transformed field distribution shown in Figure 5.8e confirms that the field components are localized at $k=\pm\pi/a$ with minimal extension into the light cone. The electric field in the cavity center is more than 10^3 times stronger than that in a planar waveguide ($\boldsymbol{E_0}$), and therefore the electric field energy density is more than 10^6 times larger than the input waveguide energy density, as confirmed in the electric field energy profile shown in Figure 5.8f. This is the highest electromagnetic energy enhancement factor reported to date and it is at least two orders of magnitude larger than what is achieved in a plasmonic bowtie cavity. We note that optimization of the design parameters, such as the angle of the bowtie tip, the rotation step of tapering segments, and the number of mirror segments, may lead to bowtie PhCs with an even higher Q/V_m ratio.

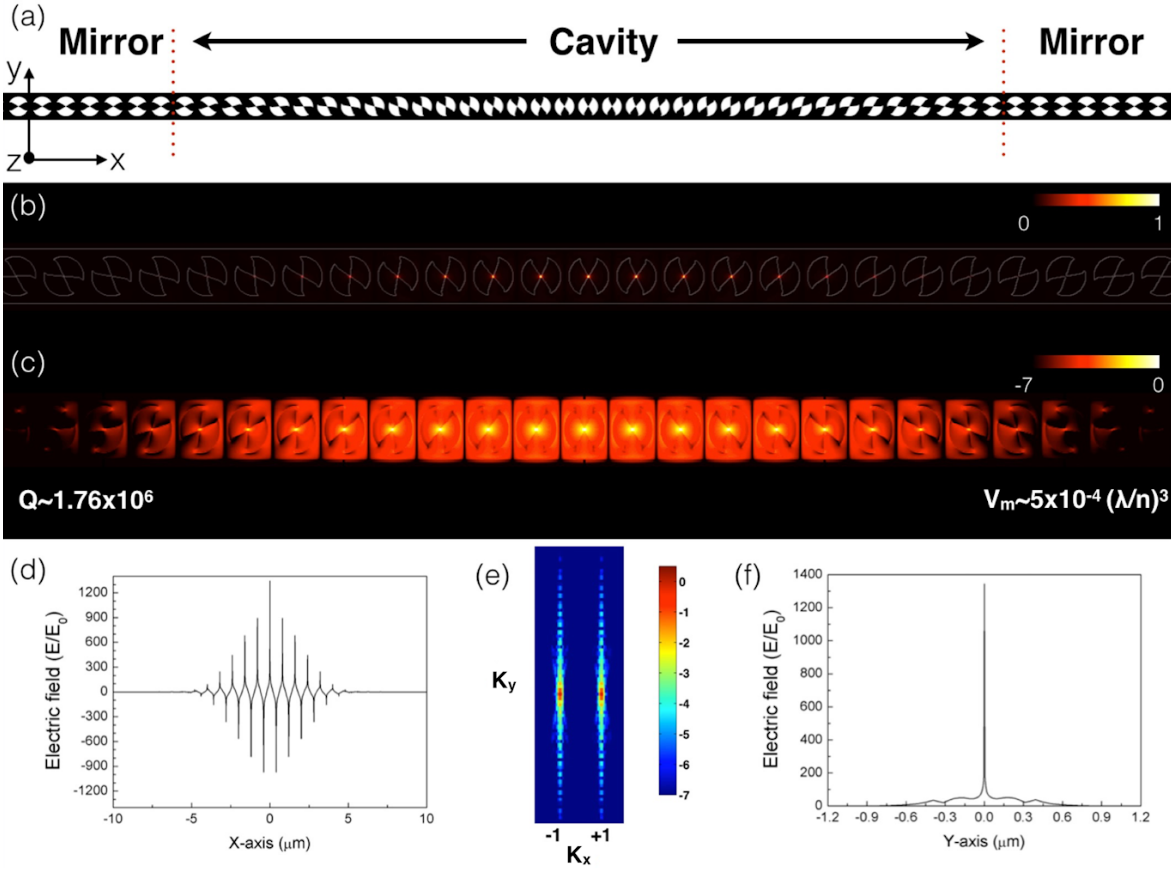

Figure 5.8 1D photonic crystal cavity design based on a bowtie unit cell. (a) The photonic crystal cavity is formed by gradually rotating a silicon bowtie unit cell from the R0-bowtie orientation in the mirror segments to the R90-bowtie orientation in the center of the cavity (5 degree rotation per unit cell). The calculated Q and V_m are 1.76×10^6 and 0.0005 $(\lambda/n)^3$, respectively. (b) Linear and (c) log plot of mode profile with dielectric structure superimposed. (d) Electric field profile along a horizontal slice through the middle of the photonic crystal showing a gradual modulation of the electric field from cavity center to mirror edges. (e) 2D Fourier transform of the electric field distribution in (d), demonstrating good in-plane confinement of the mode. (f) Electric field energy profile along a vertical slice through the center of the bowtie photonic crystal cavity showing extreme energy localization. The electric field intensity in (d) and (f) are normalized to the maximum electric field intensity in a ridge waveguide (E_0). Reprinted with permission from Ref. [96]. Copyright 2016 American Chemical Society.

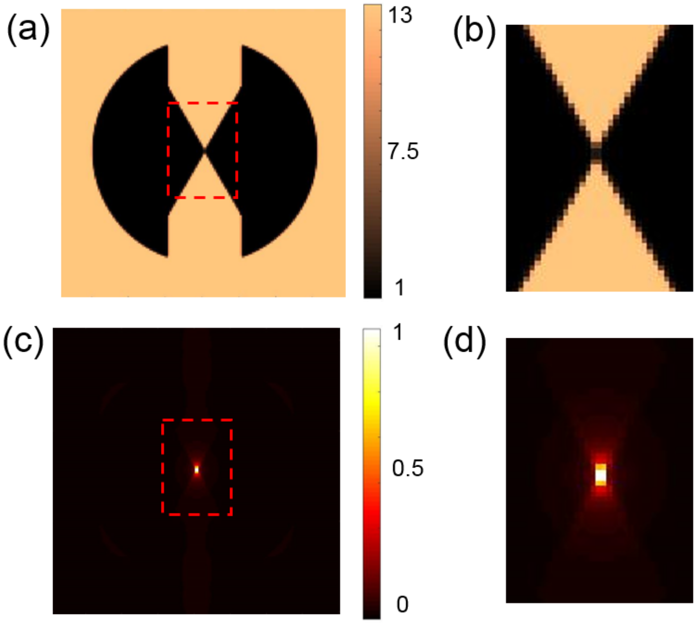

Figure 5.9 Magnified images showing the dielectric and mode profiles in the center of the bowtie PhC unit cell. (a) Dielectric profile of the R90 bowtie unit cell. The beige color represents Si and black represents air. The mesh grid size is 2 nm. (b) Magnified image of the region in the red box in (a). (c) Mode profile of the bowtie unit cell shown in (a). (d) Magnified image of the region in the red box in (c). Both (b) and (d) show the same region.

5.3.2 Bowtie photonic crystal cavity designed by modulating the air hole radius

Figure 5.10a shows a PhC designed by varying the radius of the bowtie unit cell. The air hole radius is set to 150 nm for the center cavity unit cell and 187 nm for the mirror unit cells at each end of the cavity. The radius modulated bowtie PhC cavity is simulated using 3D FDTD analysis with a mesh size of 4 nm. The resonance wavelength is 1529 nm. The tapering strategy for the unit cells between the cavity center and end mirrors follows a quadratic modulation of the air hole radius. The air hole radius for each unit cell in the taper region is defined as:[99]

$$r_i = r_0[1 + \left(\frac{i}{m}\right)]^2 \tag{5.2}$$

where *m* can be found from

$$r_m = r_0[1 + \left(\frac{N_c}{m}\right)]^2 \tag{5.3}$$

and *i* is the index number of the unit cell starting from the center of the cavity and moving symmetrically outward on each side of the cavity, N_c is the number of taper unit cells on each side of the center cavity, r_m is the air hole radius of the mirror unit cell, and r_c is the air hole radius of the center cavity unit cell. The central cavity unit cell is indexed as r_0 such that $r_0 = r_c$.

As shown in Figure 5.10b, the cavity *Q* exponentially increases with an increased tapering length between the cavity center and mirror unit cells while the mode volume increases linearly with tapering length, as shown in Figure 5.10d. These trends are consistent with previous reports on conventional dielectric mode nanobeam cavities with circular hole unit cells [95, 99]. An alternate approach to increasing *Q* without impacting the mode volume is to add more mirror unit cells, as shown in Figure 5.10c and d. Increasing the number of mirror unit cells increases the confinement strength of the mirrors, which improves overall light confinement in the cavity without affecting the mode distribution in the cavity region. However, increasing the mirror strength will also make the cavity more challenging to couple into using an in-line coupling approach such as grating-coupling or butt coupling using tapered fibers.

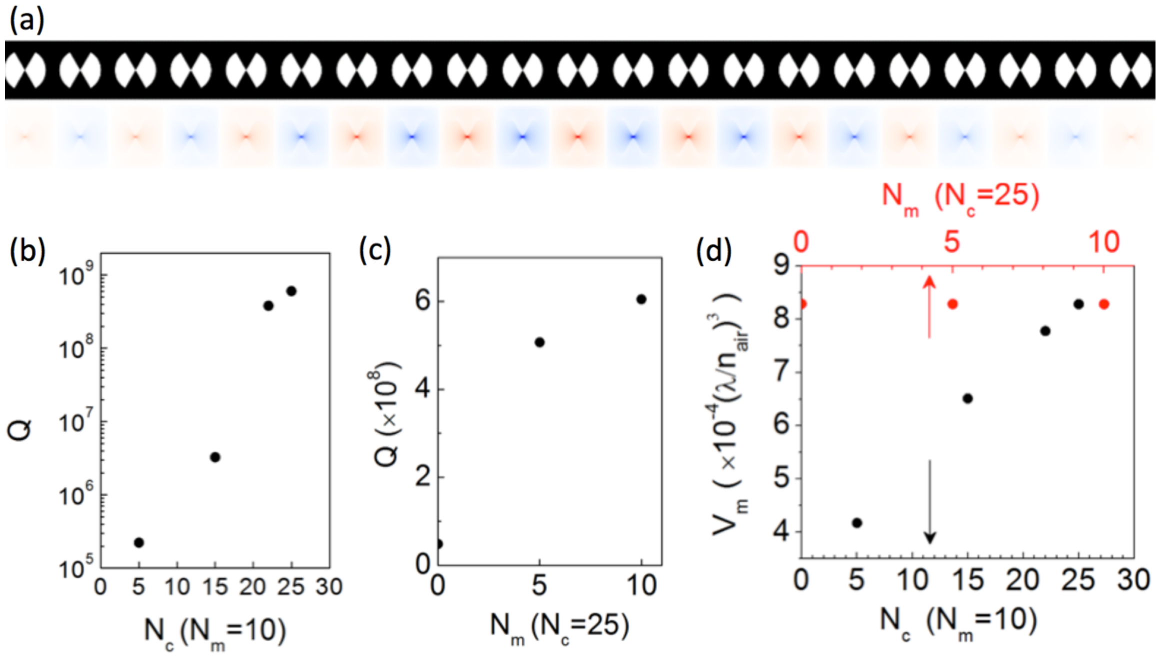

Figure 5.10 Design of bowtie cavity by modulating the air hole size within the PhC unit cell. (a) Dielectric profile of radius modulated bowtie PhC design (white = air, black = Si) in the region near the cavity center and corresponding resonance mode profile. Dependence of bowtie cavity *Q* on (b) number of taper unit cells (N_c) between the cavity center and mirror unit cells and (c) number of mirror unit cells (N_m). While the *Q* increases with both N_c and N_m, the functional dependence is different. (d) Mode volume dependence on number of taper and mirror unit cells. The mode volume linearly depends on tapering length but shows little dependence on the number of mirror unit cells because the mode does not significantly extend into the mirror region of the structure.

5.3.3 Design of bowtie PhCs based on other degrees of freedom

As introduced in Chapter 4, using our *de novo* design method, a PhC cavity can be designed based on any degree of freedom. Specific applications may require a design other than rotational and hole-size modulation. In additional, fabrication process may have different design tolerances.

Therefore, it is important to find the most appropriate degree of freedom in design that can be realized with high fidelity fabrication to enable the desired applications.

As an example, the PhC cavity could be designed based on a new degree of freedom not considered in this thesis: the connection width of the bowtie. As shown in Figure 5.11, the air band edge frequencies have a strong dependence on the connection width of bowtie, while the dielectric band edge frequencies are almost constant. This is because in the air mode the majority of the optical energy is at the bowtie tip connection and is highly sensitive to changes in the surrounding refractive index, while in the dielectric mode, majority of the light is in the silicon region between the air holes, and refractive index changes in the center of the air holes have very little overlap with the optical field. We note that for simplicity, the unit cell design in Figure 5.11 does not have a V-groove.

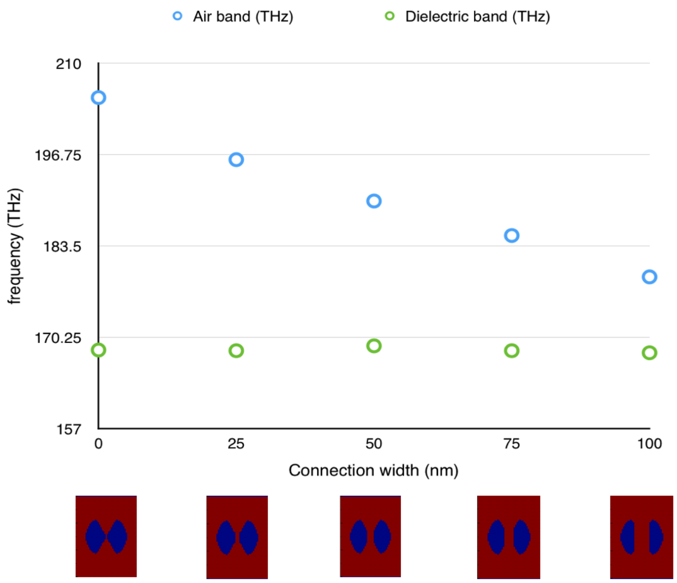

Figure 5.11 Band gap changes with respect to the change of bowtie connection width.

5.4 E-field enhancement of designed bowtie cavity

In order to further investigate the energy density enhancement in the bowtie PhC nanobeam cavity, which we attribute to both the high Q and low V_m of the designed cavity, we carried out a simulation to determine the electric field distribution of an air mode in a traditional 1D PhC nanobeam cavity with a nearly identical Q to a bowtie PhC cavity. Hence, the only difference between the two PhC cavities is the unit cell design and resulting mode volume. Following the parameters described in Ref. [108] (nanobeam width = 700 nm, thickness = 220 nm. $N_c = 25$, $N_m = 0$, $a = 450$ nm, diameter of air holes varies from 297 nm at the edge of the cavity to 228 nm at the center of the cavity), an air hole radius modulated PhC nanobeam was simulated and was found to have $Q = 8\times10^8$, as shown in Figure 5.12a and b [108]. Based on the simulations described in Figure 5.10, a radius modulated bowtie PhC was then designed to have a similar Q ($N_c = 25$, $N_m = 10$, $Q = 6\times10^8$), as shown in Figure 5.12c and d. Therefore, with the simulation time fixed at 10^4 fs, the fraction of field decay occurring in each cavity during the simulation time window should be approximately the same for both designs and the electric field intensities of the cavities can be directly compared. Examination of the electric field distributions in Figure 5.12b and Figure 5.12d reveals that the peak electric field intensity of the traditional PhC nanobeam cavity with a circular air hole unit cell is ~ 500, while the peak electric field intensity of the bowtie PhC cavity is ~ 24,000. Therefore, the bowtie PhC cavity exhibits ~ 50 times higher electric field strength (~2500 times higher energy density) in the cavity center compared to a traditional 1D PhC cavity with similar Q. The smaller mode volume in the bowtie PhC cavity (Figure 5.12d compared to Figure 5.12b) explains this enhancement as the bowtie design facilitates spatial localization of the electric field within the unit cell. We note that the enhancements found here are consistent with the energy density enhancement factor reported in Figure 5.1 for the propagation modes of PhC waveguides (*i.e.*, no cavity enhancement).

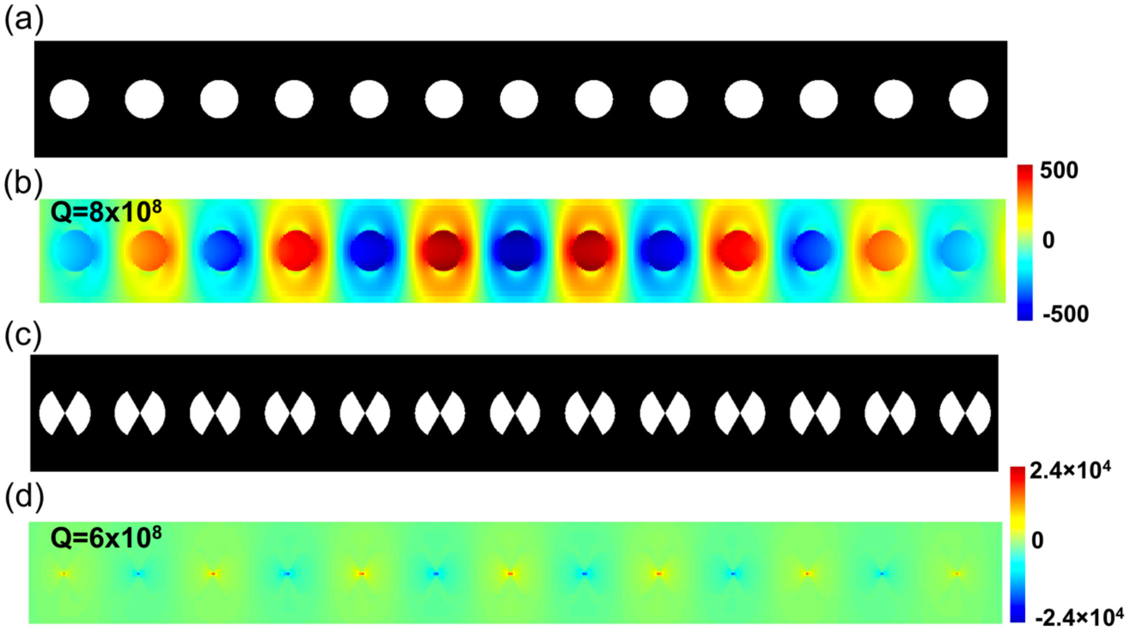

Figure 5.12 Comparison between traditional 1D PhC cavity with circular air holes and bowtie PhC cavity. (a) Dielectric profile and (b) mode distribution on resonance (λ= 1570.42 nm) of traditional PhC cavity. (c) Dielectric profile and (d) mode distribution on resonance (λ = 1530.45 nm) of the bowtie PhC cavity. In the dielectric profiles, black represents Si and white represents air.

5.5 Further confinement enhancement using V-groove

The manipulation of two boundary conditions in Figure 5.1 also applies to the cross-section of a waveguide. Figure 5.13 shows how the optical mode changes when alternating boundary conditions supporting the slot and anti-slot effects are applied at the cross-section. Here, we assume the light is TE polarized (*i.e.*, electrical field parallel to the y axis) and propagates along the x axis. A traditional slot cuts the waveguide into two halves along the y axis and pushes optical energy into the slot region. If a connection bar is placed across the slot, the energy will be confined into this added connection bar by the anti-slot effect. Following the same analysis as in Figure 5.1, optical energy is progressively squeezed into smaller spatial extents as the interlocking of slots and anti-slots goes to higher orders, as showed in Figure 5.13. However, such higher order interlocked designs of a waveguide cross-section are not practical for fabrication. A feasible solution is to simplify the higher order slot and anti-slot interlocked configuration to be a V-groove at the center, as shown in Figure 5.14. The optical energy is pushed down to the bottom tip of the V-groove, resulting in a significantly reduced modal area of the waveguide.

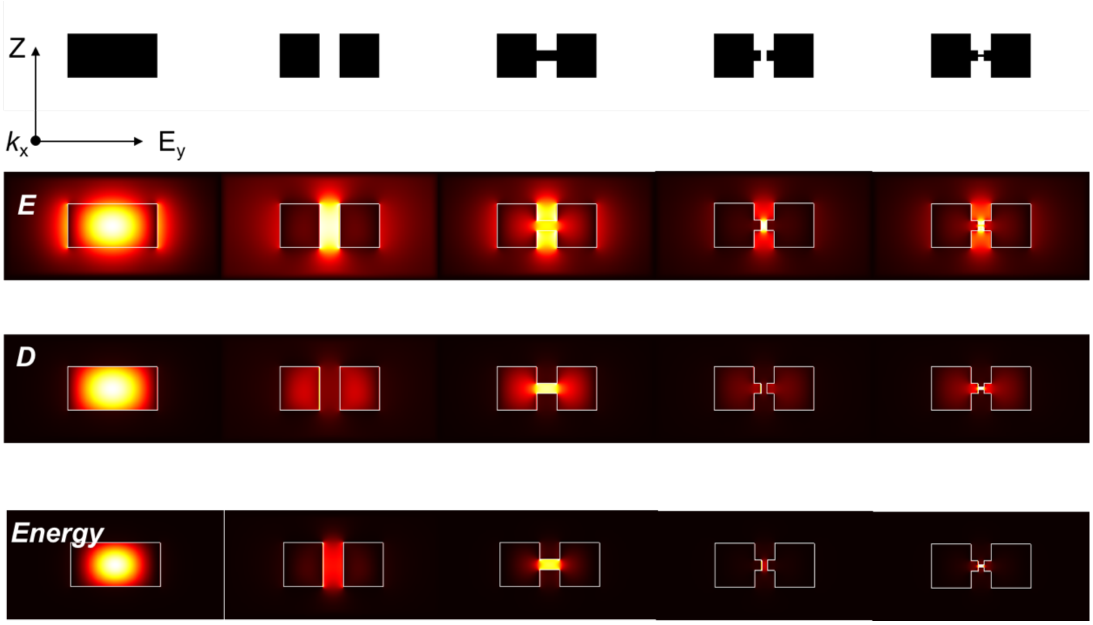

Figure 5.13 Various orders of interlocked slot and anti-slots in the cross-section of a waveguide. Higher order structures support lower mode volumes.

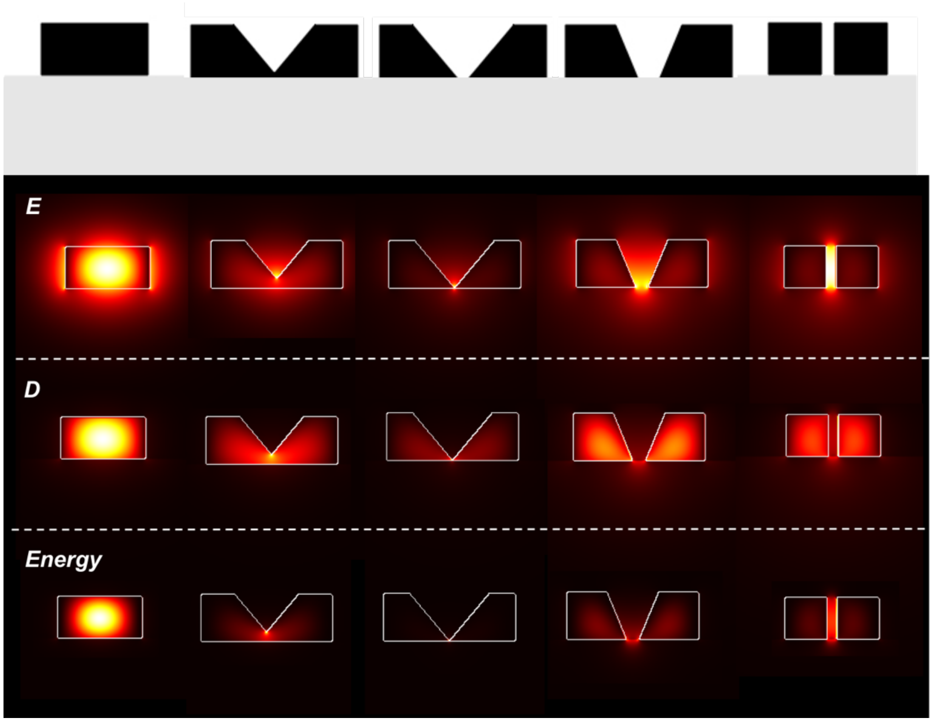

Figure 5.14 A practical design of a V-groove waveguide for optical energy confinement in the *z*-direction.

A new unit cell combining the bowtie unit cell presented earlier and the V-groove is proposed in Figure 5.15. The PhC cavity is designed based on hole size modulation. The radius of the cavity center unit cell is r=150 nm; the radii of neighboring unit cells gradually increases with distance in a quadratic fashion from the cavity center to r=187 nm at the mirror unit cells. Band diagrams for both cavity and mirror unit cells are shown in Figure 5.15b. Cavity mode profiles at the band edge (k_x=0.5) show that the optical energy is well-confined at the tips of bowtie and also squeezed in the *z*-direction by the V-groove. The Q-factor of a cavity with 20 taper unit cells and 10 mirror unit cells is 6.5×10^{6}. V_m is calculated to be 6×10^{-4} μm^3. V_m is usually normalized to the wavelength in the material, as shown in the Purcell factor calculation:

$$F_p = \frac{3}{4\pi^2}\left(\frac{\lambda}{n}\right)^3\left(\frac{Q}{V_m}\right) \tag{5.4}$$

In this design, the optical mode exists in both air and silicon. The index n should be an effective index between n_{air} and n_{si}. To decide the exact effective index requires rigorous simulations, we therefore make a simplification and normalize to the wavelength in silicon: $V_m = 6\times10^{-3}\,(\lambda/n_{si})^3$. We note that this number represents the highest bound of the normalized V_m. The lower bound is the number normalized to the wavelength in air: $1.6\times10^{-4}\,(\lambda/n_{air})^3$.

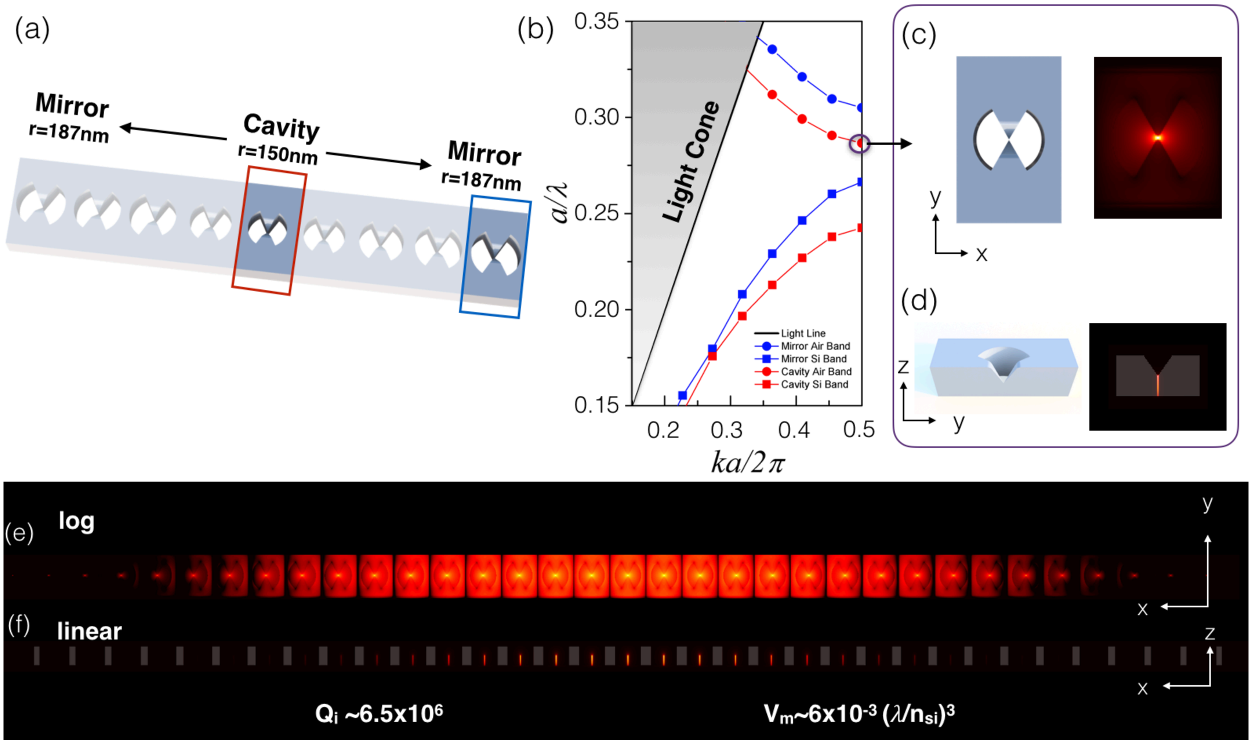

Figure 5.15 Design of the photonic crystal using a bowtie shaped unit cell. (a) The cavity is formed with a center unit cell of 150 nm radius and mirror unit cells of 187 nm radii on both sides. The air hole size is gradually tapered from the center to the mirror segments. (b) The optical band structures of the cavity unit cell (red curve) and mirror unit cell (blue curve). (c) and (d) are top view (*xy* plane) and cross-section view (*yz* plane) of the air band edge mode of the center unit cell. (e) and (f) are the simulated resonance mode of the complete photonic crystal cavity. (e) Log plot of the resonance mode in the *xy* plane at $z = 0$ (at the half thickness). (f) Linear plot of the side-view resonance mode (*xz* plane) at $y = 0$.

5.6 Experimental considerations

5.6.1 Bowtie tip rounding

Fabricated bowtie PhCs are likely to have rounded instead of triangular tips. Therefore, to better understand the potential impact of this fabrication issue, we carried out simulations on a bowtie PhC with rounded bowtie tips (Figure 5.16). In order to resolve the curvature of the tips, the mesh size at the center of the unit cell (-1/2 radius to 1/2 radius of air hole) is chosen to be 1 nm. The gap between the tips is 8 nm. Using a radius modulated bowtie PhC cavity design with the same parameters as the bowtie cavity described in Section 5.3.2, we find that the rounded tip design is characterized by $Q = 7 \times 10^7$ at a resonance wavelength near 1563 nm and $V_m = 1.003 \times 10^{-3} (\lambda/n_{air})^3$. Hence, the bowtie cavity with rounded tips maintains deep subwavelength confinement with only a slightly decreased Q and slightly increased V_m compared to the same cavity with sharp pointed tips ($Q = 6 \times 10^8$ and $V_m = 8 \times 10^{-4} (\lambda/n_{air})^3$, as presented in Section 5.3).

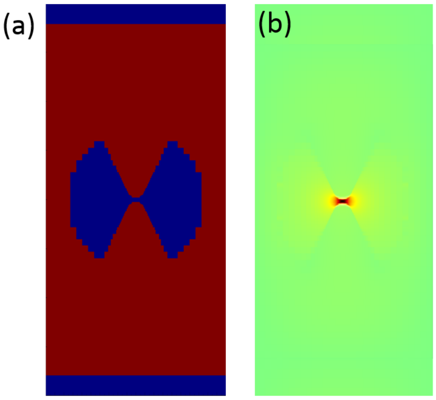

Figure 5.16 Simulated unit cell in bowtie cavity with round bowtie tips. (a) Dielectric profile: red color represents Si and blue color represents air in the simulation. (b) Electric field profile ($\boldsymbol{E}_y$) of structure shown in (a).

5.6.2 Fabrication imperfections

The most detrimental fabrication imperfection for a PhC is inconsistency across different unit cells. In the bowtie PhC cavity, the majority of the electric field is confined between the two tips of the bowtie. Therefore, consistency of the tip profile across all unit cells is crucial for obtaining a high Q-factor. In order to investigate the fabrication tolerance to unit cell variations, we performed a simulation with a very rough mesh condition, as shown in Figure 5.17. A radius modulated bowtie PhC cavity design with 25 taper unit cells and 10 mirror unit cells (as presented in Section 5.3.2) was used for the investigation. The mesh size in each circular region encompassing the bowtie (illustrated by white dotted line in Figure 5.17) is defined as $r/15$, such that the mesh grid size varies as the radius changes in the radius modulated cavity. As a result, some bowtie tips are meshed as an air gap while others have a dielectric connection between the bowtie tips. This approach simulates the lowest bound of fabrication quality, which has a Q-factor of $\sim 2.6 \times 10^4$. We note that the mode volume could not be accurately calculated from this simulation due to the chosen mesh conditions. When the same radius modulated bowtie PhC cavity was simulated with a finer, uniform 4 nm mesh (as in Section 5.3) that allows the bowtie tips of all unit cells to be resolved in the same way with a small air gap, the resulting Q-factor is four orders of magnitude larger ($\sim 6 \times 10^8$).

Based on the presented analysis of bowtie tip rounding and fabrication induced unit cell inconsistency, it is highly likely that state-of-the-art CMOS lithography techniques will be able to produce high Q and low V_m bowtie PhC cavities.

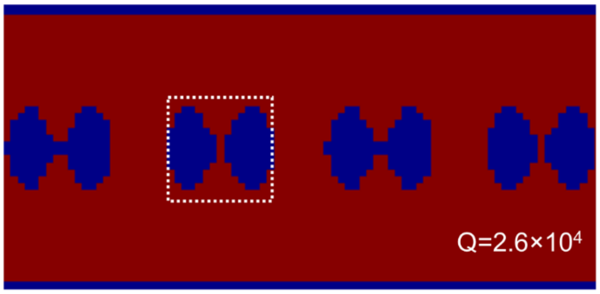

Figure 5.17 Effect of different mesh conditions in FDTD simulations. A course mesh is used to simulate a worst case scenario for the fabrication imperfection of inhomogeneity across PhC unit cells. The cavity Q is significantly degraded when the dielectric profile of the bowtie changes from unit cell to unit cell. The red color represents Si and the blue color represents air in the simulation. The white dotted square illustrates the specially meshed region.

5.7 Fabrication of Designed Bowtie Photonic Crystal Waveguides and Cavities

Because the exact dimensions of the bowtie connection region directly determine the degree of mode confinement, as discussed in Section 5.2, experimental realization of high Q and low V_m PhC cavities requires precise fabrication, demanding a critical dimension less than 10nm. This section will discuss the fabrication steps, challenges, and corresponding solutions to fabricate high fidelity bowtie PhC devices. All devices presented in this chapter were fabricated at the Microelectronics Research Laboratory (MRL) at the IBM Thomas J. Watson Center in Yorktown Heights, NY. There are four major steps in the fabrication process (Figure 5.18). First, global markers are patterned onto the wafer through deep ultraviolet (DUV) lithography for multi-step alignment. The second step is to expose the device patterns in electron beam lithography (EBL) and transfer them onto the Si layer through reactive ion etching (RIE). The third step is to define a SU8 polymer coupler to improve the coupling between the fiber tips (*i.e.*, originating from a fiber-coupled laser and commonly terminated with lensed fiber) and on-chip waveguide. The last step, which is followed only if undercutting of the PhC is desired, involves a wet etch to remove the oxide substrate and form a suspended structure.

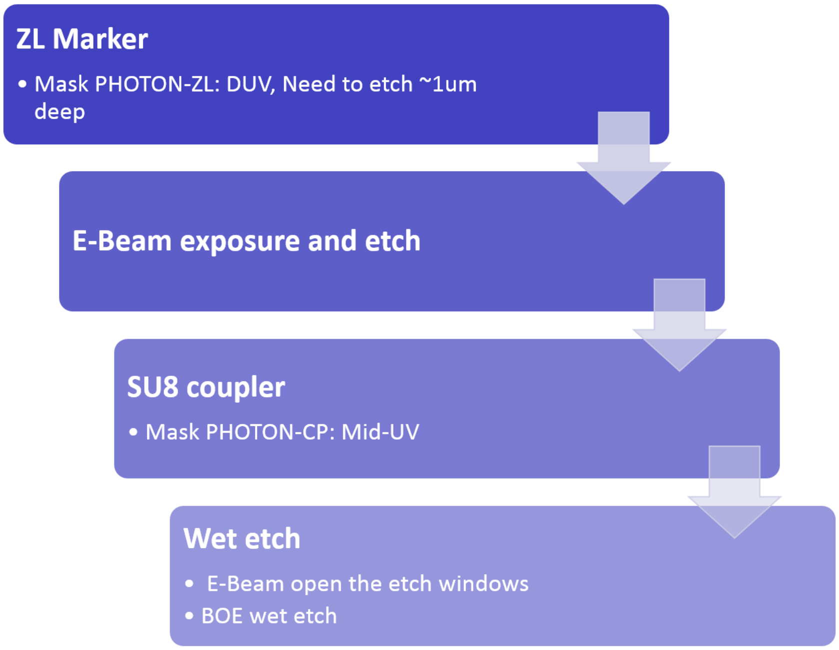

Figure 5.18 Outline of fabrication process.

The PhC fabrication is carried out on a standard 200 mm CMOS fab line at the MRL. The etch depth of zero level (ZL) global markers needs to be around 1μm to obtain a clear contrast for accurate alignment during EBL. A Leica VB6-HR 100 kV electron beam lithography system is used to expose the designed pattern onto a thin layer of hydrogen silsesquioxane (HSQ) resist after the ZL marker etching is completed. To achieve high resolution definition of the pattern, the HSQ thickness is small - only 20 nm. However, a 60 nm organic planarization layer (OPL) is spun onto the substrate before the HSQ film to serve as a polymer hard mask that allows sufficient selectivity during pattern transfer to the substrate. After exposure and development, the patterns are transferred into the OPL and Si device layers through two different RIE steps. Post RIE, the wafer is thermally oxidized to form a 4 nm oxide liner for partial recovery of etching damage and protection during subsequent processing.

The most challenging part of the fabrication is to accurately resolve the bowtie tip with a sharp angle and define the V-groove at the bowtie connection. This is done by an innovative process developed for the bowtie PhC fabrication. A dose gradient is assigned in the EBL exposure, as shown in Figure 5.19. The dose at the bowtie center is increased by 300% with an additional 135% spot-dwell shot at center. The advantage of overdosing the bowtie tips is two-fold. First, the smallest features are resolved better using higher EBL doses. Especially in the bowtie design, the specified critical dimension is less than 10 nm, which translates to only 2 to 4 electron beam shots in the exposed area (FWHM of electron beam is about 5 nm). Therefore, it is important to increase the dwell time (dosage) at these regions to fully expose the resist. Second, the dose gradient is likely to result in a gray scale resist thickness profile, which can be transferred to the Si layer in the next step to form a V-groove. Figure 5.20 shows the detailed process to form a V-groove at the center of the bowtie. The etching step and thermal oxide growth that follow EBL further increase the cutting depth of the V-groove. SEM images of the device after each step is shown in Figure 5.21. The Si structure mostly follows the EBL resist mask patterns, with only slight shrinking of the bowtie width at the tip region.

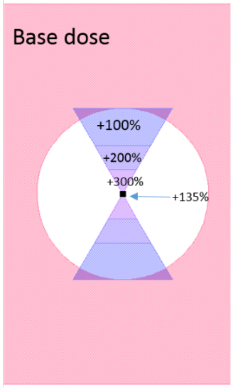

Figure 5.19 Dose gradient of the bowtie region to improve resolution of the tip and form a V-groove in the out-of-plane direction.

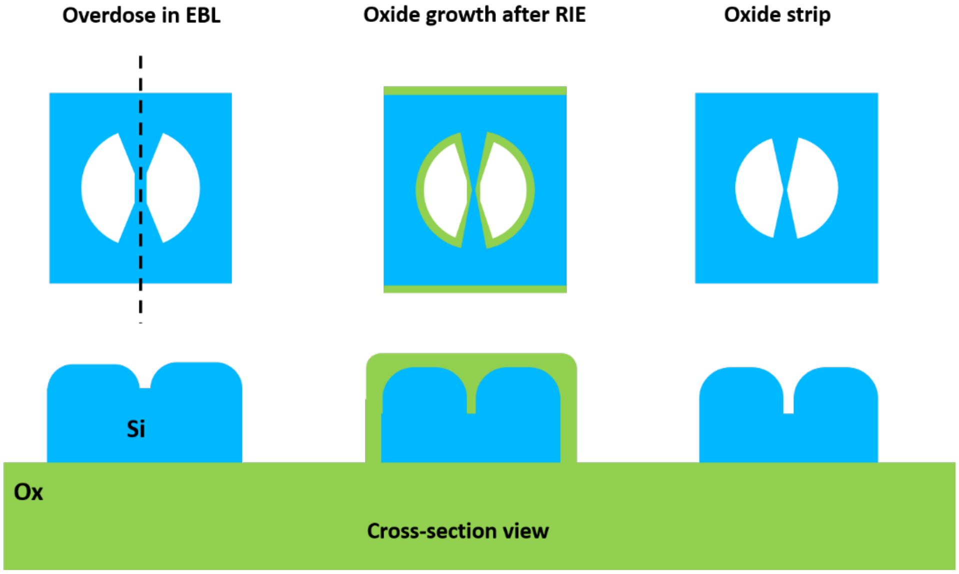

Figure 5.20 Process to define V-groove in the center of the bowtie connection region.

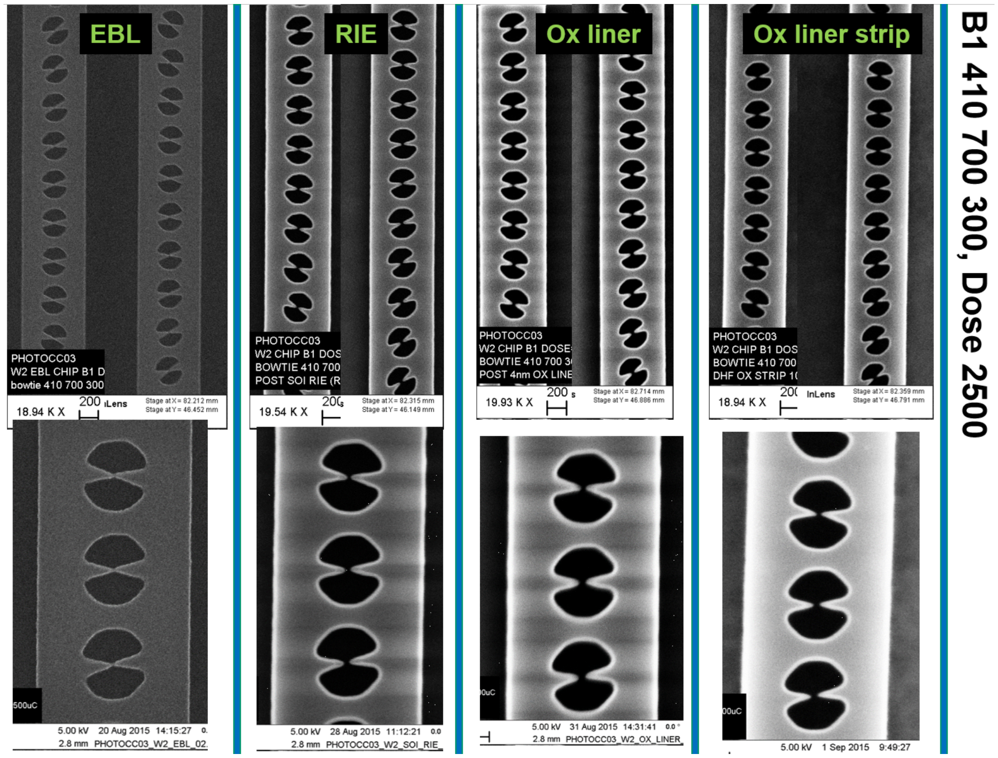

Figure 5.21 SEM images of bowtie cavities after each fabrication step.

Using a technique similar to what has been previously reported, polymer mode couplers are fabricated using spun on negative resist (SU-8) and mid-UV (MUV) lithography to improve the coupling and reduce back reflections from the cleaved facets [109]. Figure 5.22 shows the SEM images of the chip after SU8 integration. The cross section of the SU8 polymer coupler is approximately 3 μm × 2 μm. The coupling efficiency is increased by 10 dB and the Fabry-Perot fringe amplitude is decreased from 2 dB to 0.4 dB when the SU8 coupler is added.

Once the devices and polymer couplers are fabricated, depending on the future application, an undercut step can be applied to release the photonic device from oxide substrate and form a suspended structure. A9 PMMA is first spin-coated at 3000 rpm onto the wafer and then windows are opened over the PhC cavity regions via EBL, using the alignment markers from the first fabrication step. The underlying BOX is etched away using Buffered HF (BHF) for 8 minutes. To achieve the best wet etching result, we take the sample out after every 1 minute in BHF solution, rinse it with DI water, dry it with nitrogen, and then put it back again. We repeat it for 8 times, giving a total etching time of 8 minutes. The PMMA resist layer is then removed with a 10-minute soak in acetone, rinsed with acetone and isopropyl alcohol, and dried with nitrogen. Figure 5.23a and b show the optical images before and after the undercut. The interference pattern around the undercut window under optical microscope in Figure 5.23b indicates the undercut distance. Figure 5.23c-f show SEM images after the undercut. The tilted image clearly shows the V-groove profile at the center of the bowtie.

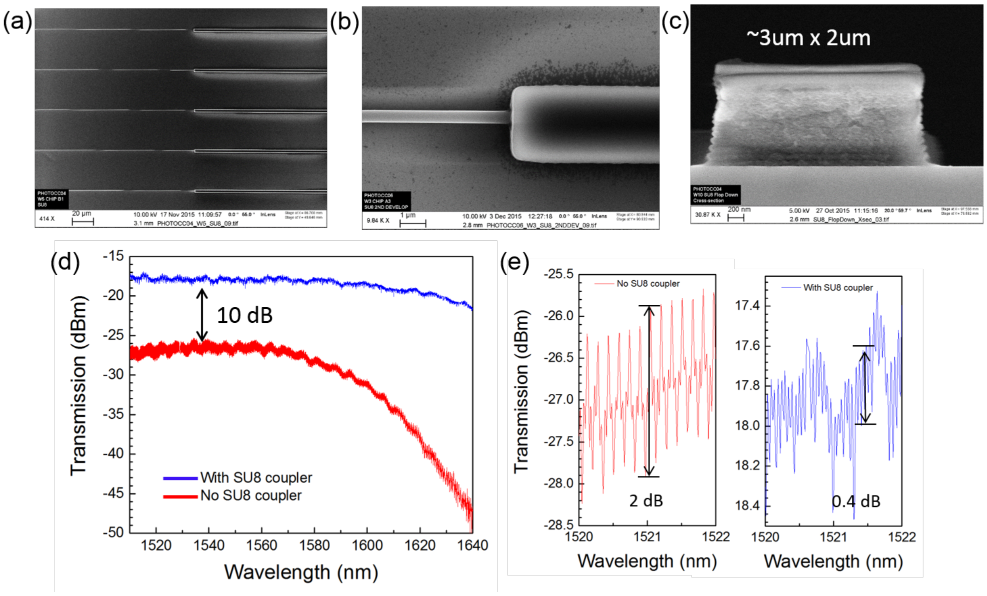

Figure 5.22 SU8 couplers and the coupling improvement. (a) Top down SEM image of SU8 coupler aligned with Si waveguide. (b) Zoom in image of single SU8 coupler. (c) Cross section of SU8 coupler. (d, e) Comparison of waveguide transmission with and without SU8 coupler. Coupling efficiency increased 10 dB and back reflection is also reduced from 2 dB to 0.4 dB.

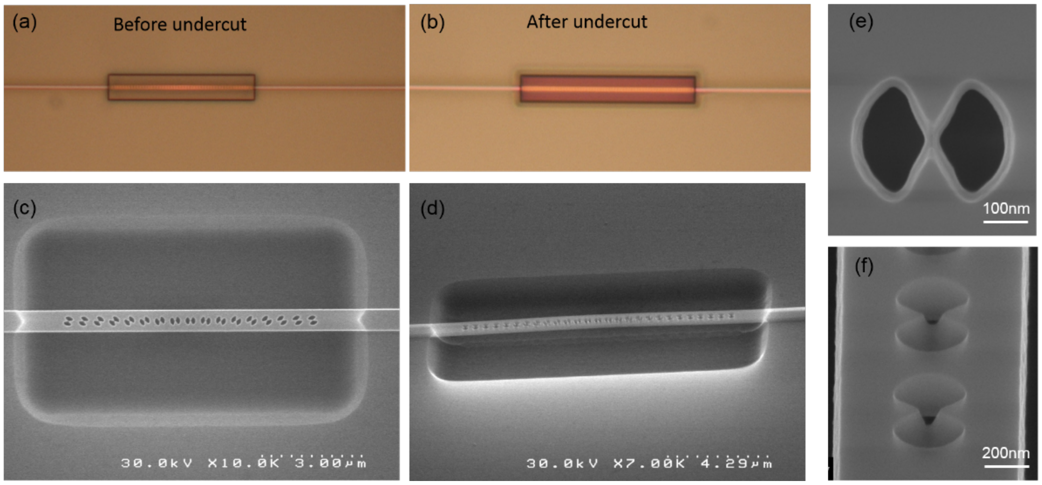

Figure 5.23 Optical and SEM images of bowtie PhC devices after wet etch. Optical microscope images of bowtie PhC devices (a) before and (b) after undercut process. (c) Top down and (d) tilted SEM images of bowtie PhC cavity after undercut. (e) Zoom in of top down image of single unit cell. (f) Zoom in of tilted image.

5.8 Experimental Measurements and Analysis

5.8.1 Tradeoff between transmission and Q factors

The experimentally measured Q_{total} is a combination of the intrinsic Q_i of the cavity and coupling Q_c, following the relation:

$$\frac{1}{Q_{total}} = \frac{1}{Q_i} + \frac{1}{Q_c} \tag{5.4}$$

Intrinsic Q_i is usually determined by the fabrication conditions, such as side wall roughness, uniformity of the unit cells and other fabrication imperfections. Coupling Q_c characterize the coupling strength between waveguide and resonator. As described by $T=(Q_{total}/Q_c)^2$, there is a general tradeoff between Q_c and transmission T [20]. High confinement between the waveguide and resonator results in a high Q-factor, but decreased transmission.

5.8.2 Measurements of bowtie PhCs with rotational design

Figure 5.24 shows the fabricated rotational designed bowtie PhC cavity described in Section 5.3.1. The PhC is designed to have in-line coupling (also called "end coupling" or "butt coupling") between the bus waveguide (*i.e.* ridge waveguide with no air holes) and PhC. For this coupling configuration, the photons at resonance frequencies have to tunnel through the mirror segments to enter the cavity. Therefore, the coupling coefficient between waveguide and cavity is decided by the mirror strength. The total mirror strength can be controlled by two design parameters: the mirror strength of each single mirror unit cell and the number of mirror unit cells. Regarding the strength of each mirror unit cell, we refer to the mirror strength calculation discussed in Section 4.2 and first reproduce Equation 4.10 here for convenience:

$$\gamma = \sqrt{\frac{(\omega_2 - \omega_1)^2}{(\omega_2 + \omega_1)^2} - \frac{(\omega_{res} - \omega_0)^2}{{\omega_0}^2}} \tag{5.5}$$

where ω_2, ω_1 and ω_0 are the air band edge, dielectric band edge, and midgap frequency of each segment, respectively, and ω_{res} is the cavity resonance. Equation 5.5 can then be rewritten as:

$$\gamma = \sqrt{\frac{(\omega_{gap}/2)^2 - (\Delta\omega)^2}{(\omega_0)^2}} \tag{5.6}$$

where $\omega_{gap} = \omega_2 - \omega_1$ is the band gap size. $\omega_0 = (\omega_2 + \omega_1)/2$ is the center frequency of the photonic band gap. $\Delta\omega = \omega_{res} - \omega_0$ is the difference between midgap and resonance frequency.

Two key parameters for mirror strength are identified from Equation 5.6: the size of the photonic band gap, and the distance of the resonance to midgap frequency. Mirror strength is the strongest when 1) the size of band gap is maximized; and 2) the resonance frequency is placed in the middle of the band gap.

Referring to Figure 5.7, Equation 5.6 indicates that the mirror strength of the R0 unit cell should be strongest since it has the largest bandgap. The confinement strength of each individual unit cell can therefore be continuously tuned by changing the rotational angle as resulting mirror strength of the unit cell. As shown in Figure 5.25, both decreasing the angle of mirror unit cell toward the R0 condition and adding additional mirror units improve the confinement (*Q*) but decrease the transmission of the PhC. Among the devices shown in the figure, the PhC with rotational angle 18° as the mirror unit cell and no additional mirror unit cells has the highest transmission intensity for the fundamental resonance, but the weakest mirror strength, which leads to the lowest Q-factor. The device designed to have the strongest cavity confinement (0° rotational angle mirror unit cells and 3 additional mirrors) did not show clear resonances in the transmission spectrum due to the low transmission intensity. Similar tradeoff is observed in hole size modulated cavities as well. We note that the measured resonances are close to the air band edge, unlike the case for traditional photonic crystal resonators that are designed to support dielectric modes. This is consistent with our design approach in which the air band mode of the R90 unit cell falls deep within the bandgap of the R0 unit cell (Figure 5.7).

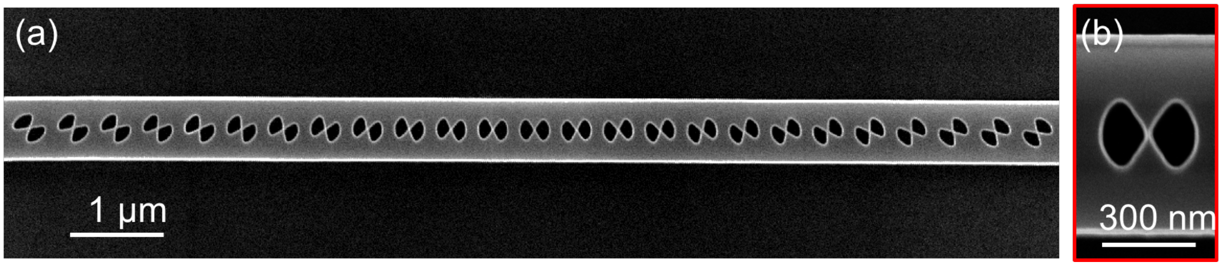

Figure 5.24 SEM image of a rotational designed cavity.

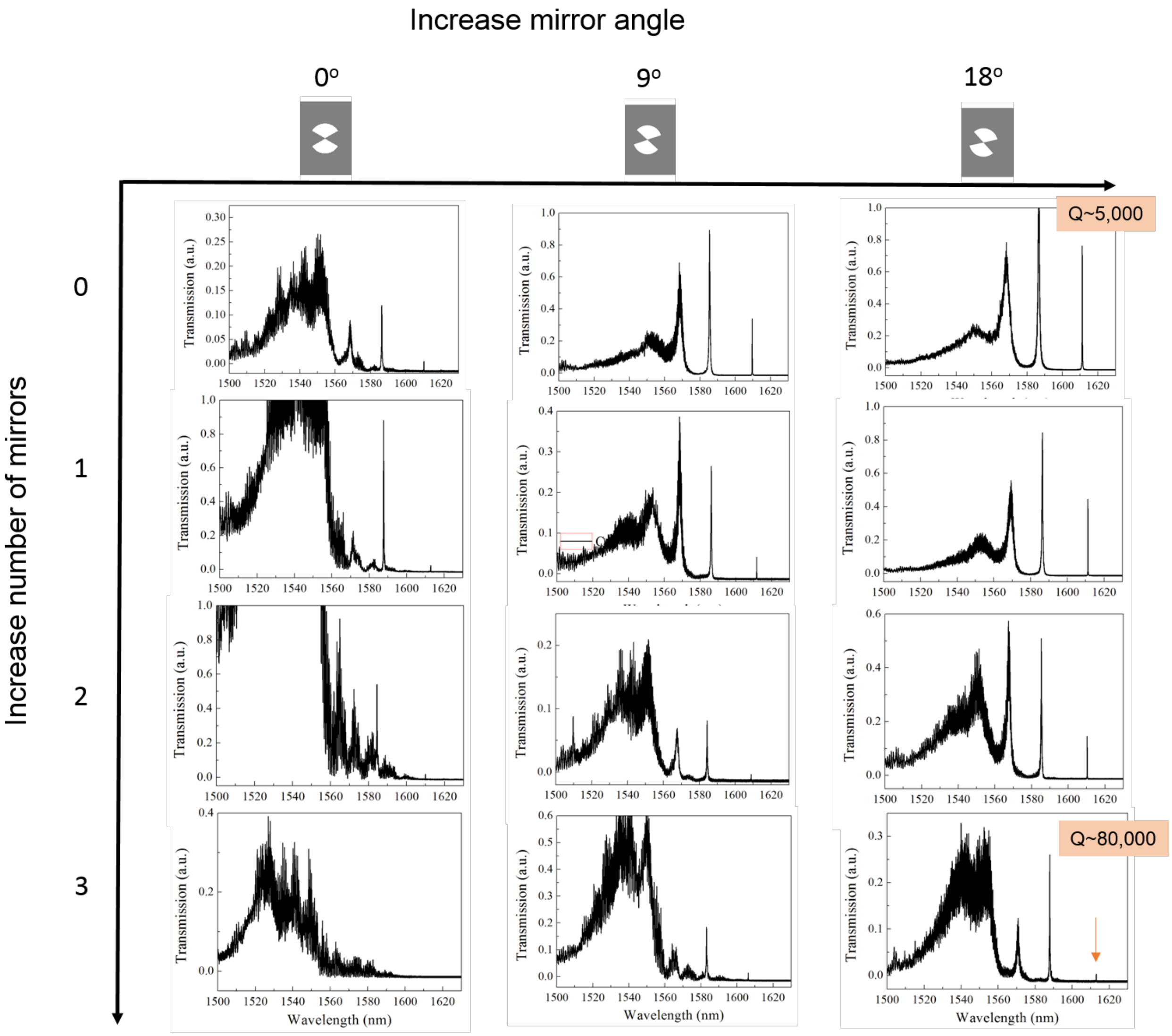

Figure 5.25 Tradeoff of Q-factor and transmission of rotationally designed bowtie PhC cavity

5.8.3 Measurements of bowtie PhCs with radius modulated design

Figure 5.26 shows the measurements of a radius modulated PhC cavity with 20 taper and 10 additional mirror unit cells. The radii of the center cavity and mirror unit cells are 150 and 187 nm, respectively. Figure 5.26b shows a zoomed in image of the unit cell highlighted in the red box in (a). The tilted SEM image in Figure 5.26c shows the V-groove in the *z*-direction. Transmission measurement reveals a Q-factor of 1×10^5 for the fundamental mode at 1578.85 nm, as shown in Figure 5.26d. Assuming the band edge has unity transmission, the normalized peak transmission is only ~ 0.0378. Although higher Q-factors may be supported in devices with more mirror unit cells, these devices have even lower transmission intensity and the poor signal-to-noise ratio precludes identification of clear resonance peaks.

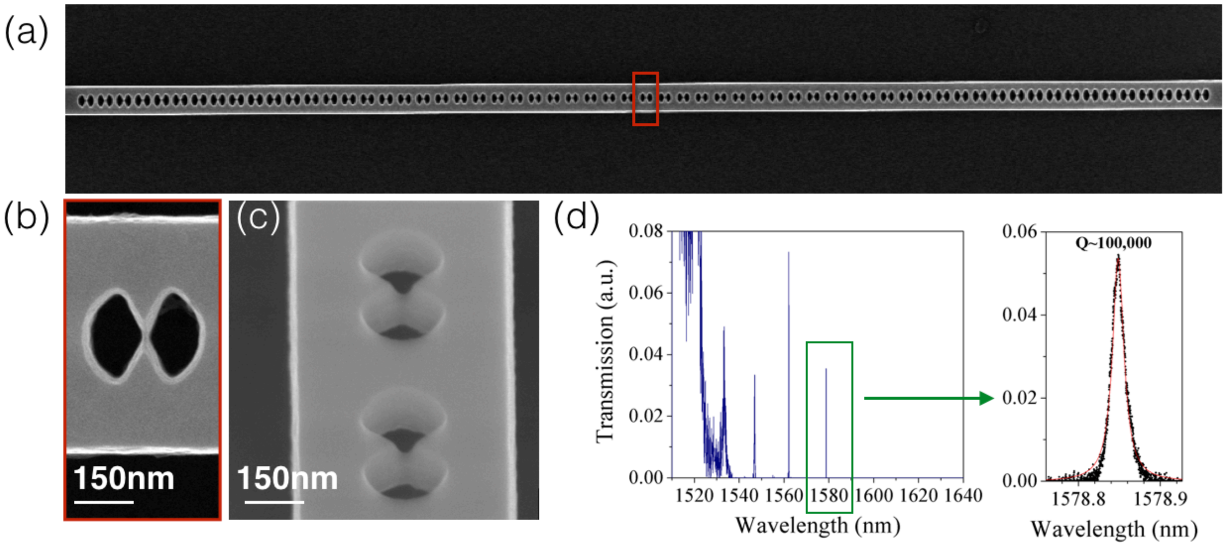

Figure 5.26 Transmission of designed bowtie photonic crystal with radius modulation. (a) SEM image of the fabricated device. (b) Zoomed in image of the single unit cell highlighted in the red box in (a). (c) Tilted SEM image showing the V-groove in the *z*-direction. (d) Experimental measurement of the transmission spectrum. The fundamental mode shows Q ~ 100,000.

5.8.4 Design of bowtie PhCs based on other degrees of freedom

The cavity is designed by linearly changing the connection width from 60 nm to 0 nm over several taper units. Figure 5.30 shows SEM images of a fabricated device. The width of the 1D PhC nanobeam is 700 nm, diameters of air holes are 300 nm, the period is 450 nm and the cavity is constructed with 20 tapers and 5 mirrors. Transmission of devices both with and without undercut are measured and compared in Figure 5.28. The undercut device shows a lower Q-factor (30,000) compared to the device that remains supported on the SOI wafer (50,000). Although not predicted in simulations, this reduced Q-factor is very likely due to surface roughness that was introduced during a wet etch undercutting process that was not performed under optimized conditions.

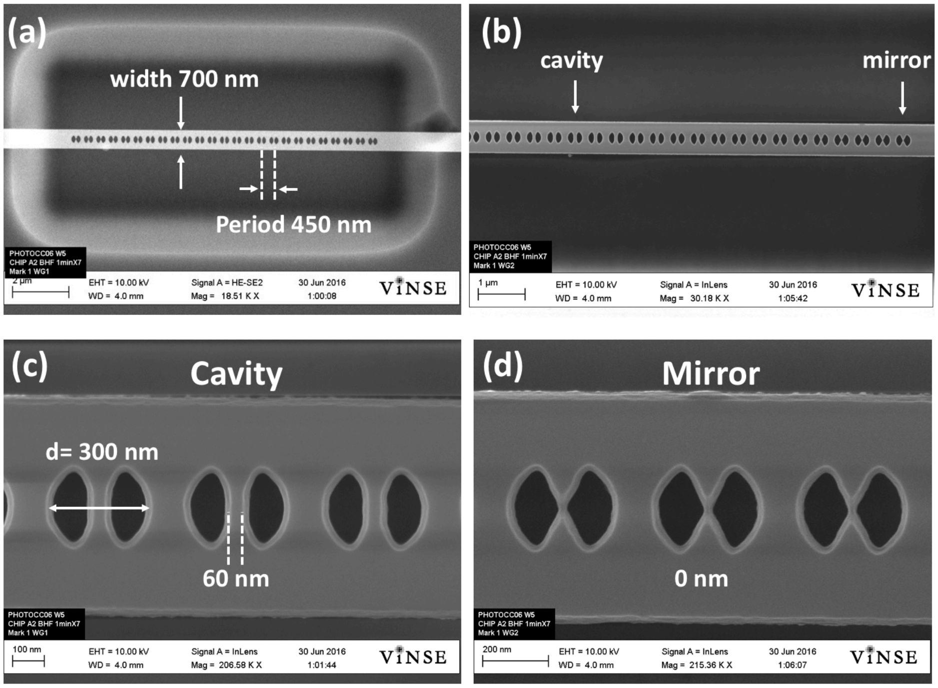

Figure 5.27 SEM images of a fabricated connection-width modulated bowtie PhC cavity. The width of the beam is 700 nm, diameters of air holes are 300 nm and the period is 450 nm. The connection width of the cavity center unit cell is 60 nm and 0 for the mirrors.

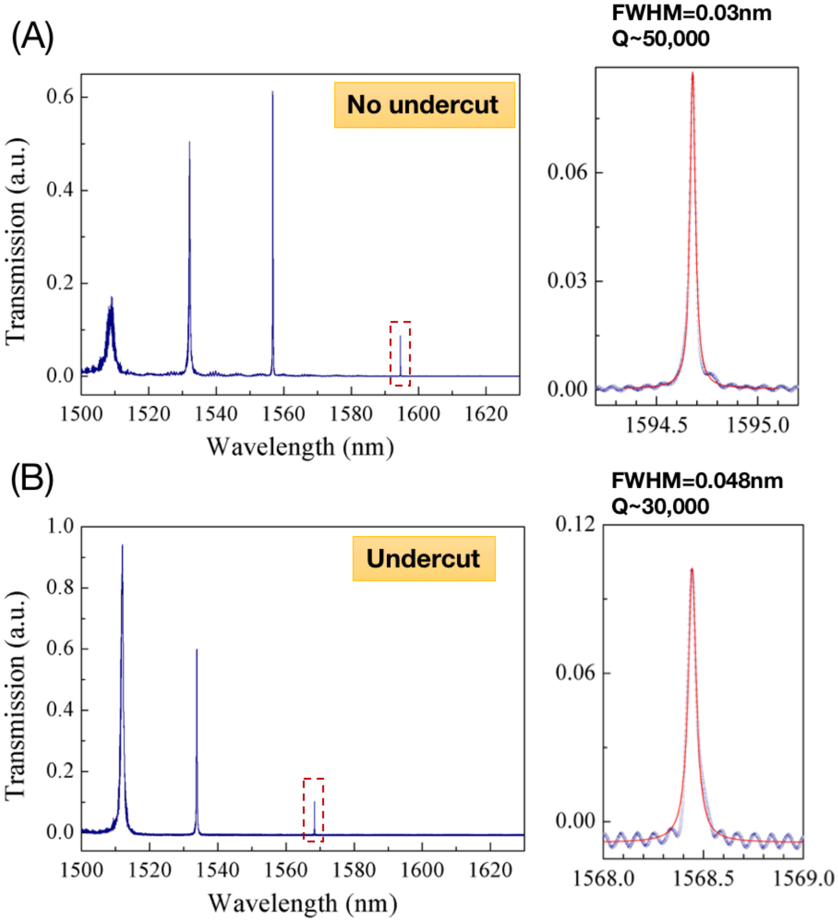

Figure 5.28 Transmission of bowtie PhC cavities designed by connection width modulation, without (A) and with (B) undercut. The inserts show the zoomed in view of the fundemental resonance mode in the red box.

5.9 Near-field scanning optical microscope (NSOM) measurement

To experimentally verify the mode distribution in the bowtie PhC cavity, NSOM measurements were carried out. The NSOM data was collected at the Laboratory of Nanotechnology, Instrumentation and Optics at University of Technology of Troyes. The NSOM setup is shown in Figure 5.29 and complete specifications of the setup can be found in Ref.[110]. General information about NSOM measurements can be found in Ref.[111].

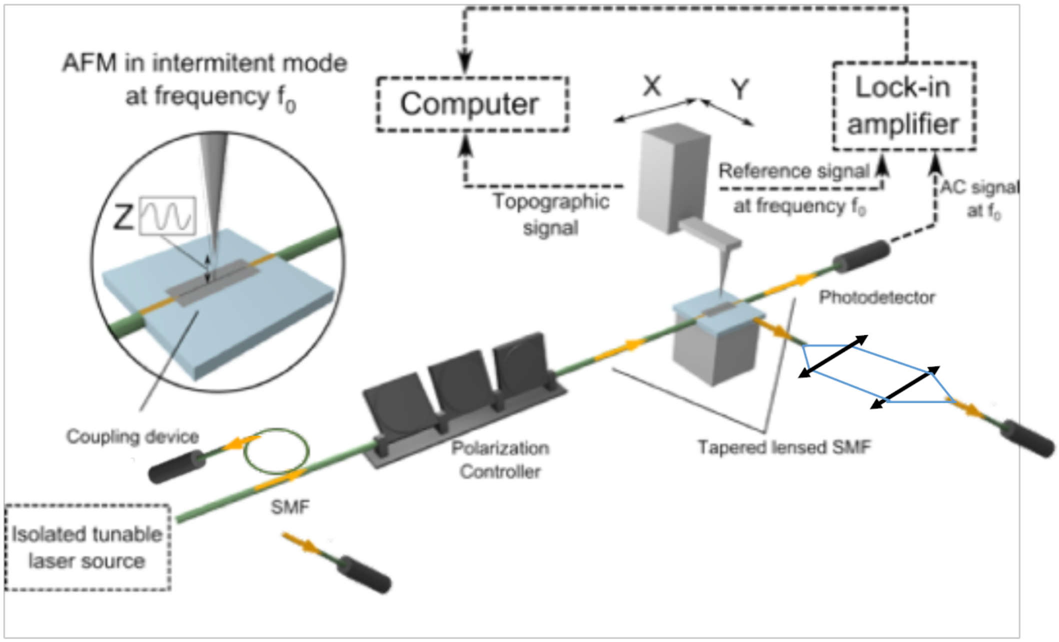

Figure 5.29 NSOM setup (Figure courtesy of R. Salas-Montiel)

Considering the practical constraints of the NSOM system, the high Q-factor device, (*e.g.*, the one shown in Figure 5.26), is not ideal for NSOM measurement due to the narrow resonance bandwidth (~ 15 pm) and low transmission. Instead, a device is designed with reduced mirror confinement (5 mirror unit cells) to increase both the full-width-at-half-maximum (~ 50 pm) and transmission intensity (~ 0.2) of the fundamental resonance. The SEM and transmission of this device is shown in Figure 5.30. Although the Q-factor is reduced compared to the device with more mirror unit cells, Figure 5.10 suggests that the mode volume of the two cavities should be similar. Hence, NSOM measurements on the device shown in Figure 5.30 can demonstrate the critical conceptual advance in this work – supporting a deep subwavelength mode in a dielectric resonator – and, moreover, the NSOM results on this particular device with reduced number of mirror units can be directly translated to the higher *Q* cavities with additional mirror unit cells.

All the simulated mode profiles shown earlier in this chapter are all collected at the center *z*-position within the PhC. Because the NSOM operates in tapping mode, oscillating between 0 and 30 nm above the silicon surface, we also carried out a simulation of the mode profile 16 nm above the silicon surface as an estimation of the average scattering field that should be detected by the NSOM (Figure 5.32a). This simulated mode profile shows an expanded mode size due to the divergence from the point-like profile in Figure 5.15e, which is the mode at the middle height of the silicon slab. Figure 5.31 shows the results from a series of simulations and reveals that the mode size linearly increases with distance from the silicon surface. At 16 nm above the silicon surface, the estimated mode size is ~ 62 nm. Figure 5.32b and c show the atomic force microscope (AFM) measured topology and corresponding near field mapping as measured by the NSOM, respectively. The optical mode is shown to be confined at the bowtie tip and agrees well with the simulated field profile in Figure 5.32a. Figure 5.32d and e show the NSOM measured profile along *x* and *y* slices. We identify the silicon region as the shaded area in Figure 5.32d and e, based on AFM measurements (purple dashed line in Figure 5.32d and e). The simulated electric energy profiles are shown by the blue curves in Figure 5.32d and e. The NSOM measured profile (red markers) along *y* slice through the center of the cavity unit cell shows a sharp peak of the optical field distribution at the bowtie center, indicating a concentrated optical field. The mode size is estimated by the full-width-at-half-maximum of the optical field in the bowtie tip region (the white gap in the silicon region in Figure 5.32d) and measured to be ~ 80 nm. This is in reasonable agreement with the corresponding FDTD simulations of the expected mode size near the surface where the NSOM measures the scattered field for a photonic crystal with $V_m \sim 6\times10^{-3}\ (\lambda/n_{si})^3$.

Slight discrepancies between the experimental and simulation curves likely arise from NSOM detection of the $\boldsymbol{E}_z$ signal, while our photonic crystal is designed for TE polarized light (mainly $\boldsymbol{E}_y$ component).

Different orders of PhC resonance are also measured by the NSOM, as shown in Figure 5.33. As mentioned previously, since the bowtie PhC cavity is designed based on an air mode, the optical band edge is at a shorter wavelength than the resonances, as shown in Figure 5.33a. The 1st order resonance is the one at the longest wavelength and is most deeply confined within the band gap. The 1st order resonance is an odd mode with maximum optical field intensity at the center of the cavity and gradually decaying intensity into the mirrors on both sides of the cavity. The 2nd order resonance is an even mode, which has two maxima of the optical field on either side of the cavity and the minimum optical field intensity is in the cavity center. The 3rd order resonance is another odd mode but with three maximum points of the optical field. Figure 5.33b and c show the simulated mode profiles and NSOM mappings at corresponding wavelengths.

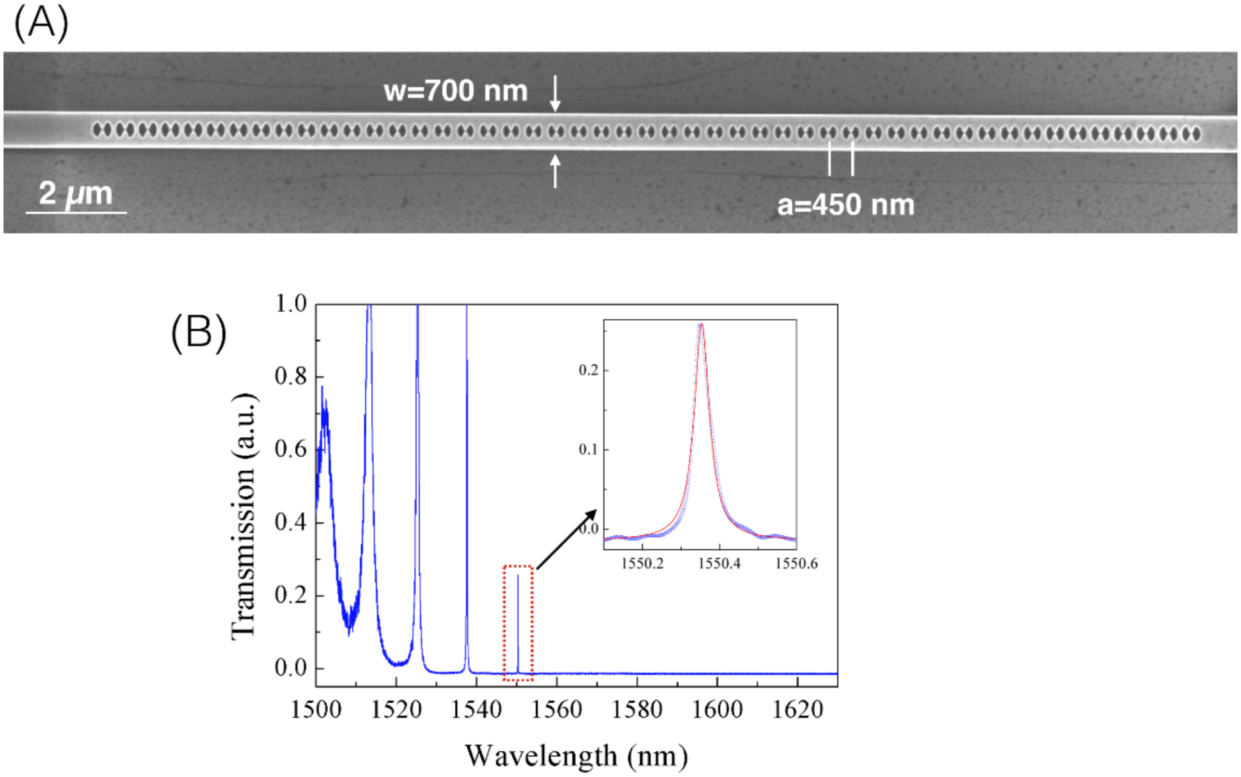

Figure 5.30 SEM image and transmission of the bowtie PhC characterized by a NSOM. (A) SEM image. The device has 5 mirror unit cells. The width of the nanobeam is measured to be 700 nm and the period is 450 nm. (B) Transmission of the device. The Q factor is 30,000, making this device easier to measure with NSOM.

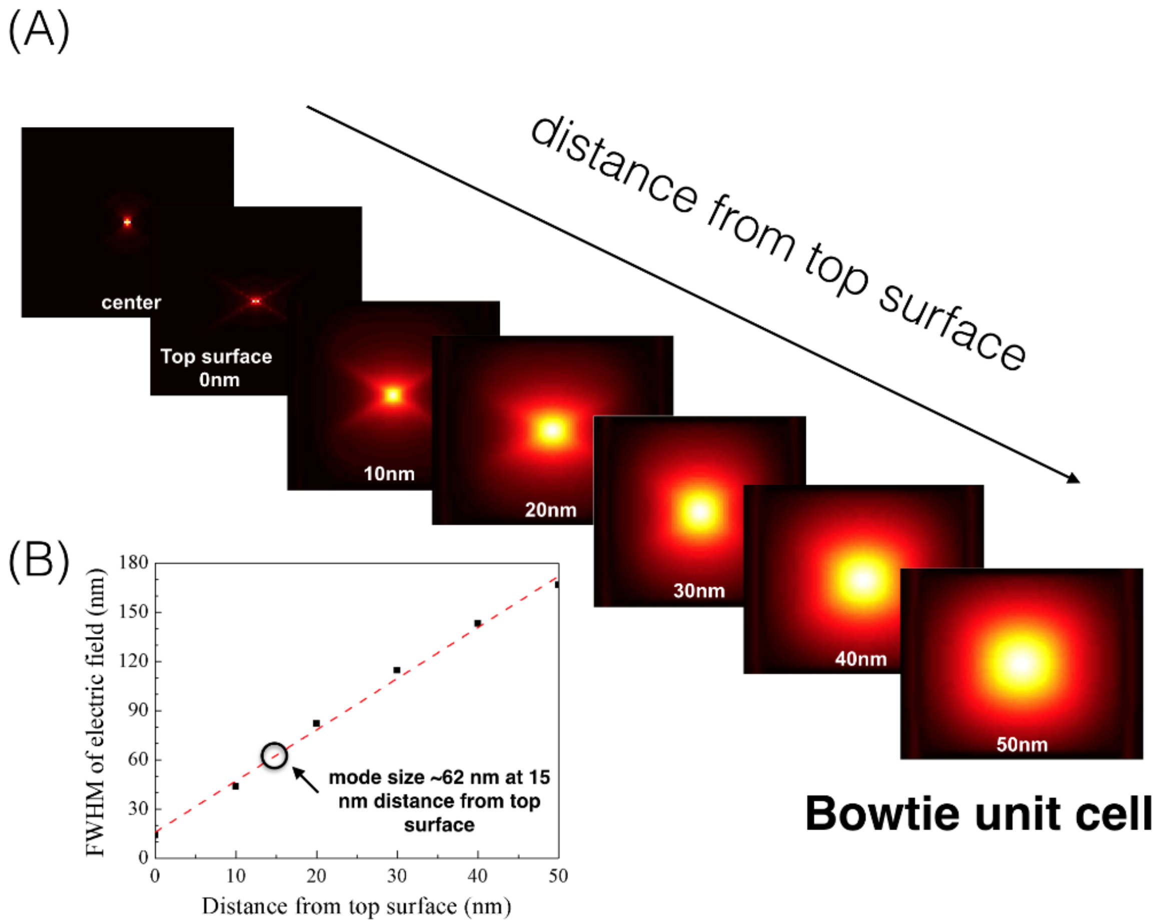

Figure 5.31 The divergence of the bowtie mode as the detection plane moves away from top surface of the device. (A) A series of mode profiles at different distances from the top surface. (B) The mode size is extracted as the full-width-at-half-maximum of the electric energy profile. The plot shows the size linearly increase with the distance away from silicon surface. The circle in the plot indicates the average distance where NSOM measures the electric field. The mode size is estimated to be around 62 nm.

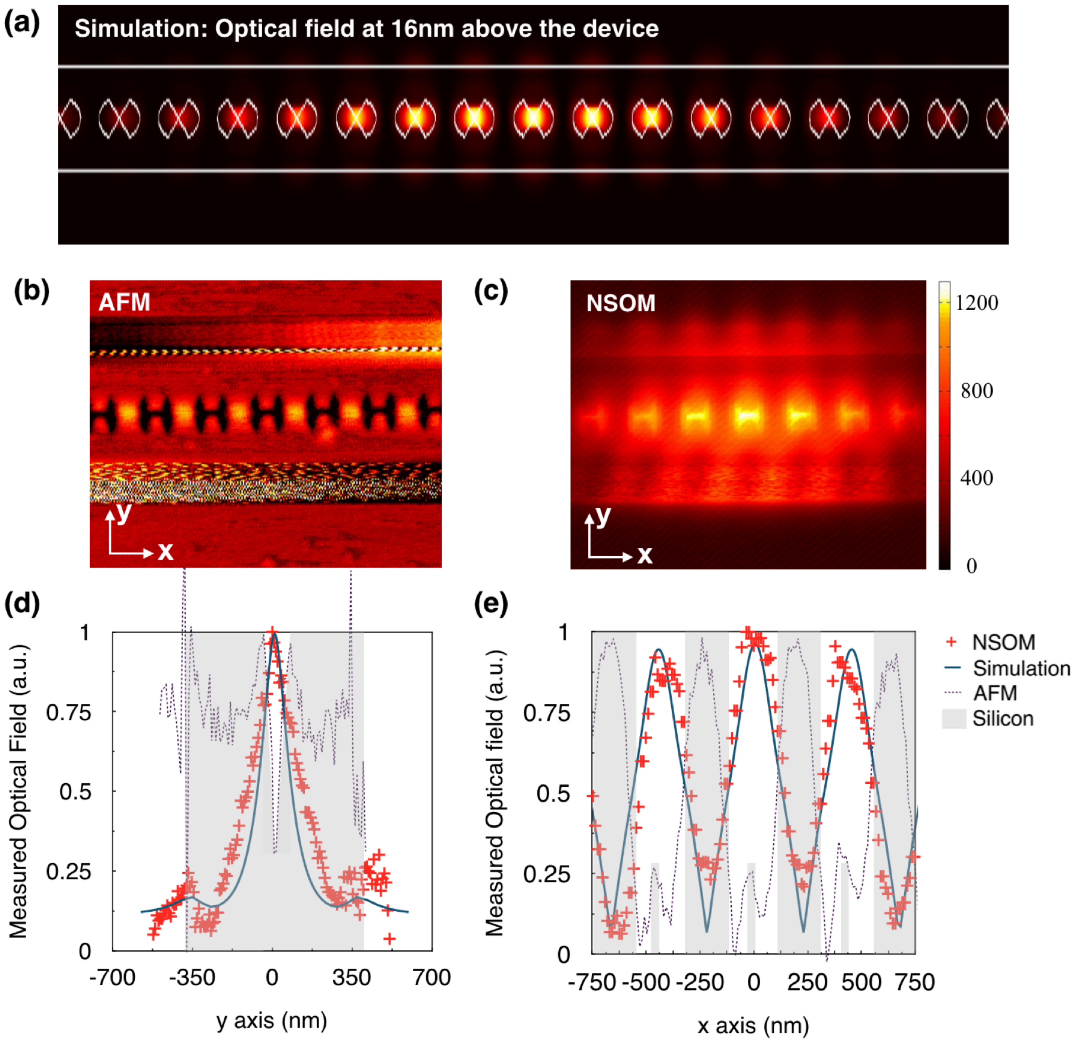

Figure 5.32 Analysis of mode size through NSOM measurements. (a) Simulated mode profile near the surface where the NSOM measures the scattered field (16 nm above silicon surface). (b) and (c) AFM measurement and corresponding optical field mapping obtained using the NSOM. (d) and (e) NSOM measured profile along vertical (*y*-axis) and horizontal (*x*-axis) slices, respectively.

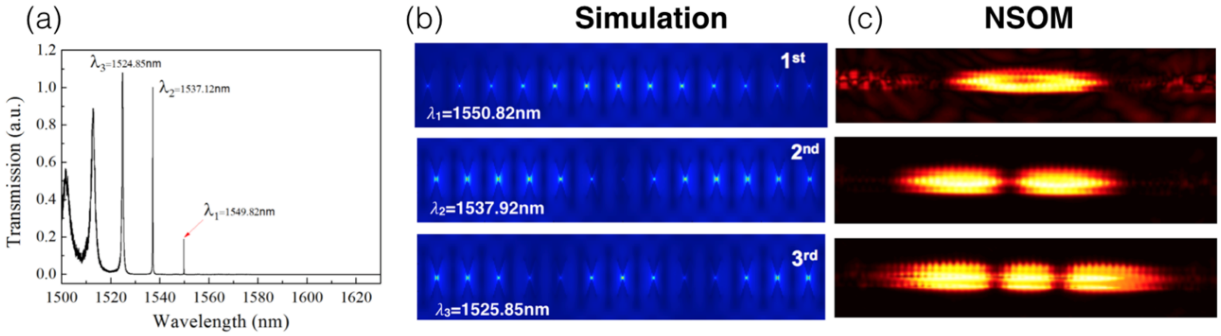

Figure 5.33 Measured near-field of different order resonances. (a) Transmission spectrum of the bowtie PhC. (b) Simulated optical field at different wavelengths corresponding to different order resonances. (c) NSOM mapping of the corresponding optical modes.

5.10 Conclusion

As confirmed by both theoretical analysis and experimental data, we demonstrated that it is possible for dielectric cavities to simultaneously support a deep subwavelength confined optical mode and maintain an ultra-high Q-factor. Using bowtie-shaped unit cells in a 1D PhC cavity, we demonstrate a mode volume as small as that of a plasmonic resonator ($V_m = 6 \times 10^{-4}$ μm^3) with temporal confinement as long as that of a dielectric resonant cavity ($Q \sim 6.5 \times 10^6$ simulated and 1×10^5 measured). We believe that the novel design method presented here, accompanied by experimental realization, is an important milestone that could inspire new photonic device designs that support record performances across a broad range of optical applications.

CHAPTER 6

CONCLUSIONS

6.1 Overview

In this work, the enhancement of light-matter interaction was investigated from three perspectives: increased external perturbation, increased overlap between the external perturbation and the optical field, and increased optical field strength. The enhanced sensitivity was demonstrated via design, theoretical analysis, numerical simulation, fabrication, and experimental characterization.

6.1.1 Amplifying the sensing signal through increased bioreceptor density

One commonly overlooked variable in the design of label-free optical biosensors is the bioreceptor density. As the size of nanophotonic sensors decreases, the active sensing region is also reduced and leaves few binding sites for bioreceptors. For this reason, although the optical field is concentrated, the detection sensitivity does not scale with the energy density. To overcome this, in Chapter 2, we considered the immobilization of bioreceptors in our design. For DNA detection, we compared two different immobilization methods: a traditional direct conjugation method and a novel in-situ synthesis method. Our results show that both sensitivity and response time scale with bioreceptor density and increases by 5 times when the in-situ synthesis method is used.

6.1.2 Increase the light-matter interaction through expanded modal overlap

In Chapter 3, we optimized the spatial overlap between the optical mode and the accessible near-surface dielectric environment by undercutting TM-mode micro-ring resonators to form suspended structures. The benefit of this design for biosensing is in two-fold. First, the bottom surface of the ring is opened for biomolecular access, therefore increasing the active sensing area. Second, by removing the substrate, the effective index of the TM waveguide is decreased, resulting in a more delocalized mode that has more interaction with surface-bound molecules. Our experimental data, supported by finite-difference time-domain simulations and mode analysis exhibits a two-fold enhanced optical detection sensitivity compared to traditional, supported TM-mode micro-ring resonator sensors. Highly sensitive detection of heat denatured Herceptin, an important breast cancer therapeutic, was demonstrated using suspended Si micro-ring resonators.

6.1.3 Design and fabrication of photonic resonators with high Q and low V_m

Chapter 4 and 5 were dedicated to a *de novo* PhC method. We provided a comprehensive review of a *de novo* PhC design method. By manipulating the unit cell, we demonstrated unprecedented control over the band structure. The addition of sub-wavelength photonic elements within the unit cells gives PhCs special functional properties (*e.g.,* deep sub-wavelength confinement) that otherwise would not be possessed in traditional PhC. We designed a bowtie shaped PhC unit cell that enabled the realization of high Q-factor and low mode volume PhC cavities in both FDTD simulation and experiments. The fabricated bowtie PhC cavities can be utilized as a platform for various strong light-matter interaction applications, including low detection limit sensing, optomechanics, optical trapping and enhanced fluorescence emission.

6.2 Future work

6.2.1 Side coupling design to improve measured transmission

Instead of in-line coupling between input waveguides and PhC cavities, a side-coupling configuration could be used. Figure 6.1 shows the SEM images of side-coupled bowtie PhC cavities. In these designs, the coupling waveguide width is tapered to 300 nm at the coupling point on the top of curved section of the waveguide. The bending radius of the coupling waveguide is r=10 µm. In the initial parameter sweep, the gap is varied from 100 to 300 nm at 50 nm increments. The 300 nm gap leads to the highest measured PhC Q-factor among these cavities, but we believe an even higher Q-factor can be achieved with further optimized coupling conditions.

Figure 6.2 shows the measured transmission spectrum of a side-coupled rotational designed bowtie PhC cavity. The cavity is designed with 18 taper units with linear tapering profile of rotational angle and 0 additional mirror units. The Q-factor of the device without undercut is relatively low (Figure 6.2a) and indicates an over-coupled condition. The undercut process removes the substrate oxide and increases the confinement of the mode. Therefore, the coupling strength is decreased and is closer to the critical coupling condition. Figure 6.2b shows an improved Q-factor (Q ~ 15,000) in the suspended device.

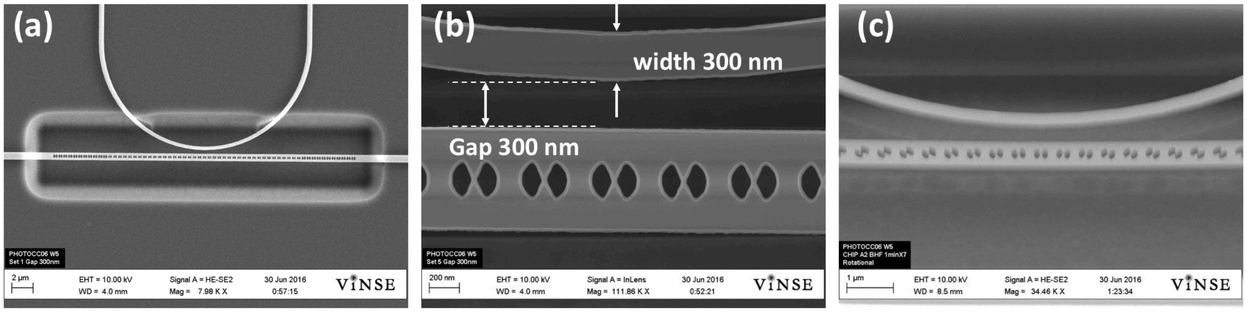

Figure 6.1 SEM images of side coupled bowtie PhC cavities.

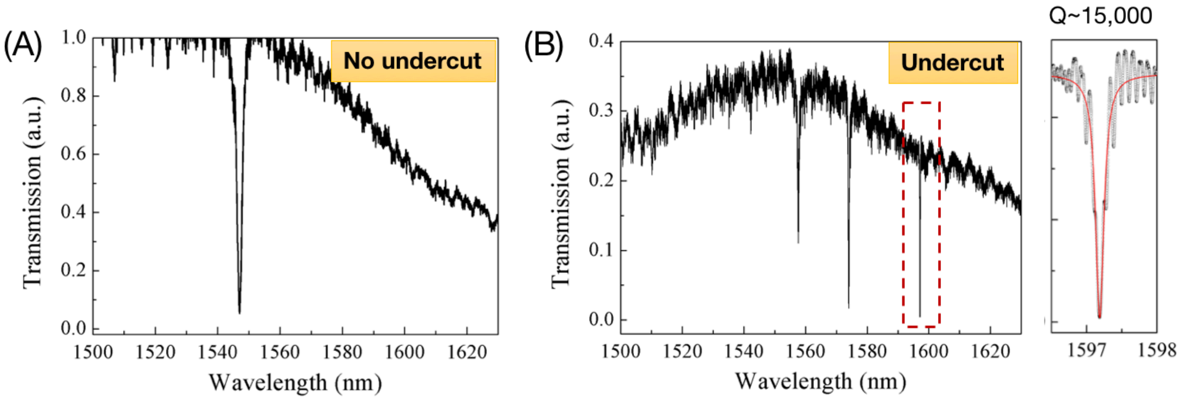

Figure 6.2 Tranmssion spectra of side-coupled rotational designed bowtie PhC cavity. (A) Measured spectrum without undercut. (B) Spectrum with undercut. Insert is the zoomed in image of the fundemental resonance marked in the red box.

In addition to the rotational bowtie PhC design, we also tested a novel design with side-coupling. In this new design, 39 unit cells with the same radius (*r*=150 nm) are designed as the cavity and 11 mirror unit cells with radii *r*=185 nm are added on both sides of the cavity region for confinement. Similar to the side-coupled rotational designed cavity, the coupling waveguide approaches the cavity center of this newly designed cavity with the same design as the side coupled rotational cavities. The design schematic and SEM image of the fabricated device are shown in Figure 6.3. Figure 6.4 shows the measured transmission of supported (A) and suspended devices (B). The Q-factor of the suspended device is measured to be ~ 120,000, suggesting that the side-coupling approach holds great promise as a measurement configuration for bowtie PhCs. Interestingly, although not using taper segments leads to large losses for in-line transmission measurements due to the modal mismatch between the mirror and cavity unit cells, the side-coupling approach mitigates this challenge by coupling directly into the center of the cavity region.

Further design analysis is needed for the cavity presented in Figure 6.3 and Figure 6.4 to achieve an optimal Q/V_m ratio.

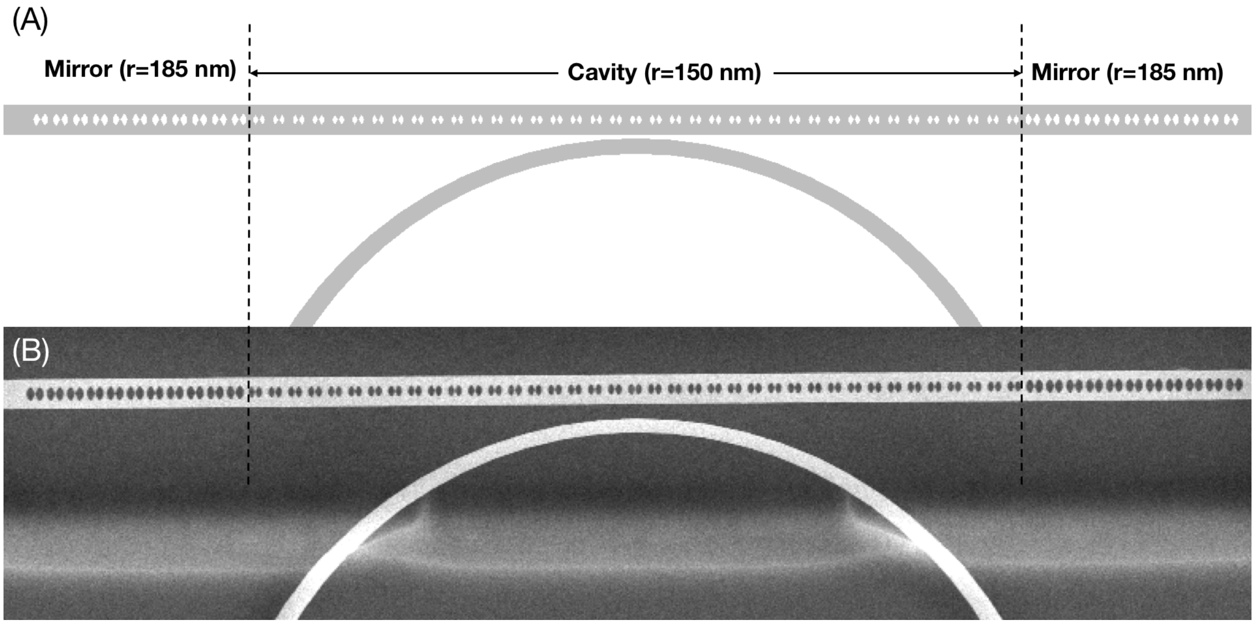

Figure 6.3 Design and SEM images of a side coupled bowtie PhC cavity with repeated identical unit cells as cavity.

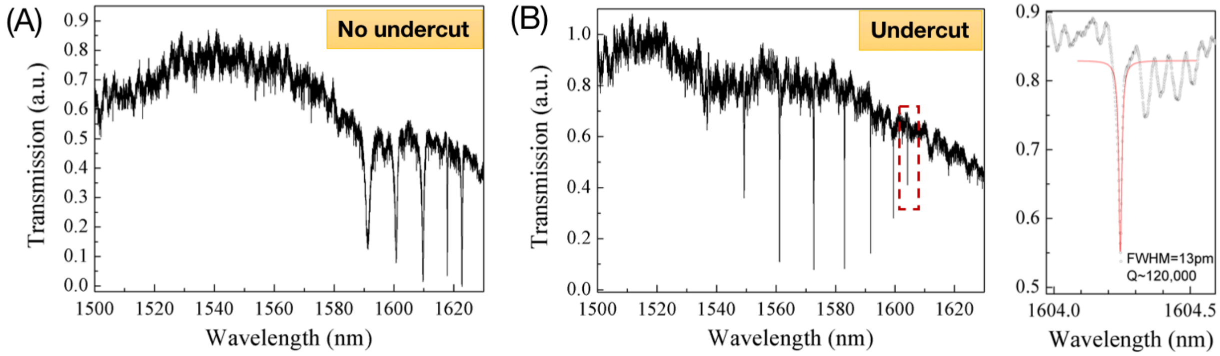

Figure 6.4 Measured transmissions of the side coupled bowtie PhC cavities with repeated identical unit cells as cavity.

6.2.2 Free space coupling: design of a guided bowtie PhC resonator

To this point, all photonic resonators discussed in this thesis are all based on waveguiding modes and cannot be efficiently coupled from free space. However, many applications require free space coupling, such as surface enhanced Raman spectrometry, photodetectors, solar cells, free space lasers and high harmonic generation. As discussed in Section 1.1.3 in Chapter 1, the 2D PhC only has an in-plane band gap. However, the Γ point in the PhC band diagram is very special because it represents an infinitely long spatial period in real space. This infinitely long spatial period means the mode is a standing wave (spatially invariant) and is only oscillating in time. In fact, light is capable of coupling into the 2D PhC slab from free space at the Γ point in the photonic band diagram, as shown in Figure 6.5 [112, 113]. The mode profiles at the on- and off-resonance frequencies are shown in Figure 6.6. Based on this idea, we can design a bowtie shaped unit cell in 2D PhC slab. Figure 6.7 shows the simulation of such a structure. From this initial simulation result, the electrical field strength at resonance frequency of the "bowtie mode" (Figure 6.7c) is 10 times higher than in PhCs with circular unit cells, suggesting that the 2D bowtie PhC may be advantageous for free space optics applications.

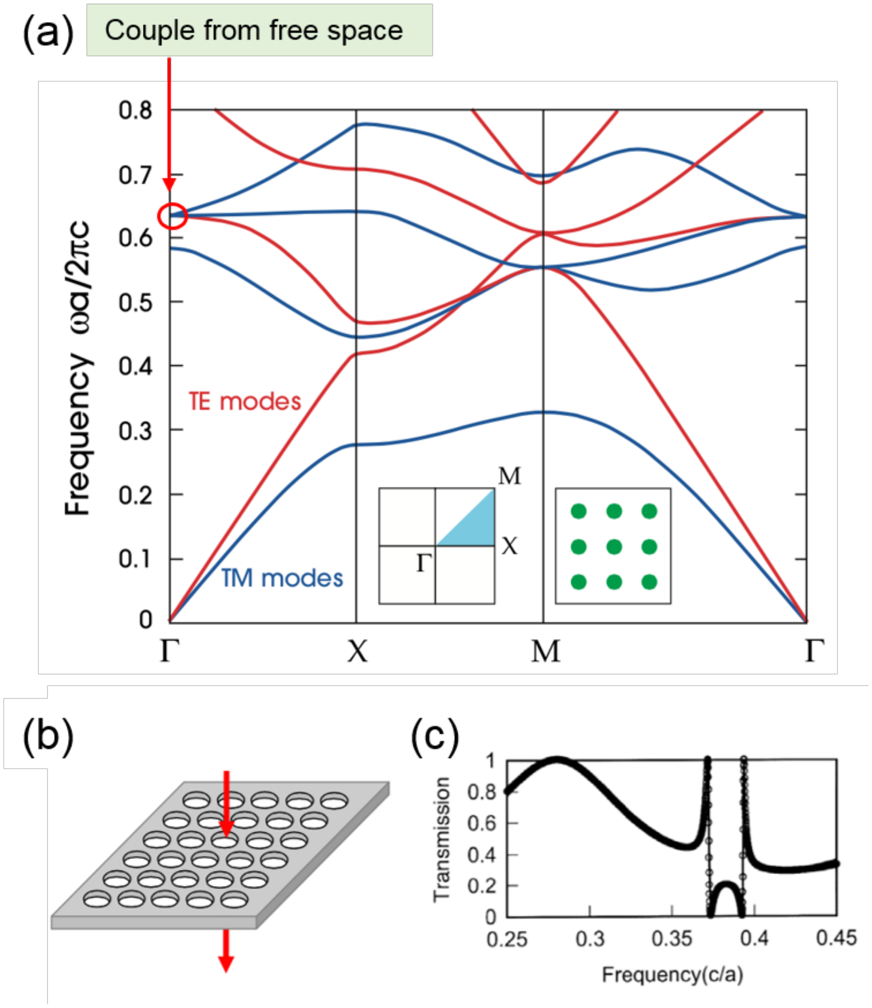

Figure 6.5 Guided PhC resonance. (a) Band diagram of a 2D slab PhC. Light is capable of coupling into the slab mode at the *Γ* point [31]. (b) Illustration of top coupling from free space into the PhC guided resonance. (c) The transmission spectrum is typically characterized by a Fano resonance [113]. Figures reproduced with permission from ©2014 Elsevier.

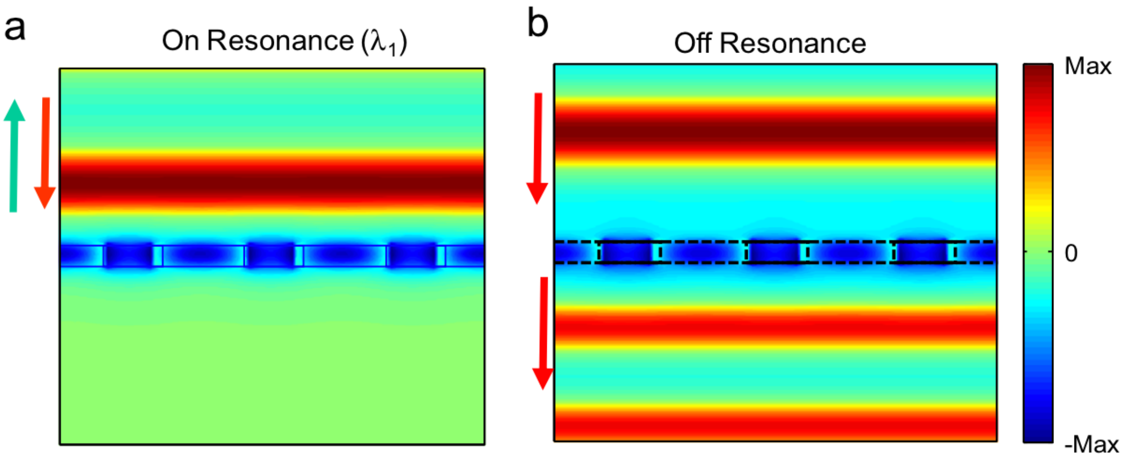

Figure 6.6 On- and off-resonance conditions of the guided resonance in a 2D PhC slab [113]. Figures reproduced with permission from ©2014 Elsevier.

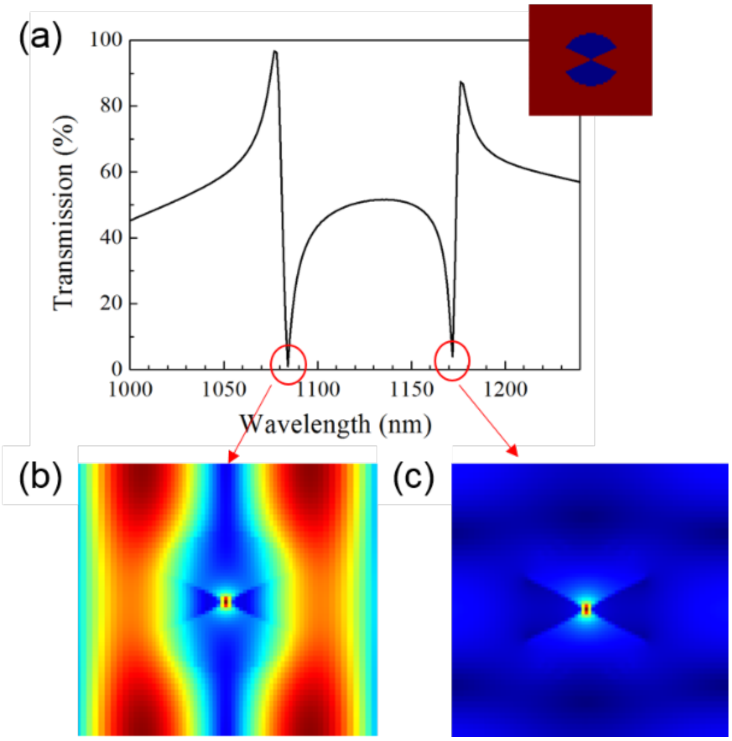

Figure 6.7 Simulation results of the 2D bowtie PhC slab coupled from free space. (a) Transmission spectrum. Insert shows the unit cell design. The period is chosen to be 440 nm × 440 nm and the radius is 80 nm. (b) Mode profile of the resonance at 1086 nm and (c) mode profile of the resonance at 1174 nm.

REFERENCES

1. Noda, S., M. Fujita, and T. Asano, *Spontaneous-emission control by photonic crystals and nanocavities.* Nat Photon, 2007. **1**(8): p. 449-458.

2. Oulton, R.F., et al., *Plasmon lasers at deep subwavelength scale.* Nature, 2009. **461**(7264): p. 629-632.

3. Matsuo, S., et al., *High-speed ultracompact buried heterostructure photonic-crystal laser with 13 fJ of energy consumed per bit transmitted.* Nature Photonics, 2010. **4**(9): p. 648-654.

4. Takahashi, Y., et al., *A micrometre-scale Raman silicon laser with a microwatt threshold.* Nature, 2013. **498**(7455): p. 470-474.

5. Atwater, H.A. and A. Polman, *Plasmonics for improved photovoltaic devices.* Nature Materials, 2010. **9**(3): p. 205-213.

6. Schuller, J.A., et al., *Plasmonics for extreme light concentration and manipulation.* Nature Materials, 2010. **9**(3): p. 193-204.

7. Brongersma, M.L., Y. Cui, and S.H. Fan, *Light management for photovoltaics using high-index nanostructures.* Nature Materials, 2014. **13**(5): p. 451-460.

8. Green, M.A. and S. Pillai, *Harnessing plasmonics for solar cells.* Nature Photonics, 2012. **6**(3): p. 130-132.

9. Xu, Q.F., et al., *Micrometre-scale silicon electro-optic modulator.* Nature, 2005. **435**(7040): p. 325-327.

10. Reed, G.T., et al., *Silicon optical modulators.* Nature Photonics, 2010. **4**(8): p. 518-526.

11. Nozaki, K., et al., *Sub-femtojoule all-optical switching using a photonic-crystal nanocavity.* Nature Photonics, 2010. **4**(7): p. 477-483.

12. Melikyan, A., et al., *High-speed plasmonic phase modulators.* Nature Photonics, 2014. **8**(3): p. 229-233.

13. Kim, S., et al., *High-harmonic generation by resonant plasmon field enhancement.* Nature, 2008. **453**(7196): p. 757-760.

14. Nozaki, K., et al., *Ultralow-power all-optical RAM based on nanocavities.* Nature Photonics, 2012. **6**(4): p. 248-252.

15. Eichenfield, M., et al., *Optomechanical crystals.* Nature, 2009. **462**(7269): p. 78-82.

16. Brolo, A.G., *Plasmonics for future biosensors.* Nature Photonics, 2012. **6**(11): p. 709-713.

17. Chakravarty, S., et al., *Multiplexed specific label-free detection of NCI-H358 lung cancer cell line lysates with silicon based photonic crystal microcavity biosensors.* Biosensors & Bioelectronics, 2013. **43**: p. 50-55.

18. Hu, S., et al., *Enhancing the Sensitivity of Label-Free Silicon Photonic Biosensors through Increased Probe Molecule Density.* ACS Photonics, 2014. **1**(7): p. 590-597.

19. Quan, Q., P.B. Deotare, and M. Loncar, *Photonic crystal nanobeam cavity strongly coupled to the feeding waveguide.* Applied Physics Letters, 2010. **96**(20): p. 203102.

20. Ryckman, J.D. and S.M. Weiss, *Low mode volume slotted photonic crystal single nanobeam cavity.* Applied Physics Letters, 2012. **101**(7): p. 071104.

21. Notomi, M., E. Kuramochi, and H. Taniyama, *Ultrahigh-Q nanocavity with 1D photonic gap.* Opt Express, 2008. **16**(15): p. 11095-102.

22. Kollmann, H., et al., *Toward Plasmonics with Nanometer Precision: Nonlinear Optics of Helium-Ion Milled Gold Nanoantennas.* Nano Letters, 2014. **14**(8): p. 4778-4784.

23. Lee, H., et al., *Chemically etched ultrahigh-Q wedge-resonator on a silicon chip.* Nature Photonics, 2012. **6**(6): p. 369-373.

24. LiangD, et al., *Integrated finely tunable microring laser on silicon.* Nat Photon, 2016. **10**(11): p. 719-722.

25. Fan, X.D., et al., *Sensitive optical biosensors for unlabeled targets: A review.* Analytica Chimica Acta, 2008. **620**(1-2): p. 8-26.

26. Rosenberg, J.C., et al., *A 25 Gbps silicon microring modulator based on an interleaved junction.* Opt Express, 2012. **20**(24): p. 26411-23.

27. Aspelmeyer, M., T.J. Kippenberg, and F. Marquard, *Cavity optomechanics.* Reviews of Modern Physics, 2014. **86**(4): p. 1391-1452.

28. Khurgin, J.B., *How to deal with the loss in plasmonics and metamaterials.* Nature Nanotechnology, 2015. **10**(1): p. 2-6.

29. Koenderink, A.F., A. Alù, and A. Polman, *Nanophotonics: Shrinking light-based technology.* Science, 2015.

30. Boltasseva, A. and H.A. Atwater, *Low-Loss Plasmonic Metamaterials.* Science, 2011. **331**(6015): p. 290-291.

31. Joannopoulos, J.D., Johnson, S.G., Winn, J.N., Meade, R.D., *Photonic Crystals: Molding the Flow of Light (Second Edition).* 2008: Princeton University Press. 304.

32. Settle, M., et al., *Low loss silicon on insulator photonic crystal waveguides made by 193nm optical lithography.* Optics Express, 2006. **14**(6): p. 2440-2445.

33. Quan, F.L., et al., *Scalable photonic crystal chips for high sensitivity protein detection.* Optics Express, 2013. **21**(26): p. 32306-32312.

34. Iqbal, M., et al., *Label-Free Biosensor Arrays Based on Silicon Ring Resonators and High-Speed Optical Scanning Instrumentation.* Ieee Journal of Selected Topics in Quantum Electronics, 2010. **16**(3): p. 654-661.

35. Gervais, L., N. de Rooij, and E. Delamarche, *Microfluidic Chips for Point-of-Care Immunodiagnostics.* Advanced Materials, 2011. **23**(24): p. H151-H176.

36. Lequin, R.M., *Enzyme immunoassay (EIA)/enzyme-linked immunosorbent assay (ELISA).* Clin Chem, 2005. **51**(12): p. 2415-8.

37. Weiss, S.M., G. Rong, and J.L. Lawrie, *Current status and outlook for silicon-based optical biosensors.* Physica E: Low-dimensional Systems and Nanostructures, 2009. **41**(6): p. 1071-1075.

38. Qavi, A.J., et al., *Anti-DNA:RNA Antibodies and Silicon Photonic Microring Resonators: Increased Sensitivity for Multiplexed microRNA Detection.* Analytical Chemistry, 2011. **83**(15): p. 5949-5956.

39. Qavi, A.J., T.M. Mysz, and R.C. Bailey, *Isothermal Discrimination of Single-Nucleotide Polymorphisms via Real-Time Kinetic Desorption and Label-Free Detection of DNA Using Silicon Photonic Microring Resonator Arrays.* Analytical Chemistry, 2011. **83**(17): p. 6827-6833.

40. Niehusmann, J., et al., *Ultrahigh-quality-factor silicon-on-insulator microring resonator.* Opt Lett, 2004. **29**(24): p. 2861-3.

41. Xia, F.N., L. Sekaric, and Y. Vlasov, *Ultracompact optical buffers on a silicon chip.* Nature Photonics, 2007. **1**(1): p. 65-71.

42. Xu, Q., D. Fattal, and R.G. Beausoleil, *Silicon microring resonators with 1.5 μm radius.* Opt Express, 2008. **16**(6): p. 4309-15.

43. Akahane, Y., et al., *High-Q photonic nanocavity in a two-dimensional photonic crystal.* Nature, 2003. **425**(6961): p. 944-947.

44. Quan, Q.M., P.B. Deotare, and M. Loncar, *Photonic crystal nanobeam cavity strongly coupled to the feeding waveguide.* Applied Physics Letters, 2010. **96**(20).

45. Song, B.S., et al., *Ultra-high-Q photonic double-heterostructure nanocavity.* Nature Materials, 2005. **4**(3): p. 207-210.

46. Lee, M. and P.M. Fauchet, *Two-dimensional silicon photonic crystal based biosensing platform for protein detection.* Optics Express, 2007. **15**(8): p. 4530-4535.

47. Xu, D.X., et al., *Label-free biosensor array based on silicon-on-insulator ring resonators addressed using a WDM approach.* Optics Letters, 2010. **35**(16): p. 2771-2773.

48. McClellan, M.S., L.L. Domier, and R.C. Bailey, *Label-free virus detection using silicon photonic microring resonators.* Biosensors & Bioelectronics, 2012. **31**(1): p. 388-392.

49. Byeon, J.Y. and R.C. Bailey, *Multiplexed evaluation of capture agent binding kinetics using arrays of silicon photonic microring resonators.* Analyst, 2011. **136**(17): p. 3430-3433.

50. Kang, C. and S.M. Weiss, *Photonic crystal with multiple-hole defect for sensor applications.* Optics Express, 2008. **16**(22): p. 18188-18193.

51. Kang, C., et al., *Photonic crystal slab sensor with enhanced surface area.* Optics Express, 2010. **18**(26): p. 27930-27937.

52. Pal, S., et al., *Silicon photonic crystal nanocavity-coupled waveguides for error-corrected optical biosensing.* Biosensors & Bioelectronics, 2011. **26**(10): p. 4024-4031.

53. Chakravarty, S., et al., *Slow light engineering for high Q high sensitivity photonic crystal microcavity biosensors in silicon.* Biosensors & Bioelectronics, 2012. **38**(1): p. 170-176.

54. Kang, C., et al., *Optimized light-matter interaction and defect hole placement in photonic crystal cavity sensors.* Opt Lett, 2012. **37**(14): p. 2850-2.

55. Lai, W.-C., et al., *Multiplexed detection of xylene and trichloroethylene in water by photonic crystal absorption spectroscopy.* Optics Letters, 2013. **38**(19): p. 3799-3802.

56. Huizenga, D.E. and J.W. Szostak, *A DNA Aptamer That Binds Adenosine and Atp.* Biochemistry, 1995. **34**(2): p. 656-665.

57. Du, Y., et al., *Multifunctional label-free electrochemical biosensor based on an integrated aptamer.* Analytical Chemistry, 2008. **80**(13): p. 5110-5117.

58. Bogaerts, W., et al., *Silicon microring resonators.* Laser & Photonics Reviews, 2012. **6**(1): p. 47-73.

59. Kang, C., et al., *Optimized light-matter interaction and defect hole placement in photonic crystal cavity sensors.* Optics Letters, 2012. **37**(14): p. 2850-2852.

60. Lawrie, J.L., Y. Jiao, and S.M. Weiss, *Size-Dependent Infiltration and Optical Detection of Nucleic Acids in Nanoscale Pores.* Ieee Transactions on Nanotechnology, 2010. **9**(5): p. 596-602.

61. Lawrie, J.L., et al., *Synthesis of DNA oligonucleotides in mesoporous silicon.* Physica Status Solidi a-Applications and Materials Science, 2009. **206**(6): p. 1339-1342.

62. Zhao, Y.L., et al., *Effect of DNA-Induced Corrosion on Passivated Porous Silicon Biosensors.* Acs Applied Materials & Interfaces, 2014. **6**(16): p. 13510-13519.

63. Vandenberg, E.T., et al., *Structure of 3-Aminopropyl Triethoxy Silane on Silicon-Oxide.* Journal of Colloid and Interface Science, 1991. **147**(1): p. 103-118.

64. Aissaoui, N., et al., *Silane Layers on Silicon Surfaces: Mechanism of Interaction, Stability, and Influence on Protein Adsorption.* Langmuir, 2012. **28**(1): p. 656-665.

65. Steel, A.B., et al., *Immobilization of nucleic acids at solid surfaces: Effect of oligonucleotide length on layer assembly.* Biophysical Journal, 2000. **79**(2): p. 975-981.

66. Lee, C.Y., et al., *Surface coverage and structure of mixed DNA/alkylthiol monolayers on gold: Characterization by XPS, NEXAFS, and fluorescence intensity measurements.* Analytical Chemistry, 2006. **78**(10): p. 3316-3325.

67. Peterson, A.W., R.J. Heaton, and R.M. Georgiadis, *The effect of surface probe density on DNA hybridization.* Nucleic Acids Research, 2001. **29**(24): p. 5163-5168.

68. Vollmer, F. and L. Yang, *Review Label-free detection with high-Q microcavities: a review of biosensing mechanisms for integrated devices*, in *Nanophotonics*. 2012. p. 267.

69. Grist, S.M., et al., *Silicon photonic micro-disk resonators for label-free biosensing.* Opt Express, 2013. **21**(7): p. 7994-8006.

70. Scheler, O., et al., *Label-free, multiplexed detection of bacterial tmRNA using silicon photonic microring resonators.* Biosens Bioelectron, 2012. **36**(1): p. 56-61.

71. Washburn, A.L., L.C. Gunn, and R.C. Bailey, *Label-Free Quantitation of a Cancer Biomarker in Complex Media Using Silicon Photonic Microring Resonators.* Analytical Chemistry, 2009. **81**(22): p. 9499-9506.

72. Washburn, A.L., et al., *Quantitative, label-free detection of five protein biomarkers using multiplexed arrays of silicon photonic microring resonators.* Anal Chem, 2010. **82**(1): p. 69-72.

73. Byeon, J.-Y. and R.C. Bailey, *Multiplexed Evaluation of Capture Agent Binding Kinetics Using Arrays of Silicon Photonic Microring Resonators.* The Analyst, 2011. **136**(17): p. 3430-3433.

74. Luchansky, M.S. and R.C. Bailey, *High-Q Optical Sensors for Chemical and Biological Analysis.* Analytical Chemistry, 2012. **84**(2): p. 793-821.

75. Jonsson, U., et al., *Real-time biospecific interaction analysis using surface plasmon resonance and a sensor chip technology.* Biotechniques, 1991. **11**(5): p. 620-7.

76. Fagerstam, L.G., et al., *Biospecific interaction analysis using surface plasmon resonance detection applied to kinetic, binding site and concentration analysis.* J Chromatogr, 1992. **597**(1-2): p. 397-410.

77. Dixit, C.K., et al., *Multisubstrate-compatible ELISA procedures for rapid and high-sensitivity immunoassays.* Nat. Protocols, 2011. **6**(4): p. 439-445.

78. Qavi, A.J. and R.C. Bailey, *Multiplexed Detection and Label-Free Quantitation of MicroRNAs Using Arrays of Silicon Photonic Microring Resonators.* Angewandte Chemie International Edition, 2010. **49**(27): p. 4608-4611.

79. Chakravarty, S., et al., *Multiplexed specific label-free detection of NCI-H358 lung cancer cell line lysates with silicon based photonic crystal microcavity biosensors.* Biosens Bioelectron, 2013. **43**: p. 50-5.

80. Zou, Y., et al. *High yield silicon photonic crystal microcavity biosensors with 100fM detection limit*. 2013.

81. Sun, Y.Z. and X.D. Fan, *Optical ring resonators for biochemical and chemical sensing.* Analytical and Bioanalytical Chemistry, 2011. **399**(1): p. 205-211.

82. Foltz, I.N., M. Karow, and S.M. Wasserman, *Evolution and Emergence of Therapeutic Monoclonal Antibodies What Cardiologists Need to Know.* Circulation, 2013. **127**(22): p. 2222-2230.

83. Nelson, A.L., E. Dhimolea, and J.M. Reichert, *Development trends for human monoclonal antibody therapeutics.* Nature Reviews Drug Discovery, 2010. **9**(10): p. 767-774.

84. Zhou, H. and M.A. Mascelli, *Mechanisms of monoclonal antibody-drug interactions.* Annual review of pharmacology and toxicology, 2011. **51**: p. 359-372.

85. Bogaerts, W., et al., *Silicon microring resonators.* Laser & Photonics Reviews, 2012. **6**(1): p. 47-73.

86. Shang, Y., R. Mernaugh, and X. Zeng, *Characterization of the native and denatured herceptin by enzyme linked immunosorbent assay and quartz crystal microbalance using a high-affinity single chain fragment variable recombinant antibody.* Analytical chemistry, 2012. **84**(19): p. 8164-8170.

87. Zhang, Y., et al., *Selection of active ScFv to G-protein-coupled receptor CCR5 using surface antigen-mimicking peptides.* Biochemistry, 2004. **43**(39): p. 12575-12584.

88. Yablonovitch, E., *Inhibited Spontaneous Emission in Solid-State Physics and Electronics.* Physical Review Letters, 1987. **58**(20): p. 2059-2062.

89. Lai, W.C., et al., *Slow light enhanced sensitivity of resonance modes in photonic crystal biosensors.* Applied Physics Letters, 2013. **102**(4).

90. Kim, G.H., et al., *Coupling of small, low-loss hexapole mode with photonic crystal slab waveguide mode.* Optics Express, 2004. **12**(26): p. 6624-6631.

91. Kuramochi, E., et al., *Ultrahigh-Q photonic crystal nanocavities realized by the local width modulation of a line defect.* Applied Physics Letters, 2006. **88**(4).

92. Akahane, Y., et al., *Fine-tuned high-Q photonic-crystal nanocavity.* Optics Express, 2005. **13**(4): p. 1202-1214.

93. Tanabe, T., et al., *Trapping and delaying photons for one nanosecond in an ultrasmall high-Q photonic-crystal nanocavity.* Nature Photonics, 2007. **1**(1): p. 49-52.

94. Kuramochi, E., et al., *Ultrahigh-Q two-dimensional photonic crystal slab nanocavities in very thin barriers.* Applied Physics Letters, 2008. **93**(11): p. 111112.

95. Quan, Q.M. and M. Loncar, *Deterministic design of wavelength scale, ultra-high Q photonic crystal nanobeam cavities.* Optics Express, 2011. **19**(19): p. 18529-18542.

96. Hu, S. and S.M. Weiss, *Design of Photonic Crystal Cavities for Extreme Light Concentration.* ACS Photonics, 2016. **3**(9): p. 1647-1653.

97. Almeida, V.R., et al., *Guiding and confining light in void nanostructure.* Optics Letters, 2004. **29**(11): p. 1209-1211.

98. Deotare, P.B., et al., *High quality factor photonic crystal nanobeam cavities.* Applied Physics Letters, 2009. **94**(12): p. 121106.

99. Kuramochi, E., et al., *Ultrahigh-Q one-dimensional photonic crystal nanocavities with modulated mode-gap barriers on SiO2 claddings and on air claddings.* Opt Express, 2010. **18**(15): p. 15859-69.

100. McCutcheon, M.W., et al., *High-Q transverse-electric/transverse-magnetic photonic crystal nanobeam cavities.* Applied Physics Letters, 2011. **98**(11): p. 111117.

101. Rivoire, K., S. Buckley, and J. Vuckovic, *Multiply resonant photonic crystal nanocavities for nonlinear frequency conversion.* Optics Express, 2011. **19**(22): p. 22198-22207.

102. Oulton, R.F., et al., *A hybrid plasmonic waveguide for subwavelength confinement and long-range propagation.* Nature Photonics, 2008. **2**(8): p. 496-500.

103. Xiao, S.M., et al., *Loss-free and active optical negative-index metamaterials.* Nature, 2010. **466**(7307): p. 735-U6.

104. Moitra, P., et al., *Realization of an all-dielectric zero-index optical metamaterial.* Nature Photonics, 2013. **7**(10): p. 791-795.

105. Lin, D.M., et al., *Dielectric gradient metasurface optical elements.* Science, 2014. **345**(6194): p. 298-302.

106. Seidler, P., et al., *Slotted photonic crystal nanobeam cavity with an ultrahigh quality factor-to-mode volume ratio.* Opt Express, 2013. **21**(26): p. 32468-83.

107. Fromm, D.P., et al., *Gap-dependent optical coupling of single "Bowtie" nanoantennas resonant in the visible.* Nano Letters, 2004. **4**(5): p. 957-961.

108. Li, H. and M. Li, *Optomechanical photon shuttling between photonic cavities.* Nature Nanotechnology, 2014. **9**(11): p. 913-919.

109. McNab, S.J., N. Moll, and Y.A. Vlasov, *Ultra-low loss photonic integrated circuit with membrane-type photonic crystal waveguides.* Optics Express, 2003. **11**(22): p. 2927-2939.

110. Luo, Y., et al., *On-Chip Hybrid Photonic–Plasmonic Light Concentrator for Nanofocusing in an Integrated Silicon Photonics Platform.* Nano Letters, 2015. **15**(2): p. 849-856.

111. Rotenberg, N. and L. Kuipers, *Mapping nanoscale light fields.* Nat Photon, 2014. **8**(12): p. 919-926.

112. Fan, S.H. and J.D. Joannopoulos, *Analysis of guided resonances in photonic crystal slabs.* Physical Review B, 2002. **65**(23).

113. Zhou, W.D., et al., *Progress in 2D photonic crystal Fano resonance photonics.* Progress in Quantum Electronics, 2014. **38**(1): p. 1-74.